7-13-2016 12:00 AM

Assessment of Post-Treatment Imaging Changes Following Radiotherapy using Magnetic Susceptibility Techniques

Jean-Guy Belliveau, *The University of Western Ontario*

Supervisor: Ravi Menon, *The University of Western Ontario*
Joint Supervisor: Glenn Bauman, *The University of Western Ontario*
A thesis submitted in partial fulfillment of the requirements for the Doctor of Philosophy degree in Medical Biophysics
© Jean-Guy Belliveau 2016

Recommended Citation

Abstract

Radiation therapy (RT) is a common treatment for brain neoplasms and is used alone or in combination with other therapies. The use of RT has been found to be successful in controlling tumors and extending the overall survival of patients; however, there are many unanswered questions regarding radiotherapy effects in the normal brain surrounding or infiltrated by tumor. Changes to the vascular and parenchyma have been documented, and more recently inflammatory mechanisms have been postulated to play a role in radiation injury. Traditional imaging techniques used within the clinic (CT and MRI) are often lacking in their ability to differentiate between recurrent tumor, transient treatment effects, or radiation necrosis. The primary goal of this thesis is to demonstrate an MRI acquisition method that has been shown to be sensitive to deoxygenated blood and iron content as a potential biomarker of radiation effect on the normal brain. Specifically, post-processing techniques are used to determine the applicability of qualitative images such as Susceptibility-Weighted Imaging (SWI) and quantitative methods such as Quantitative Susceptibility Mapping (QSM) and apparent traverse relaxation (R_2^*) using the same sequence. These methods are potential surrogate markers for vascular changes and neuroinflammatory components that could predict sub-acute and long-term radiation effects. Within this thesis, R_2^* is shown to be a promising marker for the prediction of radiation necrosis, whereas SWI and QSM are shown to be excellent modalities for detecting long-term effects such as microbleeds. Additionally, R_2^* is shown to be a potentially useful technique in identifying post-imaging treatment changes (pseudoprogression) following chemoradiotherapy for malignant glioma. Finally, the use of this non-contrast method shows promise for integration within a clinical setting and the potential for expansion to multi-center clinical trials.

Keywords

Co-Authorship Statement

At the time of thesis preparation Chapter 1 (adapted version), 3, 4, and 5 are manuscripts in final preparation for submission, the contribution of each other is outlined below:

Unless otherwise indicated Jean-Guy Belliveau outlined the research objectives, conducted the experiments, analyzed the data, and contributed to software that was used in data analysis. Jean-Guy Belliveau also wrote the manuscripts that are being prepared for publication.

James Stewart, as a co-author of Chapter 3 provided the use of the x-Rad 225 and performed dose planning. Dr. Michael Jensen as co-author provided the use of the micro-CT and performed dose planning was performed. Histology was performed by the laboratory in the adjoining hospital.

Dr. Keng Yeow Tay, as a co-author of Chapter 4, provided neurological assessment of the images based on specific research questions developed by Jean-Guy Belliveau.

Dr. Maria MacDonald and Dr. David McDonald, as co-authors of Chapter 5, recruited patients that were selected for this study.

Dr. Glenn Bauman as Jean-Guy Belliveau's co-supervisor and co-author of Chapters 1, 3, 4, and 5 recruited patients for Chapter 3. He also provided guidance, aided in the interpretation of data and liaised with any required information (images/health records) at the hospital.

Dr. Ravi Menon as Jean-Guy Belliveau's supervisor and co-author of Chapters 3, 4 and 5 provided guidance, aided in the interpretation of the data, provided supervision, and was the primary investigator for the human and animal research ethics protocol used.

Acknowledgments

First and foremost, I would like to acknowledge Dr. Ravi Menon for his guidance during the past six years in my capacity of master and doctoral student within his lab. Dr. Menon provided me with all the necessary tools needed to succeed in this and future endeavors regarding to research. I would also like to acknowledge my co-supervisor Dr. Glenn Bauman who allowed me to experience and deepened my understanding of research within a clinical environment and allowing me to experience that clinical research may not always be as simple as stated within a textbook. I would also like to acknowledge my committee members Dr. Jean Theberge and Dr. Eugene Wong, who provided me with a different perspective of data analysis and Dr. Wong, who assisted me with carrying out radiotherapy experiments.

I would also like to thank the entire staff at CFMM, who provided me with support and guidance over the course of my PhD. Specifically, I would like to acknowledge Igor Solovey and Dr. David Rudko, who participated in many discussions regarding data analysis, interpretation and implantation of algorithms. I would also like to thank Ashley Kirley, who went above and beyond her duties as animal technician to ensure my animal experiments were successful.

I would also like to thank the financial and moral support of my entire family, who may not fully understand the amount of work that is necessary for a Ph.D., yet were always supportive and provided many forms of encouragement along the way. Finally, I would like to thank the support of my future wife, who in addition to volunteering for MRI scans, was understanding of the long hours needed to perform my experiments and has provided emotional and moral support along the way.

Table of Contents

List of Tables

List of Figures

List of Abbreviations

1D: One dimension

2D: Two dimension

3D: Three dimension

ADC: Apparent Diffusion Coefficient

AUCR: Area Under the Curve Ratio

B_0: Main Magnetic Field

ΔB: Magnetic Field Shift

BOLD: Blood Oxygenation Level Dependence

CBF: Cerebral Blood Flow

CBV: Cerebral Blood Volume

CEL: Contrast Enhancing Lesion

CE-SWI: Contrast-Enhancing Susceptibility-Weighted Imaging

CEST: Chemical Exchange Saturation Transfer

CSF: Cerebral Spinal Fluid

CT: Computed Tomography

DSC: Dynamic Susceptibility Contrast

DWI: Diffusion Weighted Imaging

EPI: Echo Planar Imaging

FA: Flip Angle

FLAIR: Fluid Attenuated Inversion Recovery

FOV: Field of View

γ: Gyromagnetic Ratio

GRAPPA: Generalized Auto-calibrating Partial Parallel Acquisition

GRE: Gradient Echo

Hz: Hertz

KPS: Karnofsky Performance Status

kTRANS: Volume Transfer Coefficient

LFS: Local Frequency Shift

MEA: Magnitude Echo Average

ME-GRE: Multi-Echo Gradient Echo

MGMT: O-6-methylguanine-DNA methyltransferase

mIP: Minimum Intensity Correction

MRI: Magnetic Resonance Imaging

MTT: Mean Transfer Time

M_z**:** Bulk Magnetization

NEL: Non-contrast Enhancing Lesion

OS: Overall Survival

PD: Progressive Disease

PET: Positron Emission Tomography

PFS: Progression Free Survival

φ**:** Phase

psPD: Pseudoprogression

QSM: Quantitative Susceptibility Maps

R_1**:** Longitudinal Relaxation Rate

R_2**:** Transverse Relaxation Rate

R_2^***:** Apparent Relaxation Rate

RANO: Response Assessment for Neuro-Oncology Criteria

rCBF: relative Cerebral Blood Flow

rCBV: relative Cerebral Blood Volume

RF: Radio-Frequency

rMTT: relative Mean Transfer Time

rPH: relative Peak height

RECIST: Response Evaluation Criteria in Solid Tumor

SAR: Specific Absorption Rate

SHARP: Sophisticated Harmonic Artifact Reduction for Phase Data

SNR: Signal to Noise Ratio

SPD: Sum of Product of Diameters

SPECT: Single Photon Emission Computer Tomography

SWI: Susceptibility-Weighted Imaging

T_1**:** Longitudinal Relaxation Time

T_2**:** Transverse Relaxation Time

T_2^***:** Apparent Transverse   Relaxation Time

TE: Echo Time

TI: Inversion Time

TR: Repetition Time

TMZ: Temozolomide

VSF: Voxel Spread Function

WHO: World Health Organization

Scope of Thesis

The following is an overview of the chapters presented in this thesis.

Chapter One provides a review of the current clinical methodologies for diagnosing brain tumors in patients as well as imaging techniques used in the follow-up of their therapy. The current methods provide motivation for the use of the multi-echo gradient echo sequence that is the overarching method utilized in this thesis.

Chapter Two contains a concise overview of the factors which influence magnetization and thus signal in a gradient echo sequence. Through the use of magnetic field inhomogeneity, the contrast from the magnitude and phase of the signal can be used to post-process images which contain qualitative and quantitative information regarding the local magnetic susceptibility of tissue.

Chapter Three presents an animal model of radiation necrosis measuring the apparent transverse relaxation (R_2^*) over 28 weeks and retrospectively assessed to determine its use as a predictive marker of radiation necrosis. The steady increase in R_2^* in the hippocampus and internal and external capsule present a potential marker for the prediction of radiation necrosis up to 10 weeks before morphological imaging.

Chapter Four provides a descriptive study on the long-term effects of radiation to the normal tissue within the brain of patients treated for low-grade benign neoplasms. It demonstrates for the first time that patients who receive radiation therapy alone could potentially be at an increased risk of vascular disease due to the appearance of microbleeds within the high dose region. Additionally, it demonstrates that white matter hyperintensities on FLAIR can be detected with R_2^* and SWI while showing that these lesions are venocentric, a source of significant research in other diseases such as multiple sclerosis.

Chapter Five describes a study in which R_2^* was used to differentiate patients who have non-specific T_1-gadolinium enhancement following chemoradiotherapy for malignant glioma. It demonstrates that R_2^* can be used a marker to distinguish between patient progression and treatment effect by the increased R_2^* in a patient's T_1 contrast enhancing lesion's and FLAIR's non-enhancing lesion.

Finally, Chapter 6 presents an overview of the findings in this thesis and seeks to expand on the refinements for the experiments as well as discuss methods for implementation of this technique for multi-center trials.

Chapter 1

1   Brain Tumor Background

Glioma is one of the most common primary brain tumors in adults and may present as

low-grade (WHO Grade II), anaplastic (WHO Grade III) or Glioblastoma (WHO Grade

IV) with Grades III and IV often being grouped under the term "malignant glioma".

Following treatment of glioma, the ability to determine treatment success is of utmost

importance to select the appropriate subsequent course of action. New advances in

medical imaging have given neuroradiologists the ability to characterize gliomas using

both anatomic and functional techniques. Combined with new therapies introduced in the

clinic, interpreting these multi-parametric medical images and determining the correct

course of management can become complex as imaging changes may reflect

combinations of treatment effect and tumor changes. When a malignant glioma patient

initially presents, the standard therapy consists of maximal surgical resection followed by

a course of Temozolomide (TMZ) chemotherapy and radiation therapy as suggested by a

clinical trial by Stupp et al. in 2009 [1]. More recent studies have suggested radiation and

chemotherapy may also be efficacious for patients with low-grade glioma [2,3]. For

malignant glioma, combined chemotherapy has been shown to provide superior overall

survival (OS) of 14.6 months compared to 12.1 months for radiotherapy alone and has

proved to increase the progression-free survival (PFS) time to 6.9 months from 5 months.

At the time of malignant glioma recurrence, anti-angiogenic agents are commonly used

with PFS in the range of 6 months [4,5]. Within the clinic, patient monitoring during and

shortly after therapy is necessary due to the high cost and toxicity associated with

continuing ineffective treatments and the potential detriment to patients by discontinuing

effective treatments prematurely. For patients whose treatment was unsuccessful, their inclusion in clinical trials of new therapies may be the best option if a true progression diagnosis can be determined. The ability to differentiate true responders from non-responders ensures patients fit the criteria for clinical trials and is important for evaluating the efficacy of new agents studied on clinical trials [6].

1.1 Progression Free Survival as a surrogate marker for Overall Survival

The success of therapies is traditionally gauged by the ability to improve the OS, which is measured from the time of enrollment into a clinical trial until death from any cause. Using OS as a marker of treatment success necessitates a longer follow-up period to gauge OS and may provoke confounding effects caused by sequential therapies. As a result, pre-clinical and clinical trials have begun to adopt alternate endpoints to help determine the efficacy of treatments at earlier time points. For malignant glioma, PFS, which is defined as the time from commencing therapy until evidence of disease progression or death, is a potential replacement for OS. Within the glioblastoma literature, Han et al. [7] demonstrated a strong correlation ($R^2 = 0.92$) between OS and PFS. As further pre-clinical research and clinical trials are conducted the use of PFS as a marker of treatment success is becoming more prominent and allows the more efficient evaluation of new therapies. A limitation of PFS is the ability to diagnose patients correctly with true tumor progression as both clinical and imaging changes may reflect the effects of therapies as well as the tumor.

1.1.1 Confounding factors in assessing PFS

In most cases, patients will see symptoms improve due to the removal of the tumor and response to radiation therapy and adjuvant chemotherapy. In addition to clinical assessment, imaging is also performed to gauge response to treatment. During active treatment, pseudoprogression and pseudoresponse are two treatment-related effects that can confound the assessment of PFS and potentially lead to inappropriate patient management by either over-calling (false positive) or under-calling (false negative) true tumor progression.

Pseudoprogression is typically characterized by increased enhancement on a T_1-weighted gadolinium MRI following treatment with chemoradiotherapy; however, patients may be clinically stable and may not exhibit symptoms that would typically be associated with tumor progression. Currently, the most widely used standard of care is to continue therapy for an additional 4-6 weeks and repeat imaging [8]. In cases of pseudoprogression, on early follow-up, imaging changes typically stabilize or improve. Whereas, within cases of true progression, imaging changes will worsen. Correct interpretation of pseudoprogression would prevent abandoning an effective therapy prematurely. Pseudoresponse is a transient response to antiangiogenic drugs where the blood brain barrier becomes re-established, leading to a decrease in vascular permeability and a subsequent reduction in contrast enhancement on T_1-weighted gadolinium MRI, rather than true tumor response [9]. Correct interpretation of pseudoresponse is important to avoid continuing an ineffective therapy as tumors may progress in the absence of contrast enhancement while on anti-angiogenic agents. To account for the possibility of pseudoprogression and pseudoresponse, revised criteria that incorporate clinical and

therapeutic information into the interpretation of images have been proposed [8]. Even such revised criteria are imperfect and objective imaging methods for the accurate determination of tumor response or progression are needed. The following is an overview of current imaging methods that propose to differentiate response from non-response as well as pseudoprogression and pseudoresponse following treatment for glioma.

1.2 Conventional Imaging Techniques and Interpretation

1.2.1 CT Imaging

Computed tomography (CT) imaging was once regarded as the gold standard imaging methodology and is still commonly used to rule out acute intracranial pathology such as stroke. Prior to the introduction of MRI, CT was the primary imaging modality for the evaluation of brain tumors. The Macdonald criteria [10] for assessing response based on CT findings were developed and have been in widespread use ever since. Subsequently, the Macdonald criteria has been adapted and revised from CT for its use in MRI [11] and later evolved into the RANO and RECIST criteria described later in this article. Conventional CT imaging is now seldom used in the clinic for the follow-up of patients who have been treated for glioma, except for screening for acute pathology (such as acute bleed or obstructive hydrocephalus) in the case of rapid clinical deterioration, or for surgical guidance and radiation treatment planning. The use of CT perfusion as a potential functional imaging technique for glioma is discussed in later sections.

1.2.2 Conventional MRI

Compared to CT, MRI offers superior soft-tissue contrast and has tremendously improved the ability to diagnose brain tumors. The use of paramagnetic contrast agents

for MRI in the 1980's also allowed clinicians to understand the breakdown of the blood-brain barrier and allow for improved diagnoses. Gadolinium agents play an essential role in differentiating normal versus tumorous tissue and are used in conventional MRI imaging following treatment; however, some non-contrast methods that aid in differentiation are slowly being introduced into everyday clinical use and include sequences such as Diffusion-Weighted MRI and Magnetic Resonance Spectroscopy (MRS).

1.2.2.1 Typical Scan Parameters

Following completion of treatment, all patients have a follow-up MRI to determine whether the treatment was effective. Currently, 1.5 T MRIs and 3 T MRIs are commonly used in clinical settings. A consensus group assembled in 2015 recommended that at a minimum, the sequences listed in Table 1.1 be acquired as part of a standard imaging protocol for glioma [12]. The consensus group also suggested acquisition parameters for various MRI manufacturers.

Table 1.1 Recommend Acquisitions for patients undergoing MRI for glioma. Post-contrast T_1-weighted image were used for the MacDonald and RECIST criteria, while RANO incorporates the post-contrast T_1-weighted image as well as FLAIR.

1.	Pre-Contrast T_1-weighted mage	IR-GRE Sagittal or axial acquisition Scan time 5-10 minutes
2.	Axial 2D or 3D FLAIR	TSE or FSE Scan time 4-8 minutes
3.	Axial 2D T_2-weighted image	TSE or FSE Scan time 2-4 minutes
4.	Axial 2D Diffusion Weighted Image	Single-shot EPI 2-4 minutes for 3 b-values and 3 directions
5.	Post Contrast T_1-weighted image	IR-GRE Sagittal or axial acquisition FA 10-15° Same parameters as pre-contrast image

The images obtained in Table 1.1 form a basis to assess the treatment response of tumors. Until 2010, the MacDonald criteria was used extensively for 2D measurements of the gadolinium-enhancing lesion area and the RECIST criteria was used as a substitute with only 1D measurements along the long axis. With newer therapeutics and imaging capabilities (e.g. non-contrast imaging such as FLAIR) a re-evaluation of the methods was necessary and evolved into the RANO criteria that uses 2D measurements of the gadolinium-enhancing lesion as well as FLAIR lesion [13]. In 2010, the RANO working group suggested alternate guidelines to assist in differentiating between responders and non-responders. The guidelines could also distinguish pseudoprogression and pseudoresponse by incorporating information from multi-parametric MRI as well as clinical and therapeutic information[8]. In 2015, further guidelines from the RANO working group were released for patients receiving immunotherapy [14] to address the delayed response to therapy and therapy-induced inflammation.

The current RANO criteria measures the largest five lesions in a 2D plane along their longest diameters in two perpendicular axes as shown in Figure 1.1. The sum of these areas produces the sum of the product of diameters (SPD). This measurement should be done after surgery but before treatment to form a baseline measurement. Following the baseline scan, measurements should be done after each subsequent MRI. These measurements compared to the baseline SPD constitute the basis to determine whether there is a complete response, partial response, stable disease, or progressive disease as shown in Table 1.2.

SPD=A1*B1+A2*B2+...
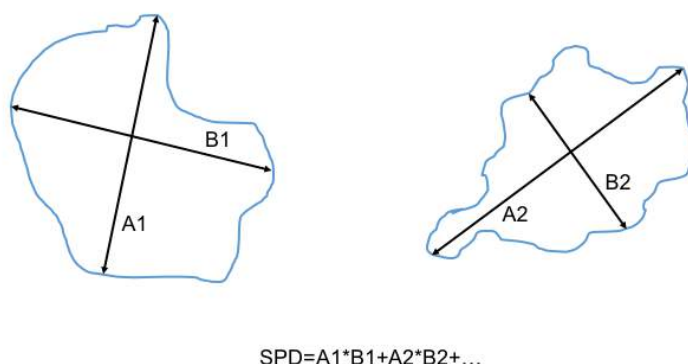
Figure 1.1 Demonstration of how to calculate the SPD in RANO criteria. Two lesions are shown, but 5 lesions must be calculated.

Table 1.2 Summary of possible diagnosis and guidelines for use of the RANO criteria.

Status	Definition for T_1-Gd enhancement	T_2-weighted FLAIR Area	Clinical Status
Complete Response	All target lesions disappeared (potential for pseudoresponse)	Stable or decreasing	Stable or improving
Partial Response	SPD decreased by at least 50% of baseline value	Stable or decreasing	Stable or improving
Stable Disease	SPD between a 50% decrease and 25% increase	Stable or decreasing	Stable or improving
Progressive Disease	SPD increased by at least 25% (potential of pseudoprogression)	Increasing	Decreasing

The RANO criteria also accounts for pseudoresponse and pseudoprogression with these measurements. In pseudoresponse, a patient's gadolinium-enhancing MRI typically will have a significant decrease within days of starting of anti-angiogenic therapy; however, since the tumor cells may co-opt blood vessels in the brain, the tumor may develop into a non-enhancing phenotype [15]. The co-opting of blood vessels is a mechanism in which tumor cells obtain a blood supply from the pre-existing vasculature leading to potential metastasis [16]. The RANO criteria accounts for this by taking a measurement of the FLAIR's lesion area. If the FLAIR hyperintensities remain stable or increase, the lesion is marked as progressive disease.

As previously noted, pseudoprogression is a condition that initially appears to be a progressive disease following treatment due to new lesions or growth of lesions within the radiation treatment areas. According to the RANO criteria, no determination of pseudoprogression or true progression should be done until 12 weeks following therapy

unless the new enhancing areas are outside the radiation treatment volume, the patient

exhibits clinical deterioration, or other methods can definitively rule out

pseudoprogression (e.g. repeat resection demonstrating viable tumor).

1.2.2.2 RANO Drawbacks

While RANO represents a significant consensus effort to standardize imaging

interpretation in the era of new therapies, it remains an imperfect tool. Kazda et al.

demonstrated that the RANO criteria does not correlate well with a clinician's assessment

of progression in anaplastic astrocytoma based on a composite of neurological symptoms

and imaging [17]. The authors also suggested this may be specific for anaplastic glioma or

other WHO Grade 3 tumors as they typically have poor contrast enhancement. The

authors emphasize the importance of considering the entire clinical context such as

change in neurologic function or symptoms in addition to imaging measures of response

(including quantitative methods such as RANO or RECIST).

Perez-Larraya et al. set out to study the usefulness of the RANO criteria compared to the

MacDonald criteria, RECIST, and RECIST + FLAIR in patients treated with

Bevacizumab [18]. Their results showed that correlation of the median PFS following

treatments with imaging was not statistically significant with any of the criteria. Their

results further validated the usefulness of FLAIR, as defined by the RANO and RECIST

+ FLAIR criteria, to avoid the overestimation of PFS in patients and commented that with

the integration of FLAIR in both 1D and 2D methods, RECIST has similar response rates

compared to the RANO criteria. Thus, while the RANO criteria represents an

improvement in response assessment that reflects newer therapies and imaging

modalities, there are clinical situations where existing imaging may be ambiguous (e.g. at

early time points following chemoradiotherapy or response to antiangiogenic agents). In these situations, newer imaging analyses or modalities may be beneficial and will be discussed in the following sections.

1.3   Diffusion Weighted Imaging

A Diffusion Weighted Image (DWI) is a common sequence acquired as part of a multiparametric MRI imaging study for CNS tumors. The most common metric calculated from DWI is the Apparent Diffusion Coefficient (ADC). ADC provides information regarding water molecules' ability to freely diffuse. In areas of high cellularity, such as tumor, the water cannot diffuse as easily and has a restricted diffusion or low ADC values (visualized as darker areas on reconstructed ADC images). In areas of necrosis or within cysts, increased ADC values reflect less impeded water diffusion (represented by brighter areas on ADC images).

In order to calculate the ADC, diffusion gradients of at least b=1000 s/mm^2 and b=0 s/mm^2 (no diffusion weighting) are recommended, although having an extra diffusion gradient at b=500 s/mm^2 will increase the quality of the computation [12]. For ADC measurements, the b-value is an indicator of the strength of the diffusion gradient applied along at least three axis. The applied b-value of the gradient is inversely related with the diffusion distance of water molecules, meaning a high b-value will be preferential to water molecules with restricted diffusion. The Stejskal-Tanner model for the pulsed diffusion method is defined with the following equation [19]:

$$b = \gamma^2 G^2 \delta^2 (\Delta - \frac{\delta}{3}) \quad 1.1$$

where γ is the gyromagnetic ratio (Hz/T), G (T/m) is the strength of the gradient, δ (seconds) is the duration of the gradient pulse, and Δ is the time between diffusion gradients Most clinical scanners have the software to compute ADC online. Bulik suggested that a mean absolute ADC value of 1.3 x10^{-3} mm^2/s or lower within the tumor volume could be a cutoff for glioblastoma relapse compared to pseudoprogression [20] based on a series of 24 patients (sensitivity and specificity of 100% and a $P < 0.001$). Applying such a threshold should not be done without other a priori knowledge, as noted by the authors who observed that acquisition methods and other factors such as tissue necrosis and vascularity may confound the computation of ADC.

In response to these confounding factors, further studies have investigated metrics other than mean ADC, such as fifth percentile ADC, maximum ADC, and minimum ADC. Additionally, other metrics can be computed when acquiring Diffusion Tensor Imaging such as Fractional Anisotropy; however, to date, such methods have not demonstrated high sensitivity and specificity without the inclusion of other imaging modalities and intervention from the neuroradiologist. [21]

Chu et al. have shown that higher b-value (b=3000 s/mm^2) gradients can be used to differentiate pseudoprogression and true progression using the ADC's histogram at the expense of relative signal intensity at the high *b*-value. They found that by using the fifth percentile of ADC values within an enhancing lesion, true progression can be differentiated from pseudoprogression using different *b*-values. (b=1000 mm^2/sec $P = 0.049$, b=3000 mm^2/sec $P < 0.001$) [22].

The obvious limitation of such methods is that the fifth percentile of all voxels within the tumor disregards 95% of the information and may not take into account the heterogeneity of the lesion.

Baseline mean ADC using the lower Gaussian curve of a double Gaussian distribution has also been shown to be a statistically significant marker of PFS and OS following treatment with Bevacizumab. Using a mean pretreatment threshold value of 1.2×10^{-3} mm^2/s, patients with a high ADC pretreatment had a significantly longer PFS (153 days versus 76.5 days, $P = 0.045$) and OS (376 days versus 194 days, $P = 0.003$) [23].

A comprehensive review of published ADC data concluded there is a potential for using the baseline minimum ADC value due to its inverse correlation with tumor grade and PFS [24]. Using previously obtained data over a 1.5 year observation period, with ADC cutoffs ranging from 0.6×10^{-3} mm^2/s to 1.0×10^{-3} mm^2/s, a statistically significant difference in mean survival rate was observed (73.8% above cutoff, 22.7% below cutoff, $P<0.001$).

Texture analysis can also be used for second order analysis of the ADC values within the tumor. Measures such as entropy, skewness, and kurtosis can be calculated based on the heterogeneity of the ADC values. Ryu et al. [25] demonstrated that the grading of glioma is feasible using these metrics to differentiate Grade 2 and 3 tumors from Grade 4 tumors. Entropy as a measure of grading glioma yielded a higher sensitivity and similar specificity (78.1% and 87.5%) compared to the fifth percentile ADC values (59.4% and 87.5%).

Brynoflsson et al. performed a more complex method using principal component analysis to determine a pseudoscore. Their methods demonstrated that many of the second order factors, as well as certain first order features, could identify two groups in their data with a median survival of 1099 days in one group and 345 days in another group ($P = 0.001$). [26]

As a whole, the usefulness of ADC as a pretreatment prognostic factor and as an assessment of response remains ambiguous. A further limitation is the potential variability between vendor and imaging protocol. Tsujita et al. demonstrated significant variability between scanner types and ADC values in healthy brain [27]; however, the variability between vendor types was on the same scale as between patients. In brain tumors, it is possible that the heterogeneity of ADC values within tumors or necrotic tissues may often confound routine quantitative methods; however, the quick acquisition time relative to the entire study time makes its acquisition worthwhile, and standardization of ADC acquisition and development of generalizable metrics remain goals of ongoing research.

1.4   Perfusion

1.4.1   Perfusion CT

While contrast-enhanced CT provides inferior anatomic imaging compared to MRI, the quantitative nature of CT allows for more accurate determination of functional parameters such as blood flow. Perfusion CT is a very quick method to determine blood flow within the brain using a nonionic contrast and relies on the rapid acquisition of serial CT images throughout a constant brain volume during the injection of a bolus of contrast

material. Tracking passage of contrast through a brain region over a fixed time period allows for the calculation of a variety of vascular parameters. For example, relative Cerebral Blood Volume (rCBV) is a measure of blood volume in a selected area of tissue relative to normal brain (typically white matter) and is calculated by measuring the area under the concentration-time curve. Relative Cerebral Blood Flow (rCBF) is a measure of blood volume that passes within an area of tissue in a specific amount of time and is calculated by deconvolving the concentration-time curve with the arterial input function to get the tissue response function. The height of the tissue response function is the measured CBF, while the rCBF is the ratio of CBF to normal brain. Another parameter that is acquired is rMTT, a measure of average time blood spends within the capillary circulation and is calculated by dividing the area under the concentration time curve by the height of the tissue response function (rCBF). Depending on the processing either rMTT or rCBF is calculated and their relation is as follows: CBV =CBF*MTT.

A rCBV threshold of 1.92 has been shown to differentiate between low and high-grade tumors with a sensitivity of 85.7% and specificity of 100% [28] in 19 patients. The same group also demonstrated that perfusion CT had significant differences between patients with treatment necrosis compared to recurrent tumor using rCBV, rCBF, and rMTT. Specifically, a lower rCBV (1.2±0.3 versus 2.1±0.7; $P<0.001$), lower rCBF (1.2±0.5 versus 2.6±1.7; $P = 0.004$), and higher rMTT (1.4±0.4 versus 1.0±0.4; $P = 0.018$) was predictive of treatment effect [29]. The use of perfusion CT is a quick and economical alternative to perfusion MRI (discussed in section 1.4.2) and is readily available in many imaging departments as perfusion CT has become a standard of care for stroke imaging. While concerns about cumulative radiation dose delivered by CT perfusion (as may be

necessary to monitor glioma) are being addressed through low dose CT techniques, the resolution of soft tissue with CT remains inferior to MRI, which may limit its adoption as a standard imaging technique in assessing tumor response.

1.4.2   Perfusion MRI

Like perfusion CT, perfusion MRI seeks to characterize vascular parameters in the tumor. There are two primary techniques used for perfusion MRI. Dynamic Contrast Enhancement (DCE, also referred to as permeability MRI), is a T_1-weighted sequence and like perfusion CT, uses images that are acquired before, during, and after injection of a contrast agent. The serial acquisition of the T_1-weighted images allow for a measurement of the signal intensity over time that reflects the tissue's perfusion, vessel permeability, and extravascular-extracellular space [30]. This method offers an advantage over the traditional static T_1-weighted gadolinium image. The tissue's response to contrast can be observed and quantified with derived parameters such as kTrans, a reproducible measure of permeability in glioma patients, or Area Under the Curve Ratios (AUCR) [31,32] a measure of the ratio between area under the curve at wash-in and wash-out. For example, Suh et al. demonstrated that when using T_1-weighed DCE, the ratio between the wash-in and wash-out AUCR is statistically significant different ($P < 0.001$) between pseudoprogression and true tumor progression groups [33]. The sensitivity and specify of this method varied based on the method in which the cumulative AUCR was calculated (i.e. 25th percentile, 75th percentile, etc.) but were between 73-90 %.

Dynamic Susceptibility Contrast (DSC) imaging is a T_2 or T_2^* weighted sequence also known as bolus tracking MRI and relies on serial imaging to track contrast flow through the brain. In DSC, the magnetic susceptibility of the contrast leads to a decrease in signal

intensity that can be measured and converted into parametric maps of CBV and CBF [34].

Derived parameters from DSC in MRI include the rCBV (similar measurement to

perfusion CT), rPH (ratio between the peak height within an enhancing lesion versus

normal white matter) and PSR (percent signal recovery of the signal intensity after a first

pass of contrast bolus). Within neuro-oncology, the vascular leakiness of tumors and

pooling of blood make rCBV the most widely used parameter as the contrast causes

changes in both T_2 and T_2^* sequences, providing robust measurement [35]. A study by

Young et al. demonstrated that the rCBV and rPH were significantly higher in groups

with true progression compared to pseudoprogression while the percent signal recovery

(PSR) was significantly greater in the pseudoprogression group [36]. They determined that

a rCBV <1.8 yielded a sensitivity and specificity of 100% and 75% respectively, while a

rCBV < 2.4 yielded a 69% sensitivity and a 100% specificity for differentiating

progression from pseudoprogression. They also demonstrated that a cutoff rPH of 1.7

achieved 100% sensitivity and specificity in differentiating true progression from

pseudoprogression. Gahramanov et al. demonstrated a similar rCBV value cutoff with a

different contrast agent (Ferumoxytol) [37]. The use of the rCBV cutoff with Ferumoxytol

was also associated with a statistically significant hazard ratio (median OS for high rCBV

163 days, median OS for low rCBV 591 days, hazard ratio 0.098, $P = 0.004$). In the same

study, correcting the standard perfusion contrast (Gadoteridol) for leakage produced a

statistically significant hazard ratio (0.12, $P = 0.003$).

Standardization of CBV is a process in which the CBV is transformed into a unitless

consistent intensity scale that is independent of scanner vendor [38]. The use of

measurement of standardized rCBV pre and post-Bevacizumab has been shown to have

statistically significant results for OS, and post-Bevacizumab has proved to be indicative

of PFS [39]. In this study, if the unitless standardized rCBV ranged from 0 to 50000, where

0 indicated no rCBV and 50000 was rCBV typically found in large vessels. For

pretreatment standardized rCBV below 4400, the mean OS was shown to be 380 days

compared to 175 days ($P = 0.024$). A standardized rCBV below 4400 after Bevacizumab

was shown to have a PFS of 167 days compared to 78 days ($P = 0.006$).

1.5   Susceptibility-Weighted MRI

One of techniques used in this thesis is Susceptibility-Weighted MRI (SWI), explained in

further detail in the next chapter. Due to the vascular nature of tumors, SWI is slowly

being recognized as an alternative to standard imaging techniques as it is sensitive to

vascular changes.

SWI can be done with or without the use of gadolinium contrast. A study by Sayyari et

al. indicated that SWI could be better suited for delineating the tumor when using

contrast, especially when identifying the lesion on SWI (CE-SWI) for measurement in

ADC [40]. They showed that the CE-SWI lesion was significantly smaller than the

gadolinium-enhancing T_1 lesion ($P = 0.002$ first time point, $P = 0.004$ second time point).

Additionally, this study used parametric tests on a patient-by-patient basis showing

elevated ADC for patients with pseudoprogression or stable disease and decreased ADC

in tumor progression. Additionally, they found that using CE-SWI as a contrast mask for

ADC measurements allowed for proper classification as opposed to the gadolinium

enhanced T_1 lesion. Fahrendorf et al. have recently demonstrated an increased ability to

delineate the tumor invasion zone of a high-grade glioma using contrast-induced phase

shift (CIPS) between a contrast enhanced and non-contrast SWI [41] allowing better

delineation of tumor extension beyond the boundaries detected by T_1 gadolinium-enhanced MRI. They further elaborate that CE-SWI could be a better imaging technique for visualization of the tumor invasion zone compared to gadolinium-enhancing T_1 and FLAIR, especially in smaller tumors, but recommended further study among a variety of glioma phenotypes.

Promising work with non-contrast SWI may lie with the processing of quantitative data using a multi-echo gradient echo sequence. The multi-echo sequence allows for measurement of the apparent transverse tissue relaxation (R_2^*) and further processing of phase can be performed to compute measures of Quantitative Susceptibility Mapping (QSM). A feasibility paper demonstrated the ability to differentiate blood deposits and calcification using QSM [42], suggesting that QSM would be useful to identify oligodendroglia variants of high-grade glioma (calcification being more common in oligodendroglial tumors) and to monitor for calcifications developing in tumors.

SWI has also been used to identify microbleeds following the treatment of glioma as well as monitoring patients following anti-angiogenic therapy [43]. Lupo et al. showed that patients receiving chemoradiotherapy for malignant glioma had increased micro-bleed formation two years post radiation while patients receiving anti-angiogenic therapy had fewer microbleeds overall following treatment. These authors, among others, postulate that anti-angiogenic drugs could have a radioprotective effect on the microvasculature.

The main drawback of SWI and its associated quantitative methods is the lack of standardization for post-processing leading to subjective interpretation of the data [44]. Additionally, gradient-echo sequences are more susceptible to motion, poor magnetic

field shims, and titanium clips that may be used in brain surgery. Furthermore, there is limited clinical information that correlates SWI imaging techniques with clinical outcomes in the treatment of glioma. Thus, its performance in differentiating true progression from pseudoresponse and pseudoprogression remains to be determined.

1.6   Other Imaging Modalities

There exist many other experimental techniques in the diagnosing and follow-up of brain tumors. MRI techniques such as spectroscopy have been used in the clinic and can help identify patterns of important brain metabolites like NAA, Choline, and lactate. Other techniques such as Chemical Exchange Saturation Transfer (CEST) and hyperpolarized C-13 may provide imaging information at a molecular level regarding tissue pH and metabolism. Nuclear medicine tracers for Single Photon Emission Computed Topography (SPECT) and Positron Emission Topography (PET) are also areas of active research in attempting to understand the metabolism and molecular profiles of tumors, treatment effect, and radiation necrosis. While it is necessary to be aware of such methods and their results when developing experiments, for this work they are not elaborated upon. These methods are either referenced or discussed, when relevant, in subsequent chapters.

1.7   References

1.   Stupp R, Hegi ME, Mason WP, et al. Effects of radiotherapy with concomitant and adjuvant temozolomide versus radiotherapy alone on survival in glioblastoma in a randomised phase III study: 5-year analysis of the EORTC-NCIC trial. Lancet Oncol. 2009; 10(5): 459–466.

2.   Buckner JC, Shaw EG, Pugh SL, et al. Radiation plus Procarbazine, CCNU, and Vincristine in low-grade glioma. N. Engl. J. Med. 2016; 374(14): 1344–1355.

3.   Fisher BJ, Hu C, Macdonald DR, et al. Phase 2 study of temozolomide-based chemoradiation therapy for high-risk low-grade gliomas: preliminary results of Radiation Therapy Oncology Group 0424. Int. J. Radiat. Oncol. Biol. Phys. 2015; 91(3): 497–504.

4.   Cohen MH, Shen YL, Keegan P, Pazdur R. FDA drug approval summary: bevacizumab (Avastin) as treatment of recurrent glioblastoma multiforme. Oncologist. 2009; 141131–1138.

5.   Gilbert MR. Antiangiogenic Therapy for Glioblastoma: Complex Biology and Complicated Results. J. Clin. Oncol. 2016; 34(14): 1–4.

6.   Stuplich M, Hadizadeh DR, Kuchlmeister K, Scorzin J, Filss C, Langen K-J. Late and prolonged pseudoprogression in glioblastoma after treatment with Lomustine and Temozolomide. J. Clin. Oncol. 2013; 30(21): 129–132.

7.   Han K, Ren M, Wick W, et al. Progression-free survival as a surrogate endpoint for overall survival in glioblastoma: A literature-based meta-analysis from 91 trials. Neuro. Oncol. 2014; 16(5): 696–706.

8.   Wen PY, Macdonald DR, Reardon DA, et al. Updated response assessment criteria for high-grade gliomas: response assessment in neuro-oncology working group. J. Clin. Oncol. 2010; 28(11): 1963–1972.

9.   Clarke JL, Chang SM. Pseudoprogression and Pseudoresponse : Challenges in

Brain Tumor Imaging. Curr. Neurol. Neurosci. Rep. 2009; 9241–246.

10. Macdonald DR, Cascino TL, Schold SC, Cairncross JG. Response criteria for phase II studies of supratentorial malignant glioma. J. Clin. Oncol. 1990; 8(7): 1277–80.

11. Bauman G, Lote K, Larson DA, et al. Pretreatment factors predict overall survival for patients with low-grade glioma: a recursive partitioning analysis. Int. J. Radiat. Oncol. Biol. Phys. 1999; 45(4): 923–929.

12. Ellingson BM, Bendszus M, Boxerman JL, et al. Consensus recommendations for a standardized Brain Tumor Imaging Protocol in clinical trials. Neuro. Oncol. 2015; 17(9): 1188–1198.

13. Eisenhauer E, Therasse P, Bogaerts J, et al. New response evaluation criteria in solid tumours: Revised RECIST guideline (version 1.1). Eur. J. Cancer. 2009; 45(2): 228–247.

14. Okada H, Weller M, Huang RY, et al. Immunotherapy response assessment in neuro-oncology: a report of the RANO working group. Lancet Oncol. 2015; 16(15): e534–e542.

15. Pàez-Ribes M, Allen E, Hudock J, et al. Antiangiogenic Therapy Elicits Malignant Progression of Tumors to Increased Local Invasion and Distant Metastasis. Cancer Cell. 2009; 15(3): 220–231.

16. Donnem T, Hu J, Ferguson M, et al. Vessel co-option in primary human tumors and metastases: an obstacle to effective anti-angiogenic treatment? Cancer Med. 2013; 2(4): 427–36.

17. Kazda T, Hardie JG, Pafundi DH, Kaufmann TJ, H. BD, Laack NN. Evaluation of RANO response criteria compared to clinician evaluation in WHO grade III anaplastic astrocytoma: implications for clinical trial reporting and patterns of failure. J. Neurooncology. 2015; 8(12): 1699–1712.

18. Gállego Pérez-Larraya J, Lahutte M, Petrirena G, et al. Response assessment in recurrent glioblastoma treated with irinotecan-bevacizumab: comparative analysis of the Macdonald, RECIST, RANO, and RECIST + F criteria. Neuro. Oncol. 2012; 14(5): 667–673.

19. Stejskal EO, Tanner JE. Spin Diffusion Measurements: Spin Echoes in the Presence of a Time-Dependent Field Gradient. J. Chem. Phys. 1965; 42(1): 288.

20. Bulik M, Kazda T, Slampa P, Jancalek R. The Diagnostic Ability of Follow-Up Imaging Biomarkers after Treatment of Glioblastoma in the Temozolomide Era: Implications from Proton MR Spectroscopy and Apparent Diffusion Coefficient Mapping. Biomed Res. Int. 2015; 20151–9.

21. Wang S, Sakai Y, Chawla S, et al. Differentiating Tumor Progression from Pseudoprogression in Patients with Glioblastomas Using Diffusion Tensor Imaging and Dynamic Susceptibility Contrast MRI. Am. J. Neuroradiol. 2016; 37(1): 28–36.

22. Chu HH, Choi SH, Ryoo I, et al. Differentiation of true progression from pseudoprogression in glioblastoma treated with radiation therapy and concomitant temozolomide: comparison study of standard and high-b-value diffusion-weighted imaging. Radiology. 2013; 269(3): 831–840.

23. Ellingson BM, Sahebjam S, Kim HJ, et al. Pretreatment ADC histogram analysis is a predictive imaging biomarker for bevacizumab treatment but not chemotherapy in recurrent glioblastoma. Am. J. Neuroradiol. 2014; 35(4): 673–679.

24. Zulfiqar M, Yousem DM, Lai H. ADC values and prognosis of malignant astrocytomas: Does lower ADC predict a worse prognosis independent of grade of tumor? A meta-analysis. Am. J. Roentgenol. 2013; 200(3): 624–629.

25. Ryu YJ, Choi SH, Park SJ, Yun TJ, Kim J-H, Sohn C-H. Glioma: Application of whole-tumor texture analysis of diffusion-weighted imaging for the evaluation of tumor heterogeneity. PLoS One. 2014; 9(9): e108335.

26.   Brynolfsson P, Nilsson D, Henriksson R, et al. ADC texture-an imaging biomarker for high-grade glioma? Med. Phys. 2014; 41(10): 101903.

27.   Tsujita N, Kai N, Fujita Y, et al. Interimager Variability in {ADC} Measurement of the Human Brain. Magn Reson Med Sci. 2014; 13(2): 81–87.

28.   Ellika SK, Jain R, Patel SC, et al. Role of perfusion CT in glioma grading and comparison with conventional MR imaging features. Am. J. Neuroradiol. 2007; 28(10): 1981–1987.

29.   Jain R, Narang J, Schultz LR, et al. Permeability estimates in histopathology-proved treatment-induced necrosis using perfusion CT: can these add to other perfusion parameters in differentiating from recurrent/progressive tumors? Am. J. Neuroradiol. 2011; 32(4): 658–663.

30.   Essig M, Shiroishi MS, Nguyen TB, et al. Perfusion MRI: The Five Most Frequently Asked Technical Questions. Am. J. Roentgenol. 2013; 200(1): 24–34.

31.   Tofts PS, Brix G, Buckley DL, et al. Estimating Kinetic Parameters From Dynamic Contrast-Enhanced T1-Weighted MRI of a Diffusable Tracer: Standardized Quantities and Symbols. J. Magn. Reson. Imaging. 1999; 10(July): 223–232.

32.   Jackson A, Jayson GC, Li KL, et al. Reproducibility of quantitative dynamic contrast-enhanced MRI in newly presenting glioma. Br. J. Radiol. 2003; 76(903): 153–156.

33.   Suh CH, Kim HS, Choi YJ, Kim N, Kim SJ. Prediction of pseudoprogression in patients with glioblastomas using the initial and final area under the curves ratio derived from dynamic contrast-enhanced T1-weighted perfusion MR imaging. Am. J. Neuroradiol. 2013; 34(12): 2278–2286.

34.   Ostergaard L. Principles of cerebral perfusion imaging by bolus tracking. J. Magn. Reson. Imaging. 2005; 22(6): 710–717.

35. Cha S, Knopp EA, Johnson G, Wetzel SG, Litt AW, Zagzag D. State of the Art Intracranial Mass Lesions : Dynamic Contrast-enhanced. Perfusion. 200211–29.

36. Young RJ, Gupta A, Shah AD, et al. MRI perfusion in determining pseudoprogression in patients with glioblastoma. Clin. Imaging. 2013; 37(1): 41–49.

37. Gahramanov S, Muldoon LL, Varallyay CG, et al. Pseudoprogression of glioblastoma after chemo- and radiation therapy: diagnosis by using dynamic susceptibility-weighted contrast-enhanced perfusion MR imaging with ferumoxytol versus gadoteridol and correlation with survival. Radiology. 2013; 266(3): 842–852.

38. Bedekar D, Jensen T, Schmainda KM. Standardization of Relative Cerebral Blood Volume (rCBV) Image Maps for Ease of Both Inter- and Intrapatient Comparisons. Magn. Reson. Med. 2010; 64(3): 907–913.

39. Schmainda KM, Prah M, Connelly J, et al. Dynamic-susceptibility contrast agent MRI measures of relative cerebral blood volume predict response to bevacizumab in recurrent high-grade glioma. Neuro. Oncol. 2014; 16(6): 880–888.

40. Al Sayyari A, Buckley R, McHenery C, Pannek K, Coulthard A, Rose S. Distinguishing recurrent primary brain tumor from radiation injury: a preliminary study using a susceptibility-weighted MR imaging-guided apparent diffusion coefficient analysis strategy. Am. J. Neuroradiol. 2010; 31(6): 1049–1054.

41. Fahrendorf D, Schwindt W, Wolfer J, et al. Benefits of contrast-enhanced SWI in patients with glioblastoma multiforme. Eur. Radiol. 2013; 23(10): 2868–2879.

42. Deistung A, Schweser F, Wiestler B, et al. Quantitative Susceptibility Mapping Differentiates between Blood Depositions and Calcifications in Patients with Glioblastoma. PLoS One. 2013; 8(3): 1–8.

43. Lupo JM, Molinaro AM, Essock-burns E, et al. The effects of anti-angiogenic therapy on the formation of radiation-induced microbleeds in normal brain tissue

of patients with glioma. Neuro. Oncol. 2016; 18(1): 87–95.

44.   Mohammed W, Xunning H, Haibin S, Jingzhi M. Clinical applications of susceptibility-weighted imaging in detecting and grading intracranial gliomas: A review. Cancer Imaging. 2013; 13(2): 186–195.

Chapter 2

2 Quantitative and Qualitative Imaging with Multi-Echo Gradient Echo Imaging

The previous chapter reviewed the current methodologies for glioma imaging. It demonstrated how edema (measured through FLAIR or ADC) and the relationship of blood volume and flow (measured through perfusion) have been instrumental in the advancement of the diagnosis and monitoring of brain neoplasms. This chapter seeks to describe the motivation behind the use of qualitative images and quantitative measurements obtained from multi-echo gradient echo (ME-GRE) sequence.

In general, gradient echo imaging has become more commonplace [1] due to better magnetic field homogeneity and is used in many applications. Gradient-echo sequences differ from spin-echoes sequences by having a lower flip angle and lack of a refocusing pulse. This has a distinct advantage at increasing magnetic field strengths as limitations on transmit radiofrequency (RF) field homogeneity, and Specific Absorption Ratio (SAR) can be problematic [2].

2.1   Signal and Bulk Magnetization

By placing a sample within a magnetic field it will exhibit a bulk magnetization (M_z) parallel to the magnetic field (B_0) as shown in Figure 2.1. The bulk magnetization will precess at a certain frequency related B_0 and the gyromagnetic ratio, $\gamma = 42.577 \, MHz/T$, as shown in equation 2.1:

$$Frequency = \gamma * B_0 \quad [2.1]$$

Applying a radio-frequency pulse to the sample will "tip" the bulk magnetization into the transverse plane.
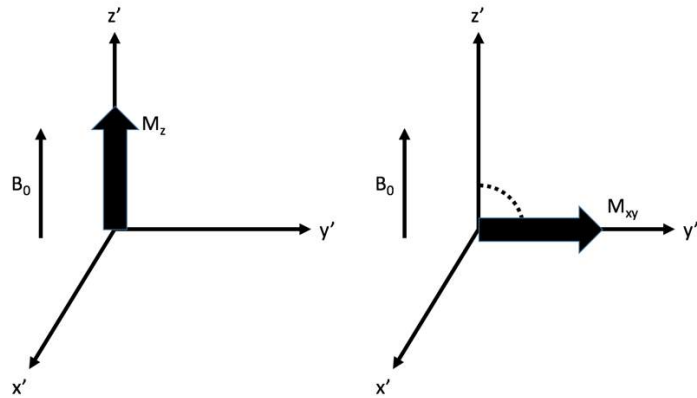
Figure 2.1 Example of bulk magnetization aligned along B_0 (left) and tipped into the x-y plane (right).

Figure 2.1 illustrates the x'-y' axis as the transverse plane relative to the rotating reference frame that precesses at the frequency in equation 2.1.

When tipped into the transverse plane, the bulk magnetization is placed into a non-equilibrium state, and the magnetization will return to equilibrium through spin-lattice (T_1) and spin-spin (T_2) relaxation. The precessing magnetization in the transverse plane induces a signal in a RF coil.

The net magnetization has a linear relationship with the external magnetic field. Therefore, higher field strengths allow for the potential of higher resolution imaging, faster acquisitions, or a combination of both.

2.1.1   Spin-Lattice Relaxation

One process by which the magnetization returns to equilibrium is through R_1 ($R_1=1/T_1$) relaxation. In its simplest form, this relaxation is a process in which the magnetization returns to equilibrium in the z-direction through interactions with the surrounding environment (lattice). T_1 increases with field strength and is not a contributing source of signal loss or contrast when using gradient-echo imaging for T_2^* weighting as a small flip angle is used (i.e. <15°) and pulse sequence repetition time (TR) is much faster than T_1 relaxation. T_1 is defined as the amount of time for the bulk magnetization to reach 63% ($1-e^{-1}$) of its original magnetization along z.

2.1.2   Spin-Spin Relaxation

Another process by which the magnetization returns to equilibrium is through R_2 relaxation ($R_2 = 1/T_2$). R_2 relaxation is due to tissue-specific spin-spin interactions which cause spins within a voxel to lose their coherence. The loss of coherence results in decay of the net magnetization in the x-y plane over time. In addition to these spin-spin interactions, spatial magnetic field variations may compound the loss of coherence causing the observed relaxation to be faster than the tissue specific relaxation. These spatial magnetic field variations are characterized by the additional terms R_2' (relaxivity caused by magnetic field inhomogeneities) and R_2^* (relaxivity from all sources) with their relations expressed in the following equations:

$$\frac{1}{T_2^*} = \frac{1}{T_2} + \frac{1}{T_2'} \quad [2.2\ a]$$

$$R_2^* = R_2 + R_2' \quad [2.2\ b]$$

In spin-echo imaging component of the loss of coherence can be recovered through the use of a 180° refocusing pulse; however, in gradient echo imaging the refocusing pulse is not used, resulting in a faster decay of the spin coherence. The contributing effects of magnetic field inhomogeneity, which causes the dephasing, can be largely attributed to the mesoscopic field and the macroscopic field that will be defined in the following section.

It should be noted that the effects of the macroscopic and mesoscopic field can be a factor in spin-echo imaging. As molecules diffuse over time, they may be exposed to variations in the magnetic field. Being exposed to variation of the magnetic field will result in molecules not being "refocused" when using the refocusing pulse. The choice of time between the excitation pulse and refocusing pulse (or multiple refocusing pulses) is an important consideration when using spin-echo sequences to measure contributions that arise only from the T_2 decay.

The T_2 (or T_2^*) time constant is defined as the amount of time needed for 37% of the signal to decay in the transverse plane (e^{-1}).

2.2 Influence on signal

As previously mentioned, in T_2^*-weighted MRI there are two main contributing factors to the signal decay in the transverse plane in addition to T_2 decay. They are, 1) the variation

of the macroscopic field that is slowly varying across the sample and 2) the mesoscopic field that influences the local magnetic field on a submillimeter scale.

2.2.1 Macroscopic Field

The variation of the macroscopic magnetic field is typically on the order of many imaging voxels. Variations of the macroscopic field are caused by air-tissue susceptibility differences [3–5] or general magnetic field imperfections that arise from placing an inhomogeneous sample within the scanner. Before imaging, major variations of the magnetic field can be "shimmed" by using various orders of shimming coils to offset the magnetic field variations.

2.2.2 Mesoscopic field

The mesoscopic field provides useful local information regarding the magnetic field inhomogeneity that is caused by paramagnetic or diamagnetic substances. In addition to affecting the local T_2^* that causes changes in the magnitude image, its influence can be detected on filtered phase images (discussed further in section 2.3).

2.2.2.1 Paramagnetism

Paramagnetism is caused by certain materials with unpaired electrons enhancing the main magnetic field. In humans and animals, MRI paramagnetism is often attributed to the presence of iron. Sources of iron include deoxygenated blood, originally shown by Ogawa [6], hemosiderin, or increases in iron content due to inflammation [7,8].

2.2.2.2   Diamagnetism

Diamagnetism is caused by materials that are repelled by the main magnetic field and induce an opposite local magnetic field. Typically, myelin, cerebral spinal fluid, and calcifications are diamagnetic [9].

2.2.2.3   Paramagnetism and Diamagnetism as a Source of Contrast

Both paramagnetic and diamagnetic compounds affect the local magnetic field in such a way as to influence T_2^*; however, when it comes to measuring the accrued phase, which is discussed in the next section, one must set a reference value. While the measured phase is referenced to the global frequency over the sample, the interpretation of such data would make quantification between patients and between sites difficult. To overcome this limitation, common areas such as the frontal or occipital white matter are used as a reference [10,11]. Using the white matter as a reference, paramagnetism will produce a decrease in accrued phase while calcification and CSF will result in an increase in phase accrual.

2.3   Multi-echo gradient echo imaging

Signal acquired from MRI imaging is inherently complex valued and can be recombined as a complex valued image. In most clinical applications the phase is discarded, and only the magnitude image is viewed; however, within the research setting the phase provides complementary information that can be used to enhance images (discussed in 2.3.2).

Post-processing techniques include forming magnitude images as well as phase (or frequency) images.

2.3.1   Magnitude

Figure 2.2 shows the magnitude image of three separate echoes from a six-echo gradient echo acquisition. The magnitude of the image is simply the absolute value of the complex data acquired from the scanner. It can be observed that there is an increase in T_2^* related contrast with longer echo times. Echo 1 has a more proton density-like contrast while Echo 6 has pronounced T_2^* weighting contrast due to the strong differential decay of regions with different T_2^* values. An advantage of multi-echo imaging is that an average of all magnitude images can be created to simplify visualization and potentially increase signal-to-noise ratio.
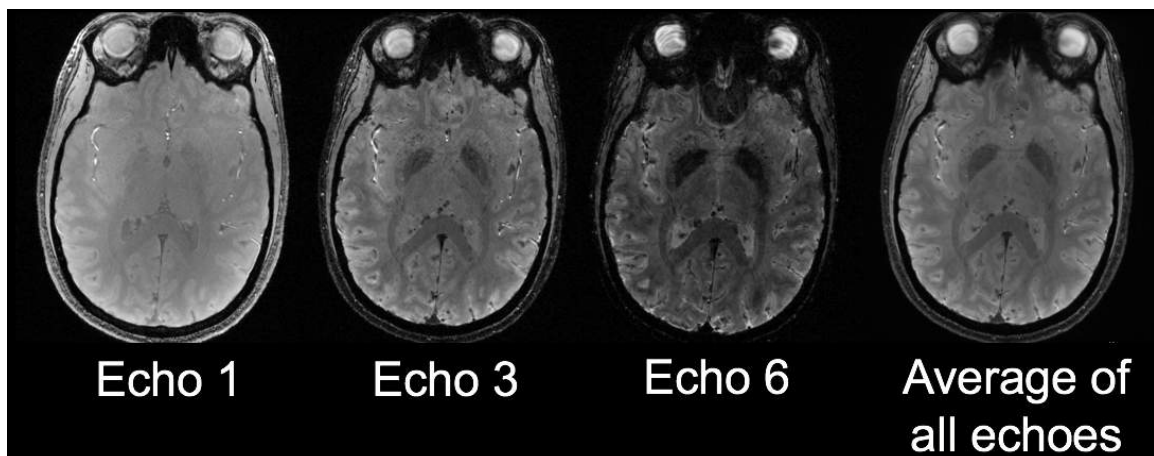
Figure 2.2 Example of various echoes acquired from a multi-echo gradient echo sequence and an average image of all echoes. TR: 40 ms, FA 13°, TE1=3.75 ms, TE3=11.95 ms, TE6=24.25 ms.

2.3.2   Phase

As previously discussed, the MR signal received from the magnetization is a complex

vector. The orientation of the magnetization vector within the transverse plane can be

described by a phase(φ). The measured phase arises from differences in the z component

of magnetic fields (microscopic, mesoscopic, and macroscopic) over a sample causing

slight variations in frequency in the range of 1-100 Hz. While the main nuclear

precession frequency is linearly related to the main magnetic field and the gyromagnetic

frequency as was shown in equation 2.1, differences in the main magnetic field can be

expressed much the same way, as shown in equation 2.3 and 2.4.

$$\Delta Frequency = \gamma \Delta B \quad [2.3]$$

Where $\Delta Frequency$ is the change in frequency and ΔB is the change in magnetic field.

The frequency offset measured at a specific echo time (TE) can be characterized as the

accrued phase (φ).

$$\varphi = \gamma \Delta B * TE \quad [2.4]$$

In equation 2.4 the ΔB term are contributions from both the local and global field

inhomogeneity; however, the phase contrast that is due to the local variations of magnetic

field inhomogeneity (i.e. mesoscopic and microscopic field) is of most interest. In order

to extract such detail, the acquired phase must be further processed.

2.3.3   Unwrapping and Filtering

The phase of the complex image acquired from the MRI is inherently bound between [-π to π] due to the nature of signal acquisition. This wrapped phase is not an accurate representation of the true relative phase within an image as the accrual of phase can be greater than 2π. The relationship between wrapped phase and unwrapped phase is shown in equation 2.5:

$$\varphi(r)_{unwrapped} = \varphi(r)_{wrapped} + 2\pi m \quad [2.5]$$

Where *m* is a positive or negative integer accounting for the number of wraps. An example of wrapped phase is shown in the top row of Figure 2.3.

Phase unwrapping attempts to remove any integer (m) of 2π from the image, and methods to unwrap phase that are acquired with a single echo are not trivial[12,13]. With multiple echo imaging, it is possible to set the relative phase of the first image to zero during reconstruction, and temporally unwrap the remaining echoes [14]. As such, only five echoes from a six echo sequence have information regarding the phase. Any remaining spatial wraps can be removed by adding or subtracting 2π at an area of wrapped phase. This unwrapped phase contains contribution of the local mesoscopic field and global field. The corresponding unwrapped phase is also shown in the middle row of Figure 2.3.

Once the unwrapped image is computed, the final stage is to remove the contributions of the globally varying magnetic field. As previously mentioned, these components have low spatial frequency and can be filtered using a Gaussian high-pass filter. An example of the filtered image is shown in bottom row of Figure 2.3.
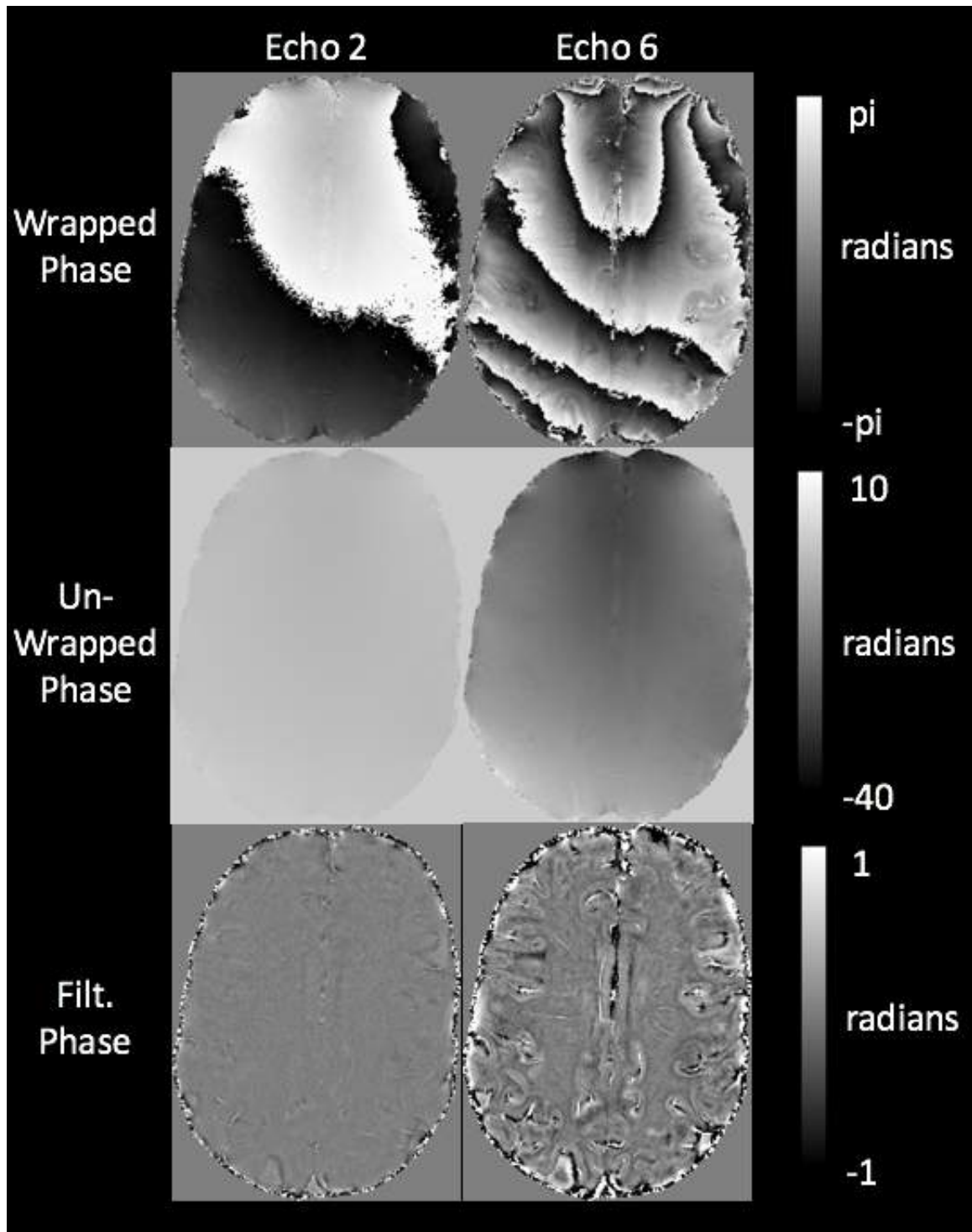
Figure 2.3 Examples of Wrapped Phase, Unwrapped Phase and Filtered Phase using a Gaussian high-pass filter for the second and sixth echo after processing the first echo to have zero phase.

While high-pass filtering is shown in Figure 2.3, other methods can remove the unwanted background field such as homodyne filtering [8,15], SHARP filtering [11], or Projection onto Dipole Fields [16]. All these techniques offer the ability to remove the unwanted contribution from the global field while retaining the local information. The amount of filtering that is performed is largely user and center specific, with a lack of standardization across sites. This lack of standardization causes the definition of global field variations and local field variations to differ between sites.

2.3.4   Post-Processing Techniques

Using the above data set, images can be processed into a final form that is viewable and provides qualitative or quantitative information. Methods such as Susceptibility-Weighted Imaging (SWI), Quantitative Susceptibility Mapping (QSM), or apparent transverse relaxation (R_2^*) are typical images that are computed with multi-echo gradient echo.

2.3.4.1   SWI

Susceptibility-Weighted Imaging, originally called BOLD venographic MRI [17], is a method in which the phase data can be used to enhance a magnitude image. The multi-echo technique is focused on computing a frequency mask, which is calculated by doing a least squares weighted fit through the multiple echoes [18]. Rewriting equation 2.4 and only taking into account the variations in local magnetic field the relationship between frequency and phase can be expressed as follows:

$$\frac{\varphi}{TE} = \gamma \Delta B_{local} \quad [\,2.6\ a\,]$$

$$\Delta F_{local} = \frac{\gamma}{2\pi}\Delta B_{local} \quad [\ 2.6\ b]$$

where the ΔF_{local} can be expressed in hertz or radians (dependent on the 2π term). This step is used in multi-echo SWI to provide a single image that is representative of the Local Frequency Shift (LFS). The LFS represents the changes in frequency within a voxel that is caused by the mesoscopic and microscopic field. The LFS map is used as a substitute for a phase-mask that can also be calculated based on the relationship in equations 2.6a and 2.6b. From this step, an appropriate frequency mask as shown in equation 2.7 can be created to process the LFS in a way that is sensitive to paramagnetic compounds such as deoxygenated blood, hemosiderin, or iron.

$$mask = \begin{cases} 1 \ if \ \Delta F_{local} > 0 \\ \dfrac{\Delta F_{local}}{|f_{cut}|} + 1 \ if \ f_{cut} < \ \Delta F_{local} < 0 \quad [2.7] \\ 0 \ if \ \Delta F_{local} < \ f_{cut} \end{cases}$$

The above mask causes any positive frequency to be set to 1, preserving the contrast in the magnitude image. Any negative frequency larger than a specified cut off is set to 0, with a linear transition between the cutoff frequency and 0. This amplifies the effect of negative frequency shifts on the magnitude image, yielding superior contrast, especially in the visualization of paramagnetic compounds such as deoxygenated blood. The linear transition is arbitrary and can be replaced with any transition function, or the mask could simply be a step function at $f_{cut} = 0$. Allowing for a gradual transition can provide for a smoother transition of negative frequency between 0 and f_{cut} providing for more pleasing contrast in the images [18].

The final step is to multiply the mask into the magnitude. The image can be multiplied n times, to enhance the visualization of the negative frequency components; however, too many multiplications may increase the noise of the image. A multiplication of 3-5 times often yields high contrast while limiting noise [4,18]. An example of the implementation of SWI is shown in Figure 2.4.
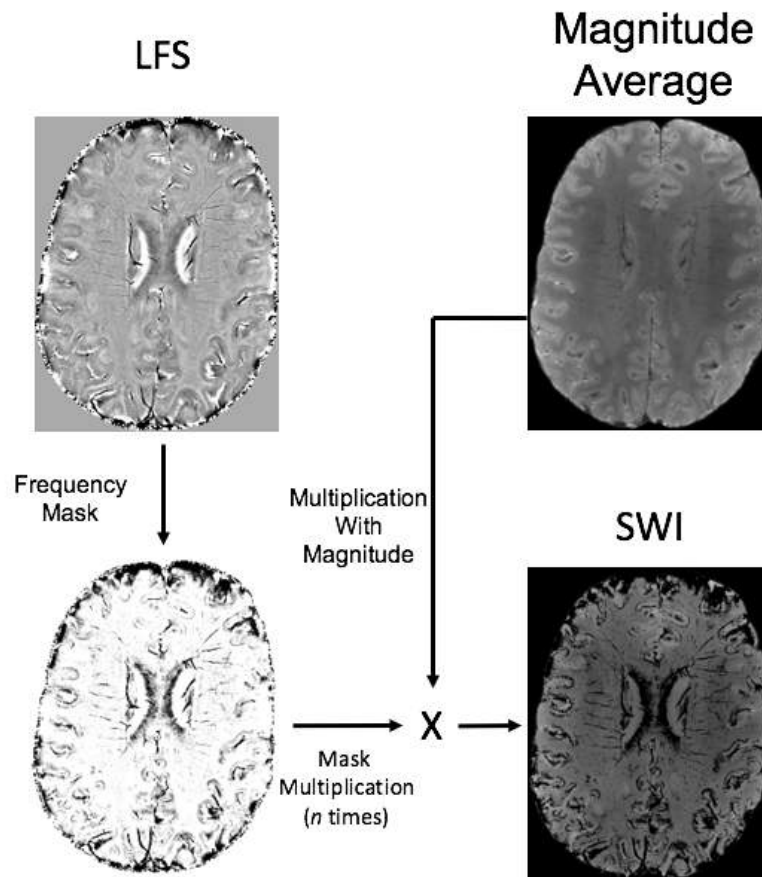
Figure 2.4 Example of the post-processing technique used to calculated SWI

One can take the additional step of using a minimum intensity projection through many slices to visualize veins that may appear in adjoining slices. This is often useful when

trying to distinguish veins from pathologies such as microbleeds, a topic which will be discussed in the subsequent chapters.

2.3.4.2   Quantitative Susceptibility Mapping

As was shown in equation 2.4 the accrued local phase is related to the product of the gyromagnetic ratio, changes in local magnetic field (ΔB), and TE. While this is useful for calculating the change in frequency as shown in equation 2.6, it is also possible to extract information about the susceptibility of the tissue within a voxel r. The magnetic field variation is related to the magnetization and the point-dipole response [19] as shown by the convolution in equation 2.8

$$\Delta B(\boldsymbol{r}) = \mu_0 M(\boldsymbol{r}) \bigotimes G(\boldsymbol{r}) \quad [2.8]$$

where M(**r**) is the local magnetization along B_0 (or z-direction), and G(**r**) is the Green's function for the point-dipole response function.

$$G(\boldsymbol{r}) = \frac{1}{4\pi} * \frac{3\cos^2\theta - 1}{r^3} \quad [2.9]$$

Where θ is defined as the angle between the local magnetization along B_0 and the phase at voxel r.

For magnetic susceptibility values $\chi \ll 1$, one can approximate the relationship between magnetization and susceptibility to be the following:

$$\mu_0 \, M(\boldsymbol{r}) \approx B_0 \, \chi(\boldsymbol{r}) \quad [2.10]$$

Therefore, the change in magnetic field at a specific point (r) can be expressed as follows:

$$\Delta B(\boldsymbol{r}) = B_0\, \chi(\boldsymbol{r}) \bigotimes G(\boldsymbol{r}) \qquad [2.11\ a]$$

$$\Delta B(\boldsymbol{r}) = B_0\, \chi(\boldsymbol{r}) \bigotimes \left\{ \frac{3\cos^2\theta - 1}{4\pi r^3} \right\} \qquad [2.11\ b]$$

While solving this equation may seem simple, it must be solved for every voxel in the image. With the number of voxels approaching tens of millions, this becomes a computationally expensive problem.

Fortunately, a convolution in image space can be expressed as a multiplication in Fourier domain as such:

$$F\{\Delta B(r)\} = F\{\chi(k)\} * \left\{ \frac{1}{3} - \frac{k_z^2}{k^2} \right\} \qquad [2.12]$$

where $k^2 = k_x^2 + k_y^2 + k_z^2$ and k_x, k_y and k_z represent the distances along the x, y, and z axes in the Fourier domain (or k-space). When k=0, which corresponds to the magic angle where the numerator of the Green's function in equation 2.11 is equal to 0 ($\theta = 54.74°$). This causes an ill-defined problem when attempting to solve for magnetic susceptibility χ in the Fourier domain due to the division by zero that may lead to streaking artifacts in the image reconstruction without optimization methods [10]. A simple optimization method could be to threshold values lower than a certain value to avoid dividing by 0.

Attempting to overcome this ill-posed problem is an area of active research with many algorithms currently proposed [10,20,21]. These methods typically involve using prior

information such as the edge information in the magnitude and phase and optimization methods to estimate the susceptibility.

2.3.4.3 R_2^* Mapping

The measurement of the apparent transverse relaxation rate, R_2^*, is the final post-processing step of multi-echo gradient echo sequences and the one used in all chapters of this thesis. The simplest form of R_2^* mapping is done by performing a best fit line through each of the acquired echoes assuming a mono-exponential decay, as shown in equation 2.13:

$$S(TE) = S_0\, e^{-TE(R_2^*)} \quad [2.13]$$

By acquiring S(TE) at known TE, solving for R_2^* appears to be rather trivial; however, there are some confounding factors in the computation of R_2^*. The first confound is that the acquired signal has superimposed noise from many sources that introduces error in the acquired data; therefore, a line of best fit through the discrete time points is used to model R_2^* decay. Throughout this thesis, a non-linear least squares method is used to model the line of best fit for equation 2.13. Further complications may arise when fitting data that approach the noise floor, although care is typically taken to avoid this situation by excluding data that are below some multiple of the noise.

The second confound is the contribution of the macroscopic fields that could affect the accurate measurement of R_2^* within the tissue. Several correction methods for the compensation of the macroscopic field exists, such as voxel spread functions [22] or sinc corrections [23]. These corrections are most needed when the slice thickness is much

greater than the in-plane resolution. When the slice becomes large, the macroscopic field can no longer be assumed to be linear, and the dephasing within voxels is influenced by the macroscopic field. These methods attempt to correct for the dephasing caused by the macroscopic field. While these the voxel spread function described in [21] was used for the experiment in this thesis, it was found that the slice thickness compared to in-plane resolution (either 1:1 or 1:2) did not play a major contributing factor to the dephasing of signal.

2.4   ME-GRE Application within this thesis

Together, the two previous chapters have given an appreciation of the role the vasculature plays in glioma and subsequent imaging of treated gliomas. Additionally, multi-echo gradient echo sequences have been shown to be susceptible to contributions of deoxygenated blood that is present in tumors. The paramagnetic contributions of iron and diamagnetic contributions of calcifications and myelin content will be investigated in the next chapter, and non-contrast methods that could be expanded for clinical use will be demonstrated.

2.5   References

1.   Markl M, Leupold J. Gradient echo imaging. J. Magn. Reson. Imaging. 2012; 35(6): 1274–1289.

2.   Basse-Lüsebrink TC, Kampf T, Fischer A, et al. SAR-reduced spin-echo-based Bloch-Siegert B(1)(+) mapping: BS-SE-BURST. Magn. Reson. Med. 2012; 68(2): 529–36.

3.   De Rochefort L, Liu T, Kressler B, et al. Quantitative susceptibility map

reconstruction from MR phase data using bayesian regularization: Validation and application to brain imaging. Magn. Reson. Med. 2010; 63(1): 194–206.

4.   Haacke EM, Xu Y, Cheng Y-CN, Reichenbach JR. Susceptibility weighted imaging (SWI). Magn. Reson. Med. 2004; 52(3): 612–618.

5.   Haacke EM, Reichenbach JR. Susceptibility Weighted Imaging in MRI: Basic Concepts and Clinical Applications. .

6.   Ogawa S, Lee T. Brain magnetic resonance imaging with contrast dependent on blood oxygenation. Proc. Natl. Acad. Sci. 1990; 87(24): 9868–72.

7.   Wisnieff C, Ramanan S, Olesik J, Gauthier S, Wang Y, Pitt D. Quantitative susceptibility mapping (QSM) of white matter multiple sclerosis lesions: Interpreting positive susceptibility and the presence of iron. Magn. Reson. Med. 2015; 74(2): 564–570.

8.   Denk C, Rauscher A. Susceptibility weighted imaging with multiple echoes. J. Magn. Reson. Imaging. 2010; 31(1): 185–91.

9.   Langkammer C, Krebs N, Goessler W, et al. Susceptibility induced gray-white matter MRI contrast in the human brain. Neuroimage. 2012; 59(2): 1413–1419.

10.   Haacke EM, Liu S, Buch S, Zheng W, Wu D, Ye Y. Quantitative susceptibility mapping: Current status and future directions. Magn. Reson. Imaging. 2015; 33(1): 1–25.

11.   Schweser F, Deistung A, Lehr BW, Reichenbach JR. Quantitative imaging of intrinsic magnetic tissue properties using MRI signal phase : An approach to in vivo brain iron metabolism ? Neuroimage. 2010; 54(4): 2789–2807.

12.   Feng W, Neelavalli J, Haacke EM. Catalytic multiecho phase unwrapping scheme (CAMPUS) in multiecho gradient echo imaging: Removing phase wraps on a voxel-by-voxel basis. Magn. Reson. Med. 2013; 70(1): 117–126.

13. Robinson S, Schödl H, Trattnig S. A method for unwrapping highly wrapped multi-echo phase images at very high field: UMPIRE. Magn. Reson. Med. 2014; 72(1): 80–92.

14. Walsh DO, Gmitro AF, Marcellin MW. Adaptive reconstruction of phased array NMR imagery. Magn. Reson. Med. 2000; 690682– 690.

15. Brainovich V, Sabatini U, Hagberg GE. Advantages of using multiple-echo image combination and asymmetric triangular phase masking in magnetic resonance venography at 3 T. Magn. Reson. Imaging. 2009; 27(1): 23–37.

16. Liu T, Khalidov I, de Rochefort L, et al. A novel background field removal method for MRI using projection onto dipole fields (PDF). NMR Biomed. 2011; 24(9): 1129–36.

17. Reichenbach JR, Barth M, Haacke EM, Klarhöfer M, Kaiser W a, Moser E. High-resolution MR venography at 3.0 Tesla. J. Comput. Assist. Tomogr. 2000; 24(6): 949–957.

18. Quinn MP, Gati JS, Klassen LM, et al. Comparison of multiecho postprocessing schemes for SWI with use of linear and nonlinear mask functions. Am. J. Neuroradiol. 2014; 35(1): 38–44.

19. Marques JP, Bowtell R. Application of a fourier-based method for rapid calculation of field inhomogeneity due to spatial variation of magnetic susceptibility. Concepts Magn. Reson. Part B Magn. Reson. Eng. 2005; 25(1): 65–78.

20. Liu J, Liu T, Rochefort L De, et al. Morphology enabled dipole inversion for quantitative susceptibility mapping using structural consistency between the magnitude image and the susceptibility map. Neuroimage. 2012; 59(3): 2560–2568.

21. Bilgic B, Fan AP, Polimeni JR, et al. Fast quantitative susceptibility mapping with L1-regularization and automatic parameter selection. Magn. Reson. Med. 2014;

72(5): 1444–1459.

22. Yablonskiy DA, Sukstanskii AL, Luo J, Wang X. Voxel spread function method for correction of magnetic field inhomogeneity effects in quantitative gradient-echo-based MRI. Magn. Reson. Med. 2013; 70(5): 1283–1292.

23. Peters AM, Brookes MJ, Hoogenraad FG, et al. T2* measurements in human brain at 1.5, 3 and 7 T. Magn. Reson. Imaging. 2007; 25(6): 748–753.

Chapter 3

3 R_2^* as a Marker for the Prediction of Radiation Necrosis in a Rat Model

3.1 Introduction

There is long history of the use of external beam Radiation Therapy (RT) to treat many forms of diagnosed brain neoplasms. While the ability to deliver conformal radiation to the tumor has improved over the years, delivery of radiation is still associated with significant doses to the adjacent brain parenchyma, and as such may cause side-effects in various stages of the treatment [1]. Side-effects are usually divided into acute, sub-acute, and late-effects [1,2]. Acute side-effects include brain encephalopathy secondary to increased edema and tends to be associated with larger brain volume treatment or larger dose per fraction treatments. Sub-acute or early-delayed side-effects are thought to be caused by transient demyelination causing somnolence syndrome and is related largely to the volume of brain radiated. In most cases, sub-acute side-effects either spontaneously recover or are managed with the temporary use of steroids. Late-effects can be irreversible and cause symptoms such as cognitive or neurological deficits. Among these late-effects, Radiation Necrosis (RN) represents a form of focal brain injury and the risk of RN is felt to be a complex interplay of total dose, dose per fraction, region, volume of brain treated, and host factors [3].

The permanent effects of RN are one of the reasons guidelines on the total deposited doses have been developed. Guidelines such as the Quantitative Analyses of Normal Tissue Effects in the Clinic (QUANTEC) [4] have been developed to attempt to limit the

incidence of RN. With the use of once-daily fractionation of less than 2.5 Gy/fraction, the incidence of RN for partial brain radiotherapy has been reported at 5% and 10% with a biologically effective prescription dose of 120 Gy_3 or 150 Gy_3, respectively. For radiosurgery, the toxicity and risk of radiation necrosis increases with the target volume, with increasing toxicity for a single fraction dose larger than 12 Gy and volumes larger than 5-10 cm^3. In addition to these guidelines, research has suggested reducing the volume of brain irradiated and avoiding exposure to certain eloquent regions such as the hippocampus, brainstem, and corpus callosum during RT should help to prevent neurocognitive decline and/or focal deficits [4–7].

To optimize radiation treatment plans, improvements in radiotherapy techniques such as image guidance, 3D conformal RT, Intensity Modulated Radiotherapy (IMRT), and proton therapy have been shown to decrease radiation to the surrounding margins around the planning treatment volume for certain brain tumors [8]. These techniques allow conformal RT of the neoplasm to reduce dose to surrounding brain and associated structures while maintaining a sufficiently high dose to the planning treatment volume. While efforts continue to optimize treatment plans, understanding the etiology of RN could potentially aid in predicting or preventing its occurrence over the long-term. Prognostic markers could allow for higher doses of RT to be delivered or toxicity to be further reduced. The most prominent RN hypotheses supported over the past decades are the vascular hypothesis [9–11] and the glial hypothesis[11–13]; however, neither fully explain RN[10,11].

The vascular hypothesis theorizes that RN is secondary to an ischemic event in the white matter and is thought to result from small vessel obliterative vasculitis induced by

radiation. Previous works have shown vessel wall thickening and vessel dilation [9,10] as well as decreases in blood vessel density and length following radiation [14].

The glial hypothesis suggests that radiation directly causes damage to the white matter precursor cells [15], which causes a demyelination process a few months to years following RT. Studies have also shown that RN can be associated with apoptosis of oligodendrocytes precursor [16] cells leading to the loss of mature oligodendrocytes and damage to the astrocytes leading to a breakdown of the blood-brain barrier [17]. It has been shown that damage to endothelial cells may lead to increased cytokine production [18] and elevated levels of vascular endothelial growth factor that lead to edema and necrosis [19–21]. Despite this work, the exact mechanism of RN is still uncertain and the potential for prevention and/or ameliorating the effects of RN remains an area of active research. More recently, a role for ongoing neuro-inflammatory processes has also been postulated [18].

While histological analysis provides a fundamental understanding into the cellular processes at play, this information is limited in its ability to track the evolution of radiation changes and requires invasive sampling, limiting its clinical application. In-vivo imaging potentially allows continuous monitoring and could serve as a non-invasive biomarker of tissue changes associated with radiation injury. The use of novel MRI sequences and higher magnetic fields for MRIs has added new ways in which radiation injury can be studied in pre-clinical and clinical settings. While traditional MRI techniques are usually inadequate for proper differentiation of RN and tumor recurrence [22,23], quantitative methods such as Diffusion Tensor Imaging [24,25], Magnetization Transfer Contrast [26] and Chemical Exchange Saturation Transfer [27] have been shown to correlate with RN and show promise in distinguishing between these entities.

As radiation necrosis is thought to be vascular, glial, or inflammatory in nature, it can be hypothesized that the use of higher field strength MRI and novel MRI sequences targeted at imaging vascular changes would allow us to detect and track the development of radiation injury in a pre-clinical model. To this end, this experiment sought to monitor animals receiving high dose partial brain radiation using imaging at a regular intervals using a 9.4T MRI scanner and performed quantitative and qualitative imaging over the course of 28 weeks. The techniques used were Susceptibility-Weighted Imaging (SWI) and apparent transverse relaxation rate (R_2^*) mapping, which have previously shown to be sensitive to venous vasculature [28] and tissue microstructure such as iron or myelin content [29,30]. These techniques were used in conjunction with the current gold-standard for imaging radiation necrosis, gadolinium-enhancing T_1 MRI.

3.2   Materials and Methods

3.2.1   Rat Selection and Imaging Time Points

All experiments were conducted with the approval of the Animal Use Subcommittee protocol at the University of Western Ontario. Male Fischer 344 (strain code 002) rats from Charles River were obtained at an age of approximately eight weeks and a weight range of 150-170 grams. Upon arrival, rats were acclimatized for three days and were then scanned for a baseline (week 0) 3-5 days after arrival at the animal facility. Rats were kept in a conventional housing room with a 12 hour (7am/7pm) light cycle. Seven to ten days after arrival, rats were irradiated using the methods described below. Rats were imaged on the MRI one week and two weeks after receiving their radiation and subsequently every 2-4 weeks until 28 weeks after irradiation at which point they were sacrificed. Some rats were sacrificed at earlier times points for histology or due to illness

(typically a 15-20% weight loss). Rats were divided into three cohorts; 1) micro-CT radiation (n=8), 2) x-Rad 225 radiation (n=10), 3) control (n=4).

3.2.2   Magnetic Resonance Imaging

Magnetic resonance imaging was performed on an Agilent 9.4 T horizontal small bore animal scanner. Rats were anesthetized with isofluorane combined with medical air (4% induction for 2-4 minutes, 1.5-2% maintenance). A custom-built two-channel head conformal transceive RF coil was used for imaging. Rats were placed on a stereotactic frame and secured with ear bars for the duration of the scan (1.5-2 hours). The acquisition protocol consisted of a bSSFP sequence (TR 5.0 ms / TE 2.5 ms, matrix size 250x180x180, FOV 43.8 mm x 31.5 mm x 31.5mm, scan time 11 minutes) and 3 averages of a 7 or 8 echo multi-echo gradient echo sequence (FA 10°, TR 30ms, TE 2.5 ms, ESP 2.7ms - 3.0ms, matrix size 250x180x180, FOV 43.8 mm x 31.5 mm x 31.5mm, scan time 16 minutes). At later time points, a T_2-weighted fast spin-echo sequence was also acquired. Gadolinium T_1 images were acquired at 12, 17, and 24 weeks using a similar anesthetization protocol. A T_1-weighted gradient echo (FA 30°, TR 45 ms, TE 2.5 ms, matrix size 130x90x90, FOV 43.8 mm x 31.5 mm x 31.5mm, scan time 6 minutes) was acquired approximately 2 hours following an *intraperitoneal* injection of the gadolinium contrast agent Magnevist (1mL/100g). It should be noted that the week 8 time point for control rats had to be discarded due to a malfunction of the gradient coil chiller causing unreliable data.

3.2.3   Partial Brain Radiation

The first irradiation was performed on a micro-CT irradiator [31]. A schematic of the

delivered radiation plan is shown in Figure 3.1. The treatment plan consisted of 10-30 Gy

delivered to the right hemisphere using a 150 kVp beam. Dose step gradients were

performed using the micro-CT jaws as shown in Figure 3.1. The delivered dose rate was

calculated to be 30 cGy/min; however, due to heating of the x-ray tube radiation delivery

had to be done in blocks allowing for cool-down over the course of radiation delivery.

The effective dose rate (delivered dose / total time) was calculated to be approximately

10-15 cGy/min depending on total delivered dose when delivered over the course of three

hours. The micro-CT had imaging capabilities allowing us to confirm the dose delivery to

the proper area.
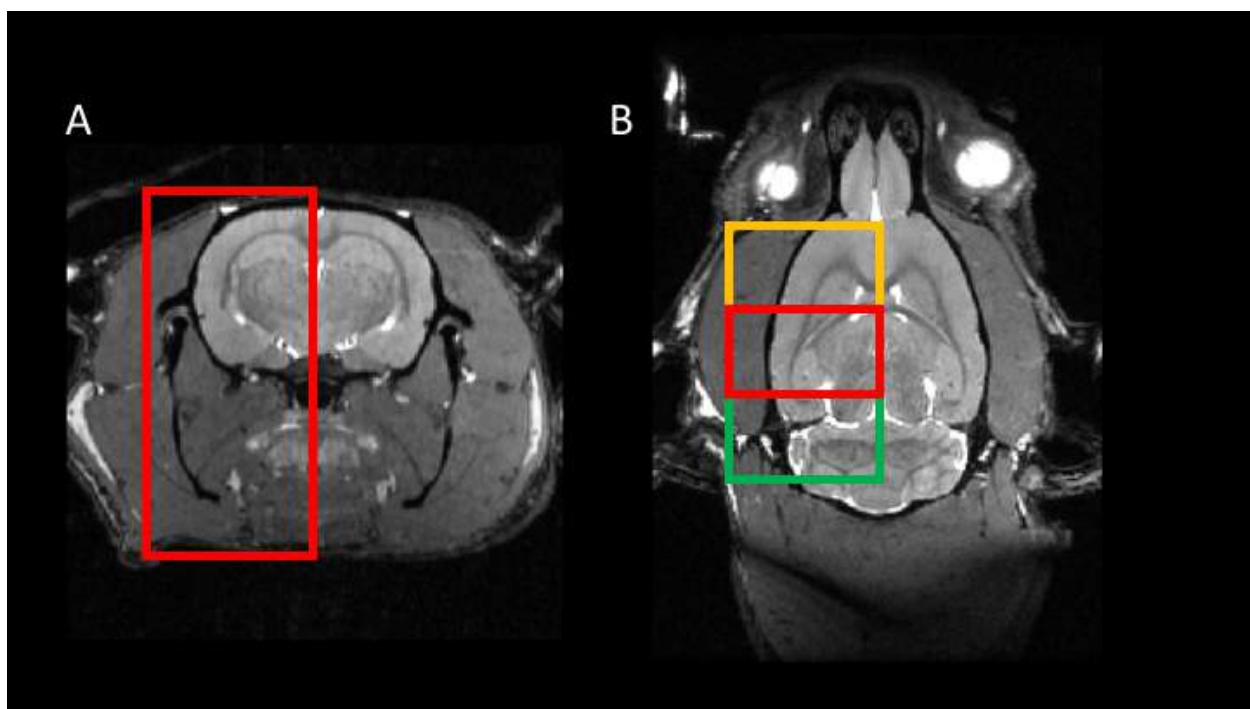
**Figure 3.1 Illustrative dose plan superimposed on bSSFP image. On the left is a
schematic dose distribution for animals irradiated on the xRad-225 platform up to**

40 Gy (n=10). On the right is a schematic of the dose distribution of the micro-CT platform. The red box indicates a dose of 30 Gy, the yellow box a dose of 20 Gy and green box a dose of 10 Gy.

The second platform used was an IGRT x-Rad 225 irradiation device. Dose rate was calculated to be approximately 2.3 Gy/min and the entire dose was delivered over 17.5 minutes using a 225 kVp beam. This resulted in a total dose of 40 Gy to the right half of the brain, delivered by a single appositional field directed superior to inferior through the brain. Dose planning was performed using custom-built Monte-Carlo analysis. Additionally, the x-Rad 225 had image localization allowing confirmation of the dose delivery to the right hemisphere. A schematic dose plan is also shown in Figure 3.1 (a). In both cases, a dose deposition gradient differential of approximately 5 Gy over the superior-inferior direction due to the kV-beam was calculated. Finally, control rats underwent sham radiation by being anesthetized for 15 minutes using similar conditions for irradiated rats.
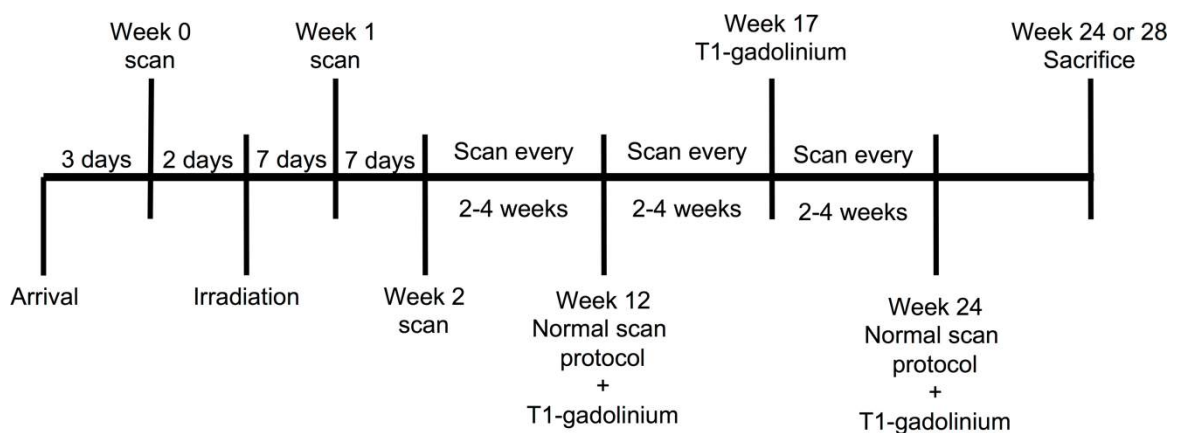
Figure 3.2 Illustrative timeline of protocol

3.2.4   Image Processing and Segmentation for Image Analysis

Manual segmentation was performed using the ITK-Snap software [32]. Any radiation-induced lesions, both hippocampi, and right hemispheric white matter were manually segmented. Lesions were segmented by using co-registered images of the gadolinium-enhancing T_1 image and the average image of all echoes. With the mutual information from both images, it was easier to exclude the CSF, striatum, and blood vessels surrounding the gadolinium-enhancing lesion.

Using the Oxford Centre for Functional MRI of the Brain Linear Image Registration Tool registration toolbox (FSL FLIRT), the segmented radiation necrosis region of interest was retrospectively overlayed on earlier time point images with registration errors no greater than 1-2 voxels. Proper registration was confirmed by using the contralateral internal/external capsule junction and anterior corpus callosum as a landmark. These retrospectively applied regions were used to determine if there were vascular changes detected with the R_2^* and SWI images at earlier time points that preceded the onset of frank necrosis.

Both left and right hippocampus were manually segmented, avoiding areas that were adjacent to the air-tissue interface. Finally, the white matter tracts (which included the corpus callosum and the internal and external capsule) were manually segmented. In all segmentation, the Paxinos atlas [33] was used as a guide. Care was taken to minimize partial volume effects.

3.2.5   SWI Processing

Before SWI processing, a four slice sliding window (convolution filter) was applied

along the direction of the magnetic field, which was also the direction of the slice

selection, as described by Haacke [34]. Following this step, high-pass filtering using a

7 mm Gaussian filter was applied and a weighted non-linear least squares fit through each

echo was used to obtain a local frequency shift map [35]. A cutoff frequency value of 17 Hz

was applied to get a frequency mask that was multiplied four times into the magnitude

data. Final SWI maps were then minimum intensity projected through 5 slices (875 µm).

3.2.6   Statistical Analysis

Statistical analysis was performed using Prism version 6.0h. The statistical analysis

compared irradiated rats to control rats using a repeated measures multiple comparison

two-way ANOVA using Sidak correction for multiple comparisons.

3.2.7   Histology

Following the last time point scan, rats were sacrificed by increasing the level of

isofluorane to 5% until there was no more response to stimuli and perfused using an

intracardiac catheter with a saline/heparin flush followed by 10% formalin solution. The

excised brain was placed in a 10% formalin solution for at least seven days before being

processed and blocked.

Standard tissue staining was performed at the adjacent hospital's pathology laboratory.

Tissues were block and stained with Hematoxylin and Eosin (H&E) and Luxol Fast Blue

(LFB). H&E is a histology stain that is commonly used for nuclei (stained by the

hematoxylin and viewed as blue or purple) as well as cytoplasm and erythrocytes (stained

by eosin and viewed as red or cherry red, respectively). LFB is a basic myelin stain used

to detect myelination within the central nervous system. Microscopy was performed

using an Aperio digital pathology slide scanner.

3.3   Results

3.3.1   Animal Behavior and weight

Animals irradiated using the micro-CT exhibited similar growth patterns compared to

control rats. Animals irradiated using the xRad-225 exhibited a slower weight gain

following irradiation; however, the weight gain was constant, and the animal's weight did

not vary by more than 15% compared to control. The mean weights and standard

deviations are shown in Figure 3.3.
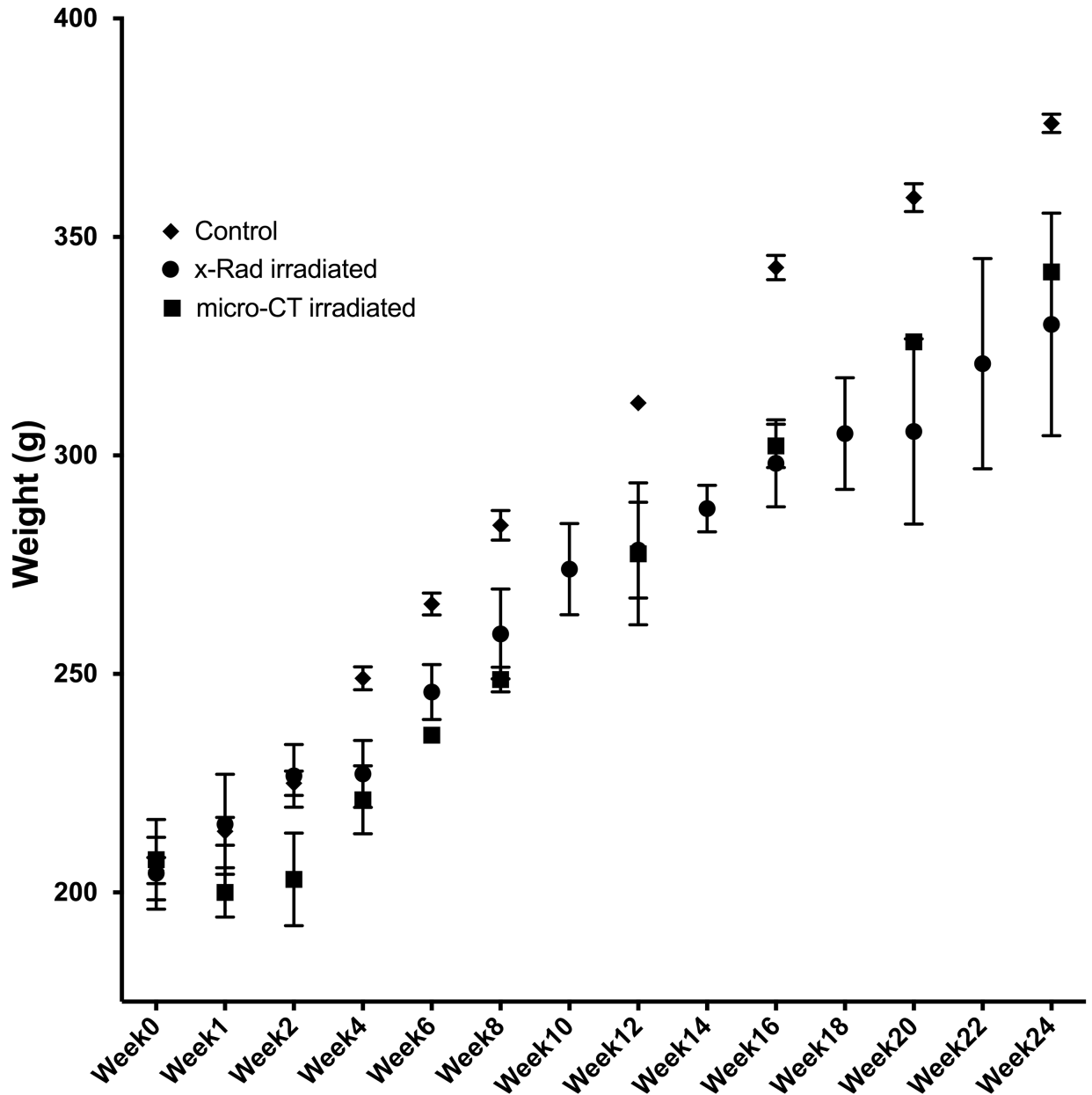
Figure 3.3 Graph of weight distributions with mean and standard deviations for each time point. Data points with no error bar indicate standard deviation smaller than the point.

Rats irradiated with the xRad-225 exhibited a hunched appearance towards the end of the experiments, but they did not exhibit other symptoms. The ipsilateral front incisors had to

be cut approximately 16 weeks following treatment for rats treated with the xRad-225 and subsequently trimmed every 2-4 weeks as necessary.

Only three rats that were irradiated with the xRad-225 survived until week 24. Originally, four rats were planned to be sacrificed along the timeline for histology, and three rats had to be sacrificed at earlier time points than planned due to weight loss. The specific source of weight-loss was due to refusal of water, food, or soft-mash in two rats, while one suffered from exsanguination from the ear on the irradiated side.

3.3.2   SWI and Gadolinium MRI

Throughout the study, there were no qualitative changes observed on the processed SWI images.

Gadolinium MRIs were performed on rats irradiated using the micro-CT before being sacrificed, and no rats demonstrated visible morphological changes. For rats irradiated with the xRad-225, morphological changes on Gadolinium MRI were apparent on all imaging sequences at week 24 as illustrated in Figure 3.4.
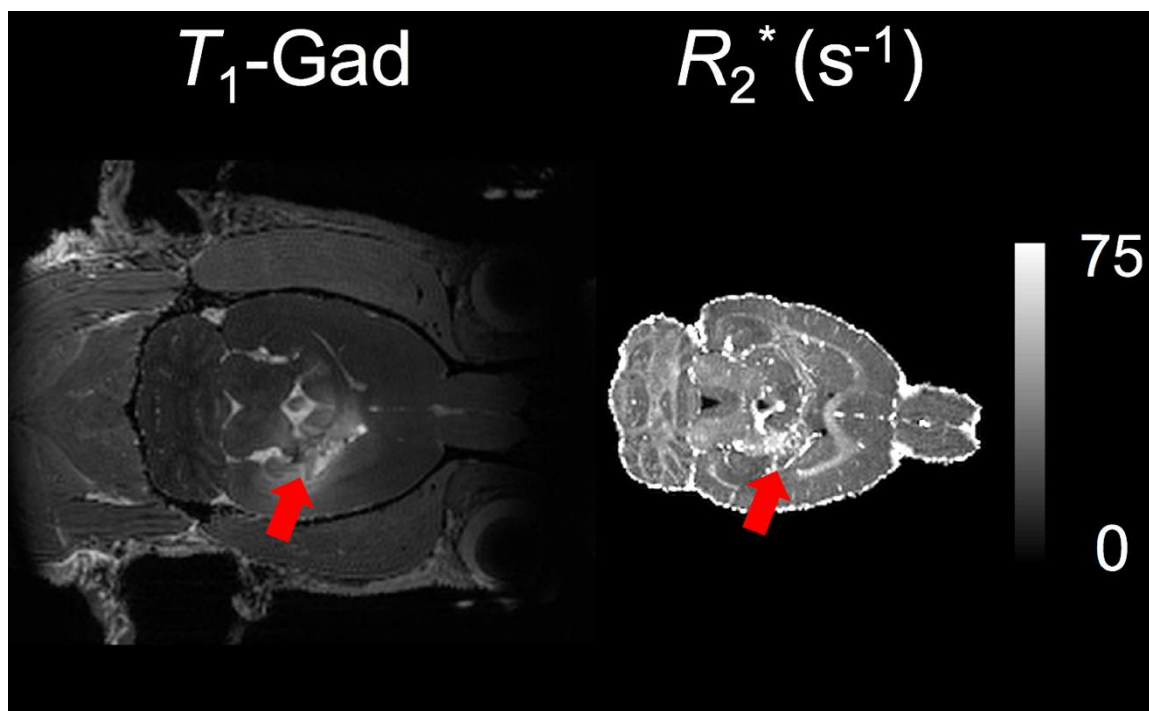
Figure 3.4 Radiation necrosis developed at the internal and external capsule, as shown by T_1-gadolinium enhancing MRI (a) and increased R_2^* (b).

The enhancing gadolinium lesion on MRI can be attributed to the breakdown of the blood-brain barrier due to radiation necrosis; this was subsequently confirmed by histologic examination (Figures 3.5 and 3.6).

3.3.3   H&E and Luxol Fast Blue Histology

While histology was performed on all three rat cohorts (Control, Micro-CT irradiated, and xRad-225 irradiated), only rats irradiated on the xRad-225 exhibited changes at later weeks as shown in Figures 3.5, 3.6 and 3.7. The Luxol Fast Blue stain shows hypointensities on Figure 3.5 and 3.6 indicated a loss of myelin content. The H&E stain also shows hypointensities indicating possible loss of tissue or disruption of the collagen. Vessel dilation was also apparent as early as week 16.
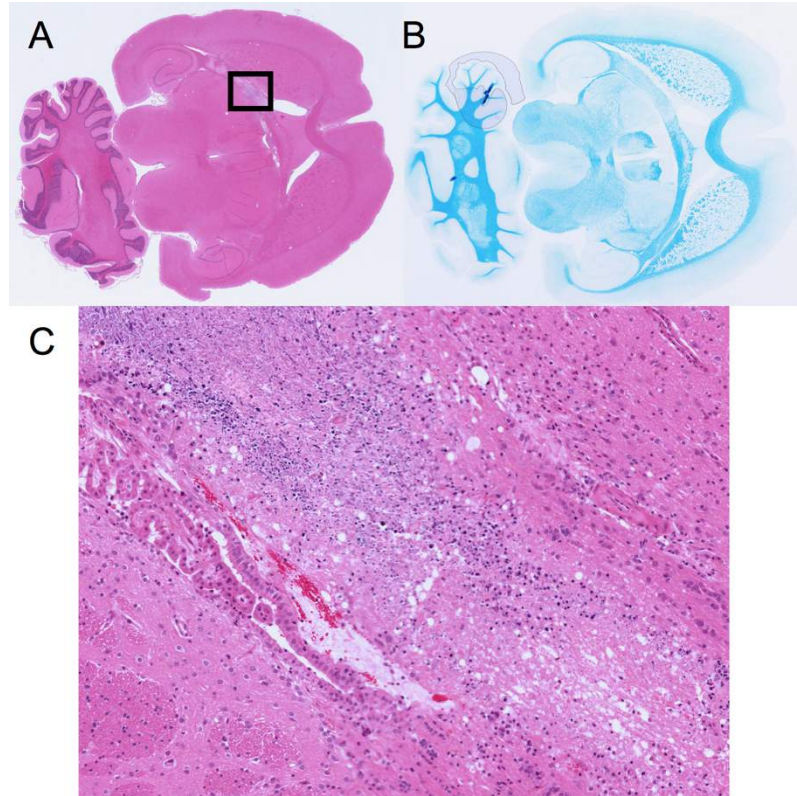
Figure 3.5 H&E stain (a) and LFB stain (b) demonstrating white matter necrosis within the internal capsule within the black box. Zoomed image of Internal Capsule (C) shows vessel dilation and hypointensity. Panels A and B are at 1x magnification; panel C is at 20x magnification.
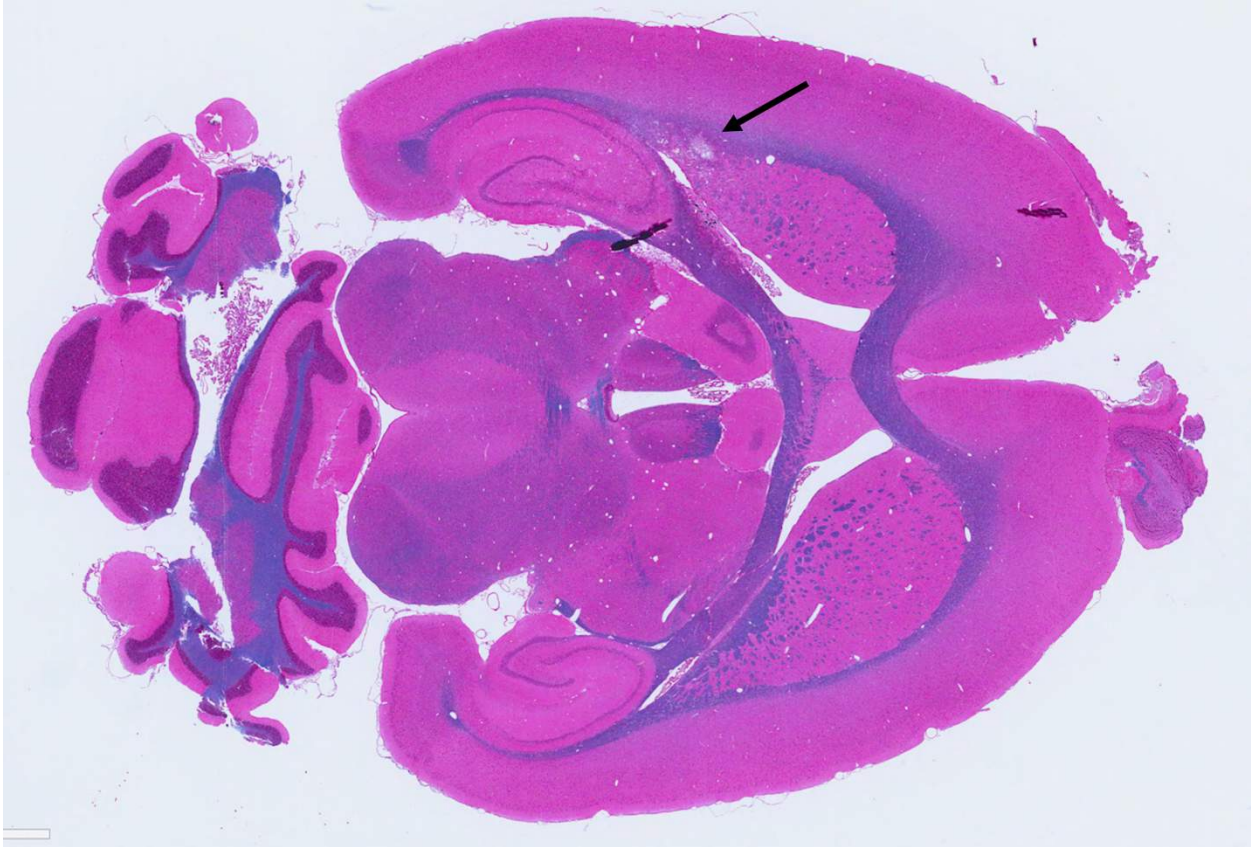
Figure 3.6 Combined H&E with LFB stain at week 20. Arrow indicates area of demyelination at the external capsule shown as hypointense purple.
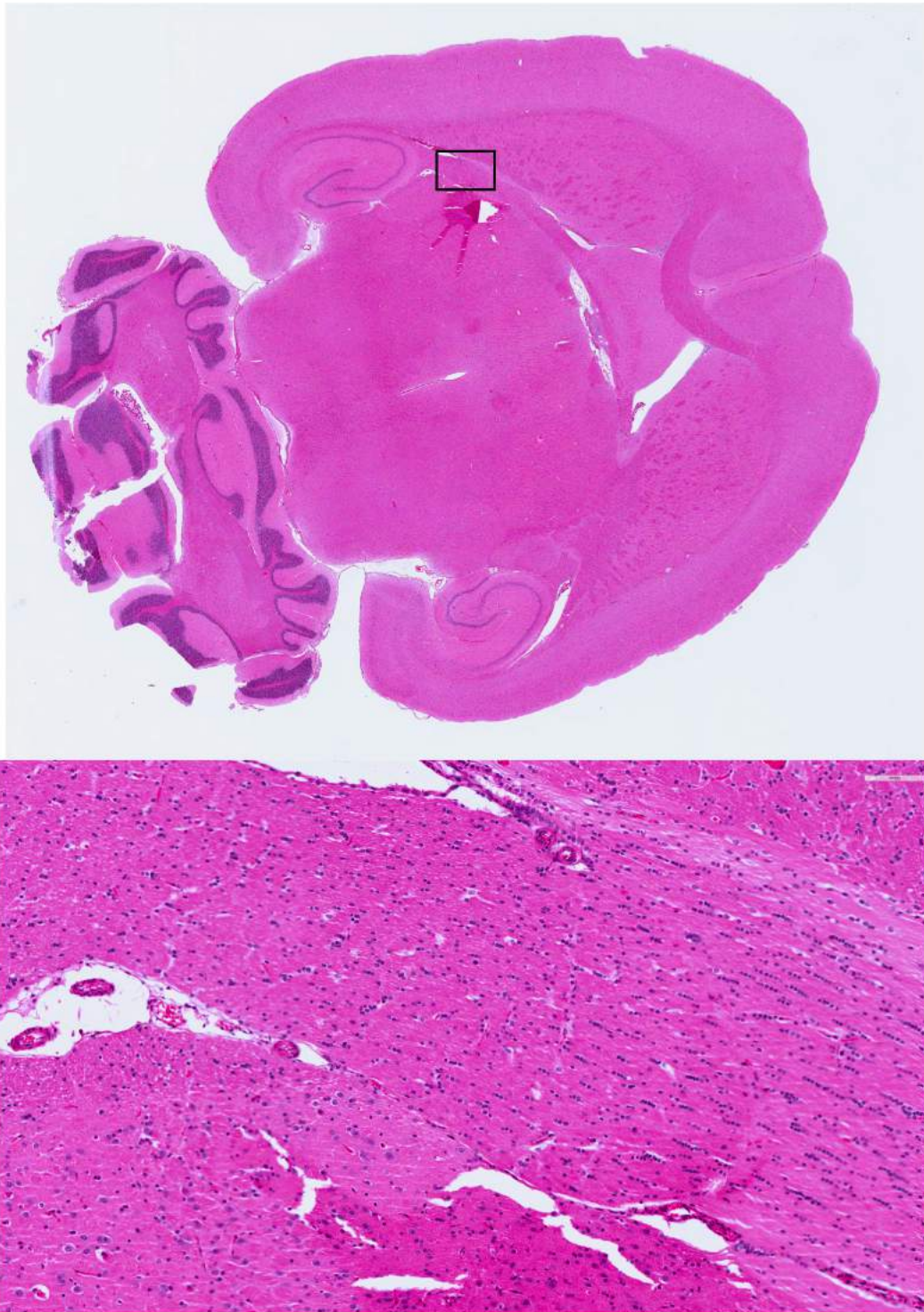
Figure 3.7 H&E slide for brain at week 16. Top is 1X magnification and bottom is 20X magnification

3.3.4 Differences in R_2^*

Rats irradiated on the micro-CT did not develop imaging evidence of necrosis nor were any statistically significant changes in R_2^* in the segmented normal tissue structures detected. The remaining results pertain to those rats irradiated on the xRad-225 platform or controls.

The raw R_2^* values within the region of eventual radiation necrosis in the three rats irradiated on the xRad-225 who survived until week 24 appear in Figure 3.8. An upward trend of R_2^* appears around the Week 14 time point, which was 8-10 weeks before any morphological changes appeared on the gadolinium-enhancing T_1 or bSSFP.
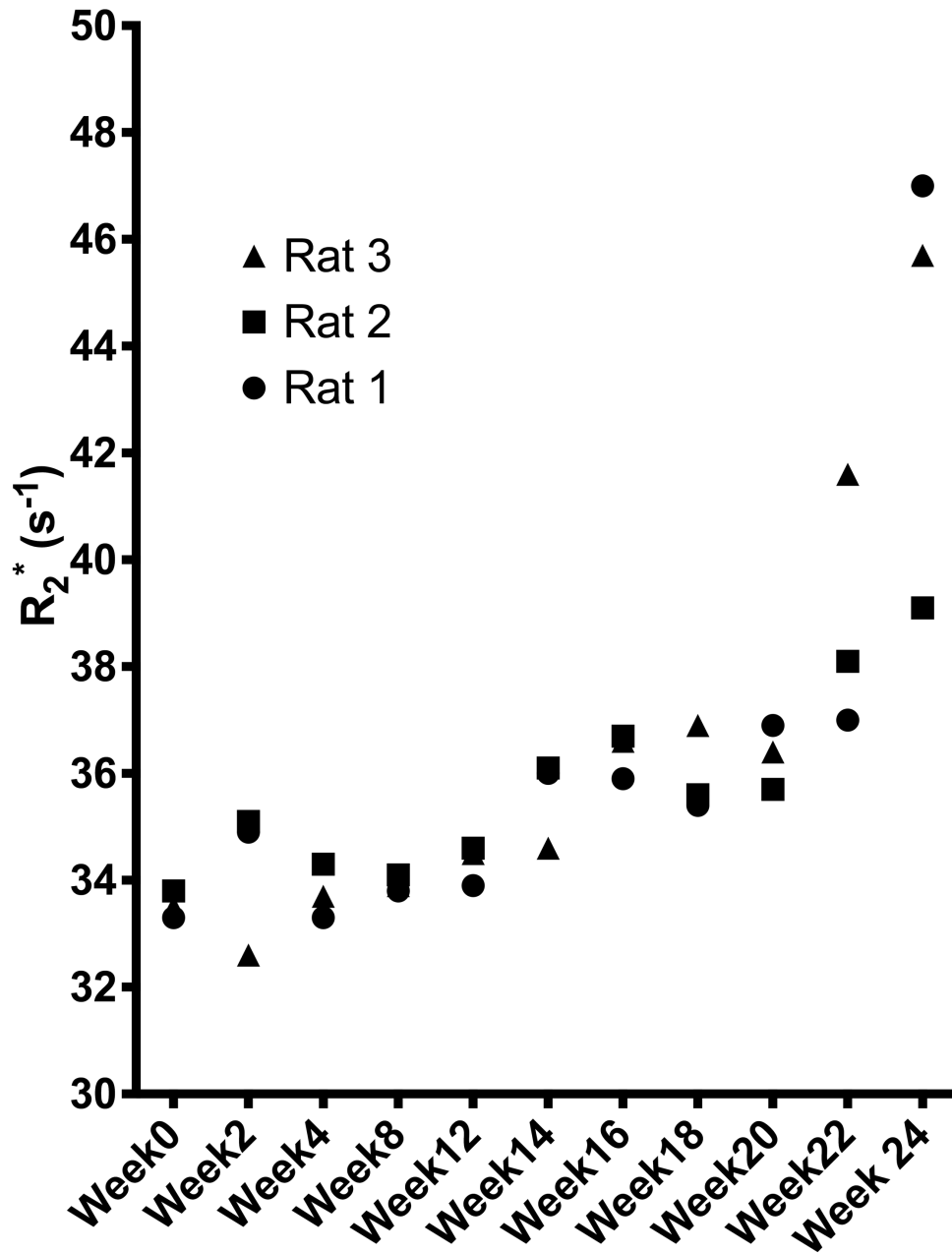
Figure 3.8 Measured R_2^* within lesion for each rat. An increasing trend of R2* is apparent as early as week 14.

The number of rats used for analysis in Figures 3.9, 3.10, 3.11, and 3.12 are provided in Table 3.1.

Table 3.1 Number of rats used in analysis

Week #	Number of Control rats	Number of Irradiated rats	Reason for loss of Irradiated Rat
0	4	10	X
1	4	10	X
4	4	8	1 Histology 1 Weight Loss
12	4	5	1 Histology 1 Weight Loss 1 Exsanguination from ear
16	4	5	X
20	4	4	1 Histology
24	4	3	1 Histology

Within the ipsilateral hippocampus, a statistically significant mean difference of R_2^* between control and irradiated rats occurred at week 12 (95% CI: 0.1-2.4 s^{-1}, $P < 0.05$) with significance at each subsequent time point as shown in Figure 3.9. In addition to differences between irradiated and control rats, a statistically significant mean difference between the ipsilateral and contralateral irradiated hippocampi within irradiated rats is evident at week 20 (95% CI: 0.5-3.0 s^{-1}, $P < 0.01$), as shown in Figure 3.10. There was no statistical significance for the mean difference between the left hippocampus in both irradiated and control rats, although a trend of increased R_2^* in the irradiated contralateral hippocampus is readily apparent as shown in Figure 3.11.
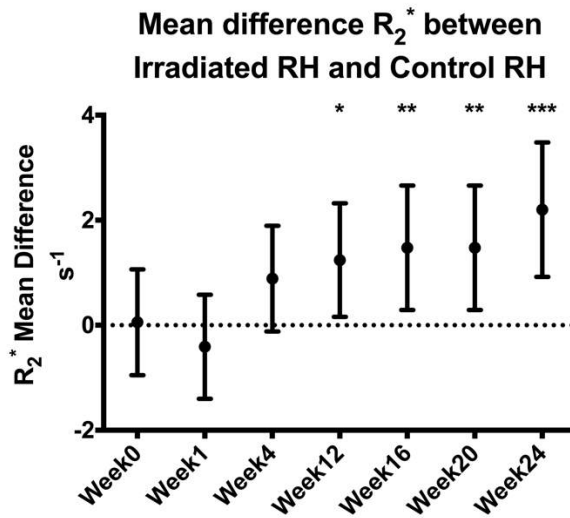
Figure 3.9 Mean difference of R_2^* between irradiated and control right hippocampus, error bars represent 95% confidence intervals, significance is represented by * $P < 0.05$, ** $P < 0.01$, *** $P < 0.001$.
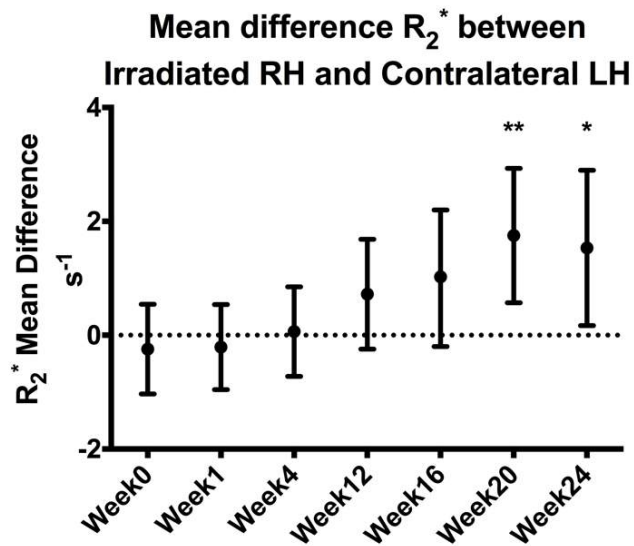
Figure 3.10 Mean difference of R_2^* between irradiated ipsilateral and contralateral hippocampus, error bars represent 95% confidence intervals, significance is represented by * $P < 0.05$, ** $P < 0.01$.
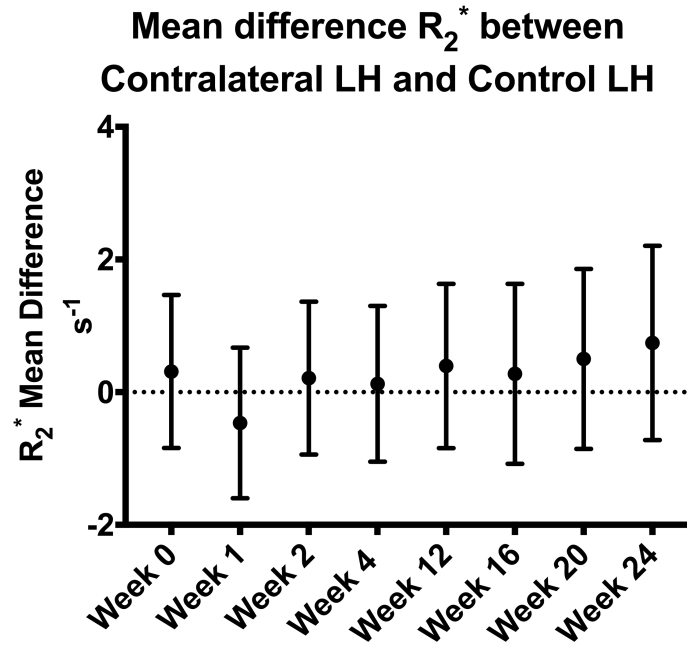
Figure 3.11 Mean difference of R2* between contralateral and control left hippocampus, error bars represent 95% confidence intervals. While there are no significant results, a weak trend of increasing R_2^* is apparent.

Within white matter tracts significant changes to the R_2^* between ipsilateral radiated and control white matter tracts were not apparent; however, a steady increase in the mean difference over time was observed as shown in Figure 3.12.

**Mean difference between
irradiated WM and control WM**
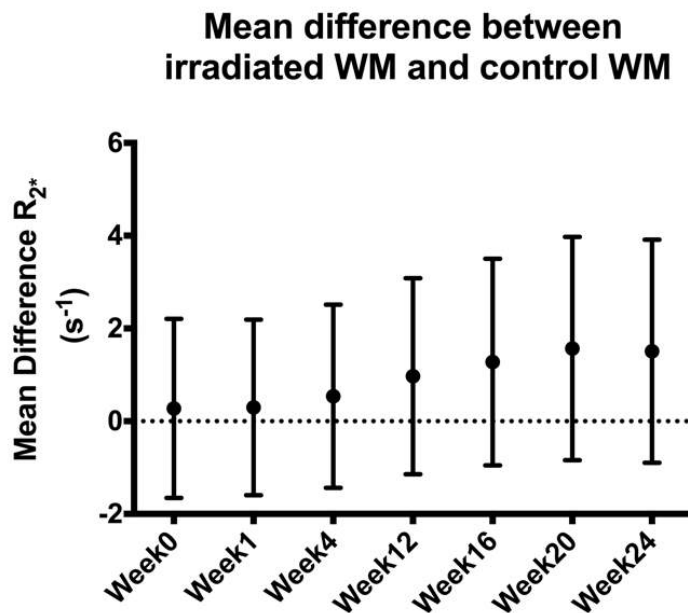
Figure 3.12 Mean difference of R_2^* between irradiated and control white matter tracts, error bars represent 95% confidence intervals. While there are no significant results, a trend of increasing R_2^* is apparent.

3.4   Discussion

This study has demonstrated a model in which increases of R_2^* in white matter tracts and hippocampus precede the morphological appearance of necrosis on gadolinium T_1-weighted imaging and bSSFP. In this specific cohort of rats, the R_2^* consistently increased in the external and internal capsule over time. This finding appears to be at odds with the vascular hypothesis, as an ischemic event in the irradiated area should be associated with a decreased R_2^* due to lower blood volume and blood flow in the region. Thus, the mechanism of RN may be more complex than radiation induced vascular injury and occlusion leading to ischemia. Increases in R_2^* could be indicative of vascular effects from neuroinflammation or vascular changes other than occlusion at the lesion site. Should small vessels be obliterated at the radiation site, as suggested by the vascular

hypothesis, residual by-products of vasculature (such as de-oxygenated hemoglobin) would increase the R_2^*. In fact, on histologic examination vascular dilation in the region where radiation necrosis was detected can be noted as early as week 16 as shown in figure 3.7, suggesting vascular effects are part of the mechanism, and further research is needed to relate changes on R_2^* to histology. If changes are happening at the capillary and small venules level, it is possible that the BOLD effect [36] of larger vessels dominate within a voxel due to the larger venules remaining intact as previously shown by histology [37], reducing the sensitivity to ischemic events in the capillaries. Additionally, it has been suggested small vessel changes occur in the hours or days following RT [11] and there are transient/variable changes in blood flow that may not have been detected with isolated imaging sessions.

While the data did not find any statistically significant changes in R_2^* within the white matter tracts, a trend towards an increase in R_2^* in white matter regions is apparent. Inter-week and inter-animal R_2^* differences of 1.5 s^{-1} were measured, which were attributed to partial volume during the segmentation. In most areas, the white matter tract was no wider than 2-3 voxels making proper segmentation difficult. It is possible that in humans, whose white matter tracts are larger and can span more voxels, longitudinal differences in R_2^* would be less sensitive to segmentation errors. The measured increase in R_2^* could be a neuroinflammatory mechanism in which there is increased iron content due to the presence of macrophages within the white matter tract. Further histologic examinations of the treated animals and examination among larger cohorts of animals would be needed to confirm this hypothesis.

The statistically significant increases in R_2^* within the hippocampus also support neuroinflammatory mechanisms within the hippocampus that have recently been suggested as mediating cognitive changes following radiation [38]. The decreased mean difference trend at week 1 could be supportive of decreased deoxygenated blood, again supporting the notion that RN is a complex process that evolves over time. The non-statistically significant trend of increased R_2^* within unirradiated hippocampus could be due to the high interconnectivity of the hippocampi along the corpus callosum. Larger cohorts and further immunohistochemistry investigations are necessary to identify the cause of this trend.

Of interest, the choice of radiation platform influenced the development of radiation injury. It is possible that the lower dose [39] or lower dose rate associated with the micro-CT (maximum 30 Gy at 30 cGy/min) compared to the xRAD-225 accounted for lack of RN lesions noted. Specifically, animals irradiated on the micro-CT at an effective dose rate of 3-5 mGy/min to 30 Gy partial brain volume did not develop any necrosis at 28 weeks after radiation, at which point they were sacrificed per the ethics protocol. It cannot be refuted that necrosis may have developed at a time point later than 28 weeks; however, this time point represents approximately 15-25% of the rats' expected lifetime, and previous established models of necrosis in rat occur between 18-26 weeks following RT [25,40,41]. In comparison, all animals irradiated on the xRAD-225 at 2.3 Gy/min to 40 Gy partial brain volume developed RN lesions. Thus, future studies examining RN in pre-clinical models should take into account dose rate as a potential confounding factor are warranted [42,43].

This study provides motivation for further research on the R_2^* dependence on RN, and further evaluations that correlate with histology and immunohistochemistry could provide further insight into the mechanisms increasing R_2^*. Given the small sample size of animals with RN, further validation of the findings in larger cohorts and alternate pre-clinical models are necessary. Another extension of this work would be to examine the utility of this imaging in pre-clinical models of glioma. In particular, these models could be used to explore whether RN can be differentiated from residual tumor using R_2^*.

3.5   Conclusions

In a pre-clinical model of RN, R_2^* acquired at 9.4T was able to detect early parenchymal changes that preceded the development of overt necrotic lesions. Variable temporal and spatial patterns of R_2^* suggest RN is a complex interplay between neuroinflammation and vascular and glial injury.

This chapter provided motivation for the future experiments within this thesis as data obtained suggest this technique is highly sensitive to increases in the vasculature and potentially neuroinflammatory components following RT. The next chapters will investigate whether changes in the vasculature are detectable in humans in the sub-acute and long-term time periods following therapy for both benign and malignant glioma. Chapter 4 will investigate vascular effects within the high dose regions of benign neoplasms and the subsequent effects it could have on the long-term health of these patients. Finally, Chapter 5 will investigate whether the differences in R_2^* as shown in this chapter can be applied to non-specific post-treatment imaging changes following chemoradiotherapy to differentiate between glioma recurrence and treatment effect.

3.6   References

1.   Tofilon PJ, Fike JR. The radioresponse of the central nervous system: a dynamic process. Radiat. Res. 2000; 153(4): 357–70.

2.   Shun Wong C, van der Kogel AJ. Mechanisms of Radiation Injury to the Central Nervous System: Implications fro Neuroprotection. Mol. Interv. 2004; 4(5): 273–284.

3.   Schultheiss TE, Kun LE, Ang KK, Stephens LC. Radiation Response of the Central Nervous System. Int. J. Radiat. Oncol. Biol. Phys. 1995; 31(5): 1093–1112.

4.   Lawrence YR, Li XA, el Naqa I, et al. Radiation dose-volume effects in the brain. Int. J. Radiat. Oncol. Biol. Phys. 2010; 76(3): S20–7.

5.   Gondi V, Tome WA, Mehta MP. Why avoid the hippocampus? A comprehensive review. Radiother. Oncol. 2010; 97(3): 370–6.

6.   Gondi V, Tolakanahalli R, Mehta MP, et al. Hippocampal-Sparing Whole-Brain Radiotherapy: A "How-to" Technique using Helical Tomotherapy and Linear Accelerator-Based Intensity-Modulated Radiotherapy. Int. J. Radiat. Oncol. Biol. Phys. 2010; 78(4): 1244–1252.

7.   Raber J, Rola R, LeFevour A, et al. Radiation-induced cognitive impairments are associated with changes in indicators of hippocampal neurogenesis. Radiat. Res. 2004; 162(1): 39–47.

8.   St. Clair WH, Adams JA, Bues M, et al. Advantage of protons compared to conventional X-ray or IMRT in the treatment of a pediatric patient with medulloblastoma. Int. J. Radiat. Oncol. Biol. Phys. 2004; 58(3): 727–734.

9.   Calvo W, Hopewell JW, Reinhold HS, Yeung TK. Time- and dose-related changes in the white matter of the rat brain after single doses of X rays. Br. J. Radiol. 1988; 61(731): 1043–52.

10. Schultheiss TE, Stephens LC. Permanent radiation myelopathy. Br. J. Radiol. 1992; 65(777): 737–753.

11. Greene-Schloesser DM, Robbins ME, Peiffer AM, Shaw EG, Wheeler KT, Chan MD. Radiation-induced brain injury : a review. Front. Oncol. 2012; 2(73): 1–18.

12. Shi L, Linville MC, Iversen E, et al. Maintenance of white matter integrity in a rat model of radiation-induced cognitive impairment. J. Neurol. Sci. 2009; 285(1-2): 178–184.

13. Hornsey S, Morris CC, Myers R. The Relationship between Fractionation and Total Dose for X Ray Induced Brain Damage. Int. J. Radiat. Oncol. Biol. Phys. 1981; 7(3): 393–396.

14. Atwood T, Payne VS, Zhao W, et al. Quantitative magnetic resonance spectroscopy reveals a potential relationship between radiation-induced changes in rat brain metabolites and cognitive impairment. Radiat. Res. 2007; 168(5): 574–581.

15. Raff MC, Miller RH, Noble M. A glial progenitor cell that develops in vitro into an astrocyte or an oligodendrocyte depending on culture medium. Nature. ; 303(5916): 390–6.

16. Nagayama K, Kurita H, Nakamura M, et al. Radiation-induced apoptosis of oligodendrocytes in the adult rat optic chiasm. Neurol. Res. 2005; 27346–350.

17. Zhou H, Liu Z, Liu J, et al. Fractionated radiation-induced acute encephalopathy in a young rat model: cognitive dysfunction and histologic findings. Am. J. Neuroradiol. 2011; 32(10): 1795–800.

18. Moravan MJ, Olschowka J a., Williams JP, O'Banion MK. Cranial irradiation leads to acute and persistent neuroinflammation with delayed Increases in T-cell infiltration and CD11c expression in C57BL/6 mouse brain. Radiat. Res. 2011; 176(4): 459–473.

19. Yoritsune E, Furuse M, Kuwabara H, et al. Inflammation as well as angiogenesis may participate in the pathophysiology of brain radiation necrosis. J. Radiat. Res. 2014; 55(4): 803–811.

20. Furuse M, Nonoguchi N, Kawabata S, Miyatake S-I, Kuroiwa T. Delayed brain radiation necrosis: pathological review and new molecular targets for treatment. Med. Mol. Morphol. 2015; 48(4): 183–190.

21. Perez-Torres CJ, Yuan L, Schmidt RE, et al. Specificity of vascular endothelial growth factor treatment for radiation necrosis. Radiother. Oncol. 2015; 117(2): 382–385.

22. Mullins ME, Barest GD, Schaefer PW, Hochberg FH, Gonzalez RG, Lev MH. Radiation necrosis versus glioma recurrence: Conventional MR imaging clues to diagnosis. Am. J. Neuroradiol. 2005; 26(8): 1967–1972.

23. Kumar AJ, Leeds NE, Fuller GN, et al. Malignant gliomas: MR imaging spectrum of radiation therapy- and chemotherapy-induced necrosis of the brain after treatment. Radiology. 2000; 217(2): 377–384.

24. Wang S, Wu EX, Qiu D, Leung, Lucullus HT, Lau H-F, Khong P-L. Longitudinal diffusion tensor magnetic resonance imaging study of radiation-induced white matter damage in a rat model. Cancer Res. 2009; 69(3): 1190–8.

25. Wang S, Tryggestad E, Zhou T, et al. Assessment of MRI parameters as imaging biomarkers for radiation necrosis in the rat brain. Int. J. Radiat. Oncol. Biol. Phys. 2012; 83(3): e431–6.

26. Perez-Torres CJ, Engelbach JA, Cates J, et al. Toward Distinguishing Recurrent Tumor From Radiation Necrosis : DWI and MTC in a Gamma Knife-Irradiated Mouse Glioma Model. Radiat. Oncol. Biol. 2014; 155365(314): 1–8.

27. Zhou J, Tryggestad E, Wen Z, et al. Differentiation between glioma and radiation necrosis using molecular magnetic resonance imaging of endogenous proteins and peptides. Nat. Med. 2011; 17(1): 130–4.

28. Haacke EM, Xu Y, Cheng Y-CN, Reichenbach JR. Susceptibility weighted imaging (SWI). Magn. Reson. Med. 2004; 52(3): 612–618.

29. Deistung A, Schäfer A, Schweser F, Biedermann U, Turner R, Reichenbach JR. Toward in vivo histology: a comparison of quantitative susceptibility mapping (QSM) with magnitude-, phase-, and R2*-imaging at ultra-high magnetic field strength. Neuroimage. 2013; 65(de): 299–314.

30. Wisnieff C, Ramanan S, Olesik J, Gauthier S, Wang Y, Pitt D. Quantitative susceptibility mapping (QSM) of white matter multiple sclerosis lesions: Interpreting positive susceptibility and the presence of iron. Magn. Reson. Med. 2015; 74(2): 564–570.

31. Jensen MD, Hrinivich WT, Jung J a., et al. Implementation and commissioning of an integrated micro-CT⁄RT system with computerized independent jaw collimation. Med. Phys. 2013; 40(8): 081706.

32. Ibanez L, W S, Ng L, Cates J. The ITK Software Guide. 2003.

33. Paxinos G, Watson C. The Rat Brain 6th edition. .

34. Haacke EM, Reichenbach JR. Susceptibility Weighted Imaging in MRI: Basic Concepts and Clinical Applications. .

35. Quinn MP, Gati JS, Klassen LM, et al. Comparison of multiecho postprocessing schemes for SWI with use of linear and nonlinear mask functions. Am. J. Neuroradiol. 2014; 35(1): 38–44.

36. Ogawa S, Lee T. Brain magnetic resonance imaging with contrast dependent on blood oxygenation. Proc. Natl. Acad. Sci. 1990; 87(24): 9868–72.

37. Brown WR, Thore CR, Moody DM, Robbins ME, Wheeler KT. Vascular damage after fractionated whole-brain irradiation in rats. Radiat. Res. 2005; 164(5): 662–8.

38. Jenrow KA, Brown SL, Lapanowski K, Naei H, Kolozsvary A, Kim JH. Selective

Inhibition of Microglia-Mediated Neuroinflammation Mitigates Radiation-Induced Cognitive Impairment Kenneth. Radiat. Res. 2013; 179(5): 549–556.

39.   Jiang X, Yuan L, Engelbach JA, et al. A Gamma-Knife-Enabled Mouse Model of Cerebral Single-Hemisphere Delayed Radiation Necrosis. PLoS One. 2015.

40.   Stockham AL, Tievsky AL, Koyfman SA, et al. Conventional MRI does not reliably distinguish radiation necrosis from tumor recurrence after stereotactic radiosurgery. J. Neurooncol. 2012; 109(1): 149–58.

41.   Kumar S, Arbab AS, Jain R, et al. Development of a novel animal model to differentiate radiation necrosis from tumour recurrence. J. Neurooncology. 2012; 108(3): 411–420.

42.   Moiseenko V, Duzenli C, Durand RE. In vitro study of cell survival following dynamic MLC intensity-modulated radiation therapy dose delivery. Med. Phys. 2007; 34(4): 1514–1520.

43.   Moiseenko V, Banáth JP, Duzenli C, Olive PL. Effect of prolonging radiation delivery time on retention of gammaH2AX. Radiat. Oncol. 2008; 318.

Chapter 4

4 Assessing Vasculature and Microstructural Changes in Low-Grade and Benign Brain Tumors Using Ultra-High Field MRI Techniques

4.1 Introduction

External beam radiotherapy (RT) is commonly employed as a treatment for many brain neoplasms. In benign and low-grade neoplasms (meningiomas, neuromas, low-grade gliomas), safe maximal surgical resection combined with RT is usually the standard of care. The prescribed dose is typically a course of 54-60 Gy in 30 fractions using conformal delivery with techniques such as intensity modulated radiation therapy. These dose plans attempt to follow specific guidelines such as QUANTEC to limit dose to radiosensitive areas such as the uninvolved brain, brain stem, optic nerve, and optic chiasm [1], as well as the hippocampus that is known for its role in neurogenesis [2,3]. Due to the infiltrative nature of some neoplasms such as low-grade gliomas or the proximity of tumors to normal brain in other neoplasms, even conformal radiation techniques can result in some volumes of normal tissue receiving radiation. The dose delivered to the normal brain can potentially cause long-term effects later in the patient's life.

Following RT, there are numerous reports of clinical sequela that are classified into acute, early-delayed, or late-effects [4]. Acute and early-delayed side-effects are usually temporary and resolve spontaneously with minimal treatment or steroids. Late-effects are typically much more severe as they cause permanent changes to the brain parenchyma that include radiation necrosis (RN), cavernous angiomas, and microbleeds [4] resulting in ongoing neurologic deficits.

RN is a side-effect that may present itself a few years following RT; however, it can occur as early as six months and as late as ten years following RT. In some patients, regions of RN may be small and do not produce symptoms. In others, progressive RN can be seen with significant effects on the patient's quality of life [5]. Symptoms ranging from headaches and drowsiness to memory loss, seizures, and focal deficits have been documented. Treatments of RN range from observation to steroids or anti-angiogenic agents [6]. In some patients, surgical resection is required to debulk necrotic areas to alleviate symptoms.

The exact cause and time-course of RN is not fully understood, but the two main hypotheses developed in the past 50 years are related to vascular and glial damage [4]. The vascular hypothesis suggests that radiation necrosis is secondary to an ischemic event, while the glial hypothesis suggests that white matter precursor cells are damaged during RT. Recently, the role that the immune response plays following RT has been documented [7,8]. The theory proposes that neuroinflammation could be another mechanism contributing to the development of RN.

In addition to frank RN, microbleeds that occur at later time-points and are detected on imaging following RT are a recent discovery [9,10]. Microbleeds may serve as a marker for future vascular disease such as stroke [11]. Not only do microbleeds indicate that more serious diseases could occur in the future, but the patient could be put at risk of more significant intracranial bleeding if started on anticoagulants [12]. Techniques such as Susceptibility-Weighted Imaging (SWI) are becoming more prominent with higher magnetic field strengths available clinically (3T) or for research ($\geq$7T). These techniques make locating microbleeds increasingly easier, as the spatial resolution can be increased

with higher magnetic fields and the paramagnetic effect of the hemosiderin deposit increases linearly with field strength. Consequently, the increased resolution can also lead to false-positives in microbleed detection as small venous vasculature that runs parallel to the magnetic field can be misinterpreted as microbleeds. SWI, Quantitative Susceptibility Mapping (QSM) and apparent transverse relaxation (R_2^*) have been previously shown to be extremely sensitive to the vasculature and hemosiderin rich microbleeds [13,14]. These techniques are also sensitive to white matter lesions, as shown in various multiple sclerosis (MS) studies [15,16]. Previous work from Raichenbaich et al. [17] estimates that these techniques are sensitive to venous vasculature of approximately 100-200 micrometers in diameter.

Among brain tumor patients, most studies to date have investigated microbleeds and radiation necrosis among patients who have high-grade neoplasms [18,19]; however, long-term RN studies in this patient population may be less feasible due to the shortened life expectancy for most patients with malignant glioma. Additionally, these studies involve patients who are treated with chemotherapy, which has been shown potentially to influence the number of microbleeds present in the brain [10,20] and may confound the estimates of microbleeds due to radiation alone.

This research study presents initial results that focus on imaging the microvasculature and microbleeds using techniques such SWI, QSM, and R_2^* on patients treated for benign or low-grade neoplasms. These patients have a longer overall survival (OS) following successful treatment and as such are at higher risk of eventually experiencing delayed adverse RT effects. Thus, it is hypothesized that SWI, QSM, and R_2^* may be a useful imaging technique to detect late radiation changes among this patient population and in

doing so, identify patients who might be at risk of longer-term sequelae of their treatment (cognitive effects or focal brain injury).

4.2   Materials and Methods

4.2.1   Patient Recruitment

The study was approved by the Human Subjects Research Ethics Board of the University of Western Ontario. Ten patients (two males, eight females) were recruited from the London Regional Cancer Program (LRCP) and were screened for eligibility by the treating radiation oncologist. Eligibility requirements included patients who were over 18 years old, Karnofsky Performance Status > 60, and who were treated for a benign or WHO Grade 1 or 2 brain neoplasm within 12-36 months of their recruitment for the study. Treatments for their neoplasms could have included surgical resection followed by radiotherapy or primary radiotherapy alone. As per protocol, patients underwent an initial imaging session at the time of enrollment and a second session 12-24 months later to detect any change in imaging features.

4.2.2   MRI

Patients were scanned on a 7T MRI at the Robarts Research Institute in London, Ontario. The first MRI for all patients was performed on an Agilent/Siemens 7T MRI with a 15 channel transmit / 31 receive channel coil. Three of the patients had their second carried out after a major upgrade to a Siemens 7T Magnetom Step 2.3 MRI with an 8 channel transmit / 32 receive channel coil while three patients had both MRIs on the Agilent scanner. An anatomical T_1-weighted image was performed (Agilent: MPRAGE, 1 mm isotropic voxel, scan time 5 min 45 seconds / Siemens: MP$_2$RAGE, 0.8 mm isotropic

voxels scan time 8 minutes 26 seconds) and a CSF attenuated MPFLAIR (Agilent: 1 mm isotropic resolution, scan time 12 minutes 42 seconds, SEIMENS: not acquired) was acquired for registration to clinical scans. A multi-echo gradient echo (Agilent: Multi-echo gradient echo, 1 mm in-plane resolution, 1.5 mm slices, TR=40 ms, TE=2.4 ms, ESP=3.3 ms, echoes=6, FA 13° GRAPPA 2.1 / Siemens: Multi-echo gradient echo, 1 mm in-plane resolution, 1.5 mm slices, TR=40 ms, TE=4.9 ms, ESP=4.5 ms, echoes=6, FA 13°, GRAPPA 2) was acquired.

4.2.3   Post Processing

The multi-echo gradient echo data set was acquired and post-processed into SWI, R_2^* and QSM maps using in-house software. The implementation of QSM used a pre-conjugate gradient method and was compared to QSM using the MEDI toolbox [21]; however, the data from the Agilent scanner was not optimized for MEDI processing. R_2^* was computed using a non-linear least squares mono-exponential fit with a voxel spread function for correction [22]. An 11-mm Gaussian high-pass filter was used to filter the phase and the phase was fit with respect to TE using a weighted non-linear least squares function to calculate the local frequency shift map. A frequency-mask of 15 Hz was then applied to an average magnitude image from all echoes to create SWI. Finally, MATLAB (The MathWorks Inc. Natick, MA) was used to create a minimum intensity projection image (mIP) through 7 mm (7 slices) of the SWI.

4.2.4   Dose Plan Overlay

Treatment dose plan, as well as planning CT and MRIs, were retrieved from the LRCP

and were registered to the research MRI using FSL's FLIRT toolbox [23]. CERR [24] was

used to export the dose plan.

4.2.5   Microbleed counts, Vasculature and White Matter
Abnormalities

Images (SWI, MPRAGE, and FLAIR) were reviewed by a neuroradiologist blinded to the

history of the patient. The neuroradiologist was asked to count the microbleeds on all

images and assess for vasculature and white matter abnormalities.

Once identified, the microbleeds were segmented on the SWI using ITK-snap [25] for

analysis using R_2^* and QSM.

4.3   Results

4.3.1   Clinical Findings

Ten patients consented to imaging and were enrolled in the study. A full description of

their cases, treatment, and current clinical status is provided in Table 4.1. A mini-mental

status exam (MMSE) was performed at the first visit and a mean score of $29/30 \pm 0.9$

indicated patients were grossly cognitively intact at assessment. Patients were imaged at a

mean of 26.7 ± 7.5 months following their treatment, and six of ten patients returned for a

second MRI between 12-24 months (17.3 ± 7.3) following their first MRI. Four patients

did not return for this second scan. Two patients became ill for unrelated health reasons;

one patient opted not to return for their second research scan and one patient's low-grade

glioma evolved into a malignant glioma, and their clinical condition precluded reimaging.

Table 4.1 Patient Clinical Status. DNR indicates did not return, V1 indicates Visit 1, V2 indicates Visit 2.

Patient/Sex	Age at time of treatment	Diagnosis	RX (Gy/Fraction)	Time btw RT-V1/ Time btw V1-V2 (months)	Current Clinical Status
1 (F)	29	WHO Gr. 2 Meningioma Rt. Sphenoid Wing	Surgery + 60/30	30/11	Employed Part-time. Aug 2015 MRI stable post surg. Changes and post-RT WM changes.
2 (F)	32	Midline Recurrent Atypical Meningioma	Surgery + 66/30	14/DNR	Stable MRI findings no evidence of progression, stable residual masses next to treated area.
3 (F)	57	WHO Gr. 1 Meningioma occipital region	Surgery + 54/30	30/DNR	Asymptomatic from meningioma, no evidence of recurrence, unrelated thyroid treatment.
4 (F)	57	Craniopharyngioma	54/30	13/14	Reduction in size of craniopharyngioma, stable FLAIR hyperintensities in the hippocampi bilaterally.
5 (F)	57	Left acoustic neuroma and posterior fossa meningioma	Surgery + 54/30	23/10	Working full time, occasional dizziness bending over or working on ladders. Stable right cerebellopontine angle meningioma.
6 (F)	63	Meningioma of the left sphenoid wing	Surgery + 66/30	17/22	Retired, well with no symptoms and no evidence of progression/recurrence on MRI.
7 (F)	55	Brain Stem Glioma WHO Gr. 1	54/30	23/22	Elevated prolactin due to pituitary dysfunction, possible treatment effect. Some facial twitching similar to initial presentation of tumor, but not requiring treatment. Near complete response.
8 (M)	33	Recurrent Meningioma of base of skull	54/30	20/12	Working full time with mild fatigue. Short term memory problems, history of WBRT for ALL in 1982.
9 (M)	50	Left posterior fossa meningioma	60/30	14/DNR	Stable on follow-up imaging with decreasing enhancement in cerebellum.
10 (F)	45	Left temporal lobe Mixed oligoastrocytoma WHO Gr. 2	60/30	14/DNR	Developed glioblastoma, no follow-up.

4.3.2   Imaging Findings

4.3.2.1   Venous Vasculature

On a whole, no gross abnormalities or venous vessel density discrepancies were observed

on the SWI. One patient (Patient 8) had a cavernous angioma that had been previously

detected on conventional MRI before enrollment in this study.

4.3.2.2   Microbleeds

Six of ten patients had microbleeds on the post radiation imaging. All microbleeds

occurred in areas of high dose (>45 Gy). Some microbleeds resolved between the initial

and follow-up scan. The full list of microbleeds is reported in Table 4.2. In all patients,

microbleeds had an R_2^* greater than 80 s^{-1} and QSM values lower than -250 ppb. Most

microbleeds had a halo artifact as shown in Figure 4.1 that aided in their detection.

Table 4.2 Microbleed count per visit.

Patient	Visit 1 Microbleeds	Visit 2 Microbleeds	New Microbleeds	Resolved Microbleeds
1	7	4	2	5
2	5	X	Did not return	Did not return
3	4	X	Did not return	Did not return
4	0	0	0	0
5	2	2	0	0
6	2	0	0	2
7	0	0	0	0
8	0	0	0	0
9	1	X	Did not return	Did not return
10	5	X	Did not return	Did not return
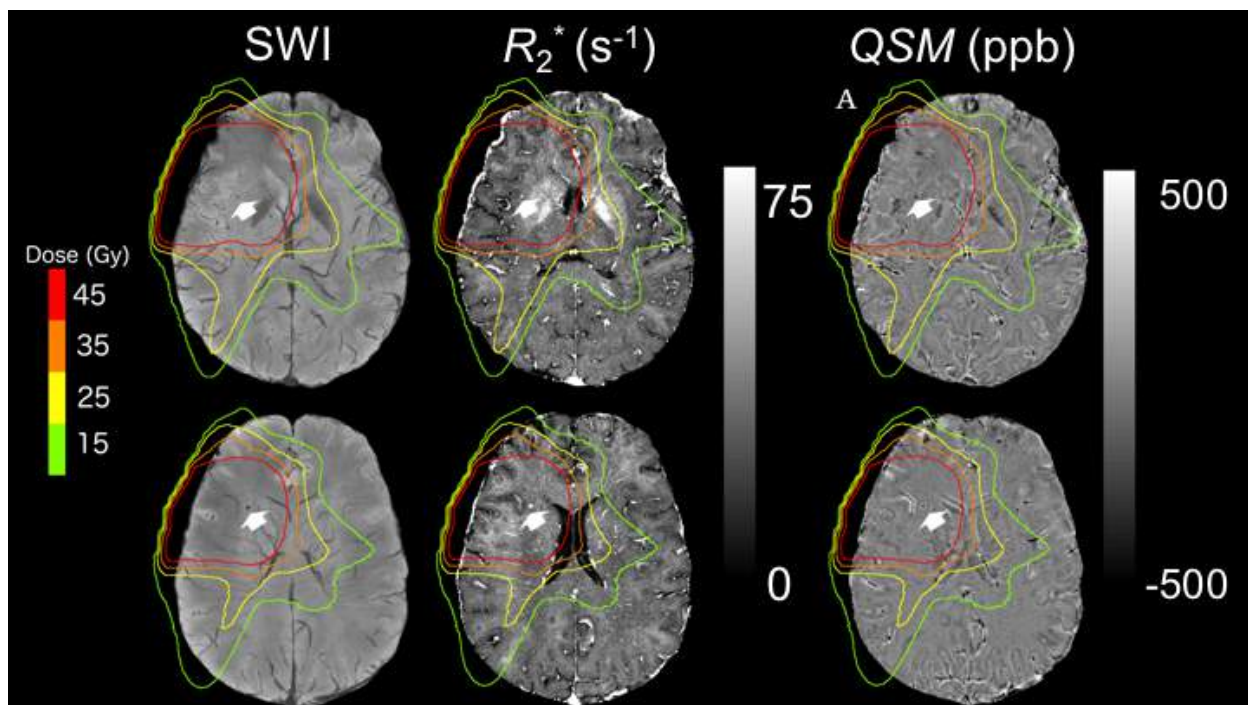
Figure 4.1 Illustration of microbleeds (white arrow) for Patient 1 in optic tract's (top row) and lobar microbleed (bottom row). The mIP SWI image shows venous vasculature in areas of high dose similar to the contralateral area.

4.3.2.3   White Matter Abnormalities

Three patients had periventricular or lobar lesions on their MPRAGE and FLAIR images

in the mid (>30 Gy) to high dose (>45 Gy) regions consistent with white matter changes

reported after RT [26,27]. Upon examination of the post-processed QSM and R_2^* images, the

periventricular white matter lesions have less volume than on FLAIR and MRPAGE

(Figures 4.2 and 4.3), and this has been documented previously in literature as FLAIR

tends to overestimate the amount of white matter change especially in the periventricular

lesions [28]. The lesions' low R_2^* strongly suggests demyelination, but the patients in this

series were asymptomatic. Therefore, the clinical relevance and future clinical course of

these white matter findings is unknown, although others have reported the presence of

asymptomatic white matter changes on long-term follow-up after radiotherapy. An

interesting observation is that these lesions have penetrating veins, as can be seen in

Figure 4.2, 4.3, and 4.4 as is often seen in MS.
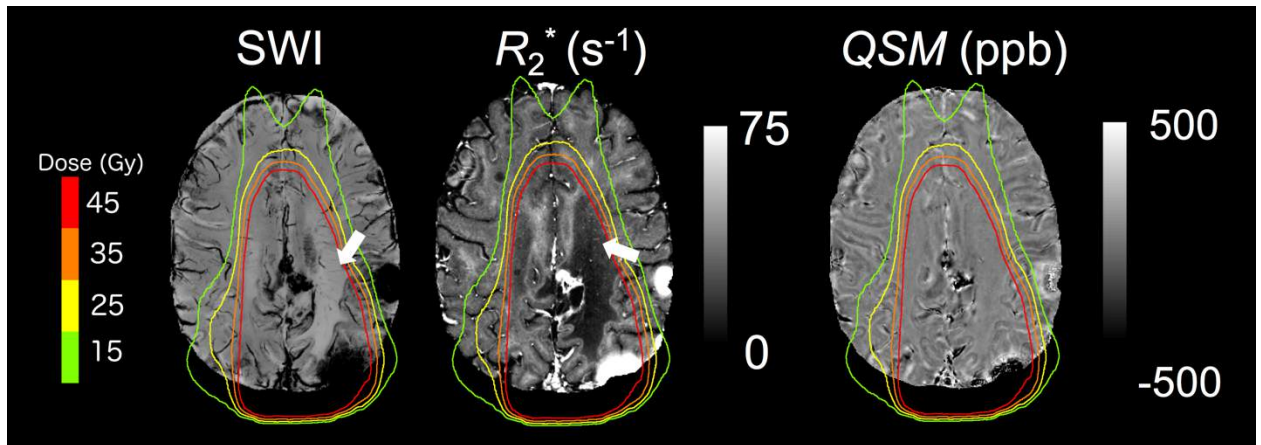
Figure 4.2 Patient 2 showing areas of residual tumors near midline as well as white matter damage in high dose regions. Venous vasculature is apparent in damaged white matter on R_2^* and SWI as shown by the white arrows.
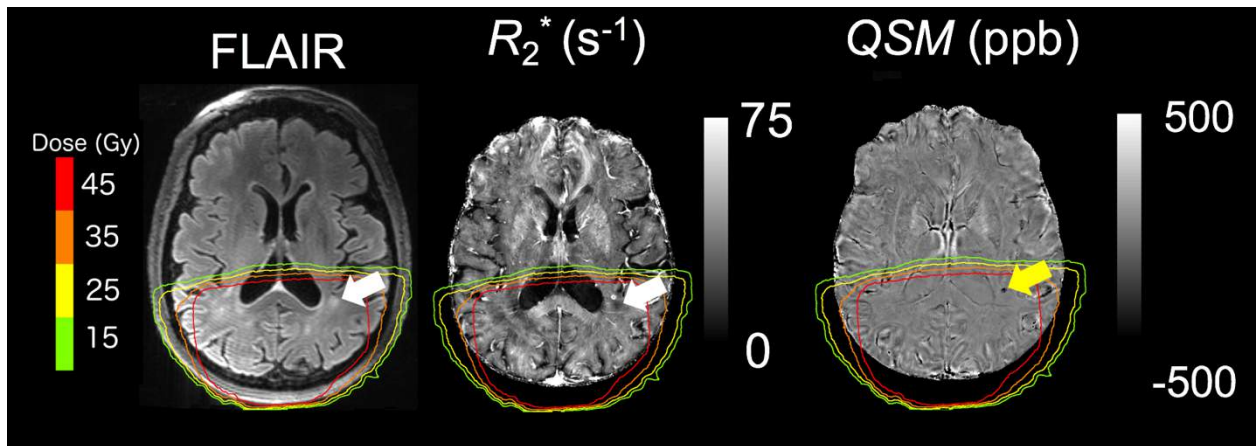
Figure 4.3 Patient 3 showing periventricular lesions that appear to be venocentric as indicated by the white arrow on FLAIR (hyperintense) and R_2* (hypointense). Adjoining to the lesion, a microbleed is evident on $R_2{}^*$, which is indicated by a yellow arrow on QSM
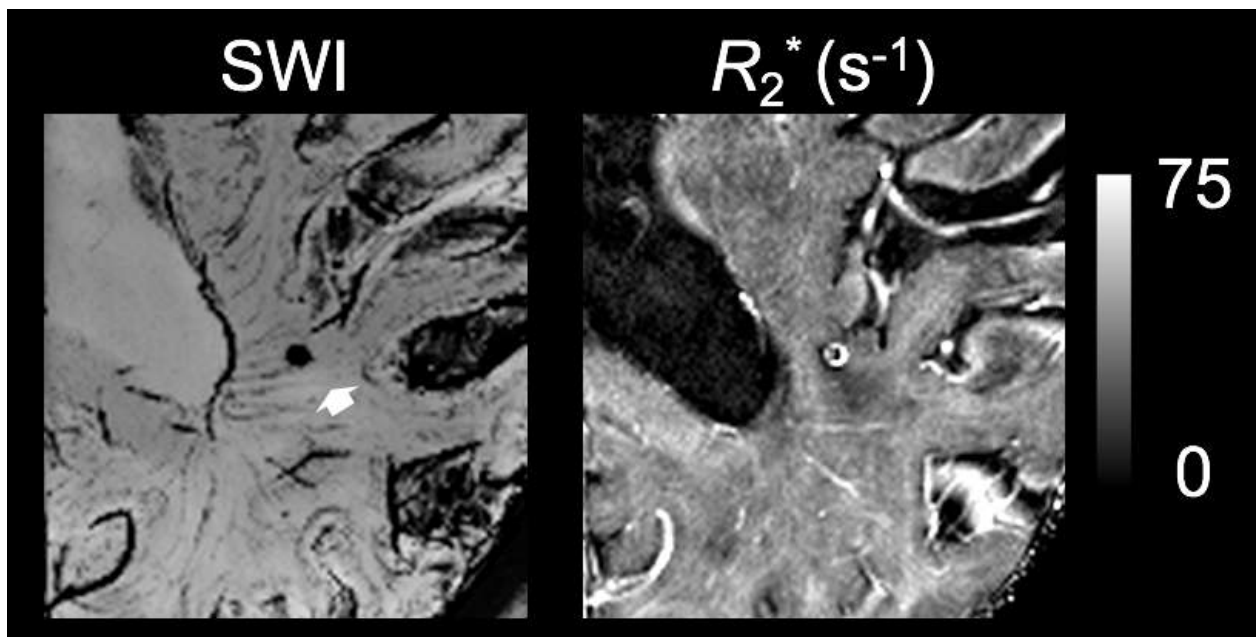
Figure 4.4 Zoom in on Figure 4.3, where the microbleed is apparent on SWI and $R_2{}^*$ and the venocentric lesion is indicated with white arrow.

4.3.2.4 Current Clinical Status

As shown in Table 4.1, most patients who enrolled in this study are clinically stable following treatment for their neoplasms. Aside from Patient 10, who developed a glioblastoma, their symptoms are not directly related to their diagnosis or treatment.

4.4 Discussion

It is believed that this is the first study that investigates vasculature and white matter in patients who have been treated for low-grade or benign neoplasms with radiation and surgery only. The potentially long survival of this patient population post-treatment increases the chance that they may experience late radiation side-effects compared to patients with higher grade lesions. Imaging biomarkers that could identify patients at risk of delayed radiation sequelae could be useful in this patient population to refine radiation delivery techniques and to explore mitigating strategies like pharmacologic interventions [29].

The main focus of this study was to determine what effect RT would have on the normal parenchyma during the late-effect time window (3-5 years after therapy). Gross abnormalities were not expected, as these patients were clinically stable and on conventional imaging, but it was hypothesized that it could be possible to detect subclinical lesions in the brain receiving significant doses of radiotherapy. The detection of these subclinical lesions may be useful for future time points should these subclinical lesions develop into necrosis. Therefore, this warrants further studies of a longer period for this patient subset. It is known that microbleeds appeared in patients treated with chemotherapy or radiotherapy for high-grade neoplasms [10]. Additionally, Liu et al.

demonstrated the ability to distinguish microbleeds from venous vasculature using quantitative methods [17]. Therefore, an investigation into the occurrence of microbleeds and demyelinating lesions as a potential imaging biomarker of late radiation effects in patients treated for low-grade brain neoplasms was performed.

In this cohort, six of ten patients showed microbleeds within the high dose regions and in five of six patients, no microbleeds were observed outside the high dose region. Long-term follow-up is required to correlate with clinical endpoints like future vascular incidents or cognitive side-effects to determine if microbleed monitoring could be of significant importance in these patients.

Although these patients do not have the number of microbleeds as shown in other studies of high-grade neoplasms, the appearance of microbleeds is indicative of endothelial damage within the high dose region. This suggests the importance of long-term monitoring in this low-grade cohort as these patients could be at a higher potential for symptomatic vascular or cognitive changes later in life [30,31]. The appearance of microbleeds could also indicate that further studies are required to look at the effect of anticoagulants. Certain studies have already shown that appearance of microbleeds in other disease states could be a contraindication for use of anticoagulants [32] and these findings suggest strategies attempting to limit radiation injury through the use of anti-platelet agents or anti-coagulation in this patient population should be evaluated cautiously.

Further to venous vasculature being present in high dose regions, veins within demyelinated lesions in the area of high doses can be observed. This is a common finding

in MS and acute disseminate encephalomyelitis [33]. The white matter lesions have previously been reported in the past [26,27,34] with reports of cognitive decline. A recent communication has shown that a 43-year-old patient developed similar MS-type lesions following RT [35]. In MS, these lesions have been shown to have an immune response that could be indicative of neuroinflammation. The ability to show that these lesions have venules running through them suggests further studies are warranted to test this hypothesis of neuroinflammation as a mediator of late radiation effects. Supporting this finding was the detection of FLAIR hyperintensities coupled with the low R_2^* values that would indicate demyelination. Neuroinflammation as a mediator of radiation late cerebral effects and as a potential therapeutic target is an area of active investigation [29] and these findings suggest imaging biomarkers like SWI and R_2^* might be useful tools for non-invasive monitoring of neuro-inflammatory processes.

This method also corroborates other results that show that the use of multi-echo gradient echo can be of practical importance in the post-treatment monitoring of patients. In addition to SWI and R_2^*, QSM can be used to differentiate between small veins and microbleeds. The halo effect and large susceptibility value of the microbleed on QSM is something that could lead to reduced burden for neuroradiologists when detecting microbleeds through the use of automated methods. Additionally, the high R_2^* can help distinguish microbleeds and small venules that have much lower R_2^* values (20-40 s^{-1}).

A limitation of this study is the limited number of participants and inability to acquire follow-up imaging for all patients. This preliminary experience illustrates the feasibility of the technique in this population and suggests a study of larger cohorts of patients with this imaging technique may be warranted.

Another limitation of SWI techniques, in general, is that titanium clips used following surgery cause blooming artifacts on post-processed images. The artifacts are caused by the magnetic field perturbation caused by these clips and causes the signal to decay at a much higher rate, causing more issues with lengthened TE. Finally, SWI is limited in its ability to view the arterioles; however, Bian et al. [36] have shown that arteries and veins can be imaged in the same acquisition. This method also can decrease false-positives and to improve microbleed detection. This method would also be beneficial in observing damage to the arterioles.

4.5   Conclusions

This chapter presented a preliminary study examining the long-term effects that radiation therapy has on patients treated for benign or low-grade neoplasms. It was demonstrated that these patients are susceptible to microbleeds as well as demyelinating lesions. This study suggests this subset of patients requires further long-term monitoring as they are potentially at an increased risk for vascular and/or cognitive events given the preclinical changes detected and their anticipated longer overall survival. The presence of microbleeds suggests prophylactic treatment with anti-platelet agents or anti-coagulation as a strategy to prevent late vascular events as used in other cerebrovascular diseases may not be advisable. Finally, this study shows that the demyelinating lesions in these patients do have venules that are penetrating through the white matter, as shown in Figures 4.2, 4.3, and 4.4. The finding of venocentricity is similar to other disease processes with a neuroinflammatory component, such as Multiple Sclerosis, supporting current research investigating anti-inflammatory agents as a potential therapeutic strategy to reduce late cerebral effects from radiotherapy.

4.6   References

1.   Lawrence YR, Li XA, el Naqa I, et al. Radiation dose-volume effects in the brain. Int. J. Radiat. Oncol. Biol. Phys. 2010; 76(3): S20–7.

2.   Monje ML, Dietrich J. Cognitive side effects of cancer therapy demonstrate a functional role for adult neurogenesis. Behav. Brain Res. 2012; 227(2): 376–9.

3.   Monje ML. Cranial radiation therapy and damage to hippocampal neurogenesis. Dev. Disabil. Res. Rev. 2008; 14(3): 238–42.

4.   Fink JR, Born D, Chamberlain MC. Radiation necrosis: relevance with respect to treatment of primary and secondary brain tumors. Curr. Neurol. Neurosci. Rep. 2012; 12(3): 276–85.

5.   Rahmathulla G, Marko NF, Weil RJ. Cerebral radiation necrosis: A review of the pathobiology, diagnosis and management considerations. J. Clin. Neurosci. 2013; 20(4): 485–502.

6.   Levin VA, Bidaut L, Hou P, et al. Randomized double-blind placebo-controlled trial of bevacizumab therapy for radiation necrosis of the central nervous system. Int. J. Radiat. Oncol. Biol. Phys. 2011; 79(5): 1487–1495.

7.   Moravan MJ, Olschowka J a., Williams JP, O'Banion MK. Cranial irradiation leads to acute and persistent neuroinflammation with delayed Increases in T-cell infiltration and CD11c expression in C57BL/6 mouse brain. Radiat. Res. 2011; 176(4): 459–473.

8.   Ballesteros-Zebadúa P, Chavarria A, Celis MA, Paz C, Franco-Pérez J. Radiation-induced neuroinflammation and radiation somnolence syndrome. CNS Neurol. Disord. Drug Targets. 2012; 11(7): 937–49.

9.   Lupo JM, Chuang CF, Chang SM, et al. 7-Tesla susceptibility-weighted imaging

to assess the effects of radiotherapy on normal-appearing brain in patients with glioma. Int. J. Radiat. Oncol. Biol. Phys. 2012; 82(3): e493–500.

10. Tanino T, Kanasaki Y, Tahara T, Michimoto K, Kodani K, Kakite S. Radiation induced microbleeds after cranial irradiation: Evaluation by phase-sensitive magnetic resonance imaging with 3.0 Tesla. Yonago Acta Med. 2013; 56(1): 7–12.

11. Charidimou A, Werring DJ. Cerebral microbleeds and cognition in cerebrovascular disease: An update. J. Neurol. Sci. 2012; 322(1-2): 50–5.

12. Cordonnier C. Brain microbleeds. Pract. Neurol. 2010; 10(2): 94–100.

13. Bian W, Hess CP, Chang SM, Nelson SJ, Lupo JM. Susceptibility-weighted MR imaging of radiation therapy-induced cerebral microbleeds in patients with glioma: a comparison between 3T and 7T. Neuroradiology. 2014; 56(2): 91–96.

14. Vernooij MW, Ikram MA, Wielopolski PA, Krestin GP, Breteler MMB, van der Lugt A. Cerebral Microbleeds : Accelerated 3D T2*-weighted GRE MR imaging versus Conventional 2D T2*-weighted GRE MR imaging for detection. Radiology. 2008; 248(1): 272–277.

15. Langkammer C, Khalil M, Enzinger C. Quantitative susceptibility mapping in multiple sclerosis. Radiology. 2013; 267(2): 551–559.

16. Wisnieff C, Ramanan S, Olesik J, Gauthier S, Wang Y, Pitt D. Quantitative susceptibility mapping (QSM) of white matter multiple sclerosis lesions: Interpreting positive susceptibility and the presence of iron. Magn. Reson. Med. 2015; 74(2): 564–570.

17. Reichenbach JR, Barth M, Haacke EM, Klarhöfer M, Kaiser W a, Moser E. High-resolution MR venography at 3.0 Tesla. J. Comput. Assist. Tomogr. 2000; 24(6): 949–957.

18. Lupo JM, Molinaro AM, Essock-burns E, et al. The effects of anti-angiogenic therapy on the formation of radiation-induced microbleeds in normal brain tissue

of patients with glioma. Neuro. Oncol. 2016; 18(1): 87–95.

19. Na A, Haghigi N, Drummond KJ. Cerebral radiation necrosis. Asia. Pac. J. Clin. Oncol. 2013; 10(August 2007): 11–21.

20. Koppelmans V, Vernooij MW, Boogerd W, et al. Prevalence of cerebral small-vessel disease in long-term breast cancer survivors exposed to both adjuvant radiotherapy and chemotherapy. J. Clin. Oncol. 2015; 33(6): 588–593.

21. Liu J, Liu T, Rochefort L De, et al. Morphology enabled dipole inversion for quantitative susceptibility mapping using structural consistency between the magnitude image and the susceptibility map. Neuroimage. 2012; 59(3): 2560–2568.

22. Yablonskiy DA, Sukstanskii AL, Luo J, Wang X. Voxel spread function method for correction of magnetic field inhomogeneity effects in quantitative gradient-echo-based MRI. Magn. Reson. Med. 2013; 70(5): 1283–1292.

23. Jenkinson M, Smith SM. A global optimization method for robust affine registration of brain images. Med. Imaging Anal. 2001; 5143–156.

24. Deasy JO. CERR: a computational environment for radiotherapy research. Med. Phys. 2003; 30(5): 979–985.

25. Ibanez L, W S, Ng L, Cates J. The ITK Software Guide. 2003.

26. Rane N, Quaghebeur G. CNS effects following the treatment of malignancy. Clin. Radiol. 2012; 67(1): 61–68.

27. Szerlip N, Rutter C, Ram N, et al. Factors impacting volumetric white matter changes following whole brain radiation therapy. J. Neurooncol. 2011; 103(1): 111–119.

28. Haller S, Kövari E, Herrmann FR, et al. Do brain T2/FLAIR white matter hyperintensities correspond to myelin loss in normal aging? A radiologic-

neuropathologic correlation study. Acta Neuropathol. Commun. 2013; 114.

29. Greene-Schloesser DM, Moore E, Robbins ME. Molecular pathways: Radiation-induced cognitive impairment. Clin. Cancer Res. 2013; 19(9): 2294–2300.

30. Plummer C, Henderson RD, O'Sullivan JD, Read SJ. Ischemic stroke and transient ischemic attack after head and neck radiotherapy: A review. Stroke. 2011; 42(9): 2410–2418.

31. Martinez-Ramirez S, Greenberg SM, Viswanathan A. Cerebral microbleeds: Overview and implications in cognitive impairment. Alzheimers. Res. Ther. ; 6(3): 33.

32. Haley KE, Greenberg SM, Gurol ME. Cerebral microbleeds and macrobleeds: Should they influence our recommendations for antithrombotic therapies? Curr. Cardiol. Rep. 2013; 15(12): 1–10.

33. Quinn MP, Kremenchutzky M, Menon RS. Venocentric lesions: An MRI marker of MS? Front. Neurol. 2013; 4 JUL(July): 1–5.

34. Armstrong CL, Gyato K, Awadalla AW, Lustig R, Tochner Z a. A critical review of the clinical effects of therapeutic irradiation damage to the brain: The roots of controversy. Neuropsychol. Rev. 2004; 14(1): 65–86.

35. Shaygannejad V, Zare M, Maghzi H, Emami P. Brain radiation and possible presentation of multiple sclerosis. J. Res. Med. Sci. 2013; 18(Suppl 1): S93–5.

36. Bian W, Banerjee S, Kelly DAC, et al. Simultaneous imaging of radiation-induced cerebral microbleeds, arteries and veins, using a multiple gradient echo sequence at 7 Tesla. J. Magn. Reson. Imaging. 2015; 42(2): 269–279.

Chapter 5

5 Apparent Transverse Relaxation (R_2^*) as a method to differentiate treatment effect and progressive disease in pseudoprogression

5.1 Introduction

Pseudoprogression (psPD) is a diagnosis given to patients recently treated for high-grade gliomas with chemotherapy and radiation therapy who exhibit transient post-treatment MRI changes such as worsening gadolinium contrast enhancement within the treated area. While psPD has been reported with radiation alone [1], this finding is most commonly seen in the setting of combined chemotherapy and radiation for glioma. The routine addition of Temozolomide (TMZ) to current treatment regimens for malignant glioma as recommended by Stupp [2,3] and with evidence to support the increased use of chemotherapy in the treatment of lower grade gliomas [4], correctly identifying psPD has become an urgent clinical problem [5]. The reason for the transient enhancement in psPD as seen with MRI has yet to be determined; however, it has been proposed that damage to vascular supply and neuroglial cells caused by alkylating agents such as TMZ cause an exaggerated cellular response to radiation within the tumor. This reaction leads to damaged astrocytes, disrupted vessel supply, inflammation, and subsequently damage to the blood-brain barrier [6]. Supporting this hypothesis is the observation that psPD is more commonly seen in malignant gliomas with the methylated O^6-methylguanine-DNA-methyltransferase enzyme (MGMT), a biomarker of increased sensitivity to treatment [7].

The increased awareness and features associated with psPD prompted revised guidelines for the RECIST [8] and RANO [9] criteria to assist neuroradiologists and oncologists in

interpreting post-treatment enhancing lesions. Regarding psPD, the guidelines recommend that any T_1-weighted gadolinium enhancements within the treatment area be monitored for up to 12 weeks while maintaining adjuvant therapy. If any enhancement appears outside the treated area, a diagnosis of progressive disease (PD) is favored.

Taking a passive approach to the monitoring of possible PD leads to anxiety for the patient and potentially prolongs ineffective treatment with possible clinical deterioration in patients who truly have PD. Alternatively, those with psPD who are incorrectly identified as having PD may be switched from a potentially effective therapy to less effective or more toxic alternatives and could skew the results of salvage clinical trials. [10]. For example, Bevacizumab is a commonly employed salvage therapy for patients for progressive disease and has been shown to reduce enhancement through stabilization of the tumor vasculature; however, Bevacizumab may not only reduce radiation-induced vascular leakiness but may also lessen the efficacy of TMZ in patients who express the MGMT promoter [11]. Thus, patients with actual psPD who are most likely to respond to TMZ could be switched to a potentially deleterious agent if incorrectly identified as PD.

Newer MRI sequences have been used in an attempt to differentiate psPD from PD with varying degrees of success; however, there is still no clear method in which a patient with a gadolinium-enhancing T_1-weighted MRI after therapy can be differentiated between treatment effect and PD.

Of the newer MRI sequences that have become commonplace, Diffusion Weighted Imaging, which can measure the Apparent Diffusion Coefficient (ADC), and perfusion MRI are currently the most applicable within a hospital setting. ADC has the distinct

advantage in that it can be acquired quickly and does not need a T_1-altering exogenous contrast agent. This makes it an attractive option for serial imaging; however, the heterogeneity of the tumors has been cited as a limiting factor in differentiating between psPD and PD using ADC [12].

Perfusion MRI, specifically Dynamic Susceptibility Contrast (DSC) MRI, has become a useful tool to measure Cerebral Blood Volume (CBV) and Cerebral Blood Flow (CBF) amongst other measurements. In single institution studies, increased CBV and CBF have been found to be associated with PD, allowing successful differentiation from psPD [13,14]. DSC is the method of choice due to its speed and ease of acquisition, but may suffer from susceptibility artifacts from air-tissue interfaces, contrast leakage, or high blood volume areas leading to over or underestimating of rCBV [12,15]. It is also difficult to standardize across institutions [16].

Building on the previous literature, the apparent transverse relaxation rate (R_2^*) of patients treated with chemoradiotherapy who exhibited transient post-treatment imaging enhancement where there was clinical uncertainty as to whether changes were related to psPD or PD was examined. R_2^* maps are calculated voxel-by-voxel using a multi-echo gradient echo sequence and fitting the signal decay over echo time. R_2^* measurements have been shown to be highly sensitive to white matter content [17], calcifications, vasculature [18,19], and inflammation [20]. An increased R_2^* is most often attributed to an increased iron content from deoxygenated blood or iron-rich macrophages. A decrease in R_2^* can usually be attributed to calcifications or edema.

It was hypothesized that the differential vascular and inflammatory changes seen in PD vs. psPD would be reflected in different patterns in the R_2^* maps. In particular, it was hypothesized, based on previous perfusion literature [14,21], that PD would be associated with an increase in blood volume and would exhibit an increased R_2^*. Comparatively, psPD would be associated with a decreased blood volume and would exhibit a decrease in R_2^*. Also, it was hypothesized that susceptibility-weighted imaging (SWI) could be helpful in distinguishing areas rich in deoxygenated hemoglobin that would correlate with an increase in R_2^*.

5.2   Methods

5.2.1   Patient Selection

All patient recruitment was approved by and adhered to the University of Western Ontario's Human Subjects Research Ethics Board. All patients had initial surgery with histologic confirmation of malignant glioma. They were treated according to the Stupp protocol with combined TMZ and radiation followed by adjuvant TMZ. Standard of care 1.5T MRI imaging was used to follow patients during treatment with follow-up scans at 1-month post chemoradiation and subsequent scans after every 2-3 cycles of adjuvant chemotherapy. Patients with possible psPD or PD were identified from the neuroradiologist clinical report with correlation with the neuro-oncologist's interpretation of the imaging and clinical findings. Routine clinical imaging in this situation was an early interval scan at 6 weeks after possible psPD was detected. Potentially eligible patients with scans that were ambiguous for psPD vs. PD were offered participation in this study where the additional research scan was obtained within the six-week period before repeat clinical imaging. Patients who exhibited claustrophobia, were under the age

of 18, or whose KPS was less than 60 were excluded from the study. The research scan

was performed between 4 to 21 days following their clinical MRI. Patients were scanned

on a Siemens 3T Prisma MRI Scanner. The patient's clinical status and subsequent

clinical imaging after the research scan was reviewed to determine whether the patient's

imaging changes resolved (consistent with psPD) or worsened (consistent with PD).

5.2.2   Image Acquisition

The following were acquisitions performed for this study: 1) an anatomical T_1-weighted

MPRAGE sequence (FA 8°, TR/TI/TE= 2300 ms/900 ms/2.27 ms, 1 mm isotropic

resolution, scan time 4 minutes), 2) a CSF-attenuated FLAIR sequence (TR/TE

12000 ms/ 139ms, resolution 1 mm x 1 mm x 3.0 mm, scan time 5 minutes), 3) DWI (2D

EPI diffusion-weighted, b=0 s/mm^2 and b=1000 s/mm^2, resolution 0.6 mm x 0.6 mm

x 2.0 mm, scan time 3 minutes) and 4) a 6 echo multi-echo gradient echo sequence (ME-

GRE) (FA=12°, TR/TE/ESP=45 ms/6.41ms/6.12 ms, GRAPPA 2, resolution = 0.5mm x

0.5 mm x 1mm, FOV=22.4cm x 16.8cm x22.4 cm, echo fraction 5/8, scan time 12

minutes, 22 seconds).

5.2.3   Segmentation and Registration

Contrast-enhanced T_1 images and FLAIR images were segmented to form the Contrast-

Enhancing Lesion (CEL) and Non-Enhancing Lesion (NEL), respectively. The CEL was

defined as enhancement on the clinical T_1-weighted gadolinium image and the FLAIR

image while the NEL was defined as hyperintensities on the FLAIR image only. In all

cases, the enhancing lesion on the contrast T_1-weighted image and FLAIR was semi-

automatically segmented using ITK-SNAP [22] for manual and region growing

segmentation and Matlab for further delineations of the CEL and NEL. The Matlab code is included in Appendix A.

Both FLAIR and contrast-enhancing T_1 were registered to the ME-GRE's magnitude echo average image or the computed ADC map. All images were registered using FSL's FLIRT toolbox using normalized mutual information [23]. A contrast-enhancing T_1-weighted image misregistration of 1-mm was considered acceptable due to the contrast-enhancing T_1-weighted image being acquired on a separate day. The frontal and occipital horns, as well as the contralateral sulci, were used as landmarks for registration.

The qualitative gadolinium-enhanced T_1 and FLAIR images, and their subsequent masks, were registered to qualitative datasets to avoid interpolation errors during registration. The necrotic core that was surrounded by the gadolinium enhancement on T_1 was not included in the region of interest as analysis of R_2^* within the necrotic core was noted to be low in both psPD and PD. Therefore, the assessment of R_2^* in this tumor region was felt to be non-informative.

5.2.4   Multi-Echo Image Processing and Computation

From the ME-GRE data, an average magnitude of all echoes (MEA), Susceptibility-Weighted Images (SWI) and R_2^* maps were computed. SWIs were created using in-house software using a frequency based approached initially described by Brainovich et al. [24]. The background phase was removed using an 11 mm Gaussian filter and a linear frequency mask with a 15 Hz cutoff described by Quinn et al. [25] was used to preserve the venous vasculature. The frequency mask was set between 0 and 1 and was multiplied three times into the magnitude image.

R_2^* maps were also computed using an in-house method fitting every voxel's magnitude data to a mono-exponential decay using a nonlinear least squares fit. The data were corrected with a Voxel Spread Function (VSF) as described by Yablonskiy [26].

Mean R_2^* for the CEL and NEL were calculated by computing the average signal intensity of all VSF corrected voxels within each region of interest and fitting the data using a mono-exponential decay curve using a non-linear least squares fit as described above. In most cases the data at each echo were normally distributed; however, in one case the later echoes had a binomial distribution (Patient 4), this case was documented and investigated further as described in the discussion and Figure 5.2.

5.2.5 R_2^* Comparisons

Comparisons of R_2^* between the CEL and the NEL, as well as the ratio of R_2^* in the CEL to NEL, were made to determine whether differences in R_2^* within these regions could provide insight into the disease pathology. The hypothesis was that the presence of greater blood volume, a greater hypoxic region, and leakier vessels in PD would increase the R_2^* in the CEL of PD patients. Conversely, lower vascular load within psPD would lower the R_2^* within the CEL.

5.2.6 ADC Computations

ADC maps were processed online using the Siemens Prisma software. The same CEL and NEL regions of interest were registered to and applied to the ADC maps. ADC histograms were analyzed and reported as the mean and median values, unless otherwise stated. Some patient's ADC histograms had a binomial distribution and are documented in Table 5.1.

5.3　　Results

5.3.1　Lesion R_2^*

Nine of eighteen patients imaged had useable multi-echo gradient studies. Reasons for non-useable data included motion artifact (n=8) or magnetic susceptibility caused by the surgical clips at the site of the craniotomy (n=1). In this specific instance, the titanium clip interfered with the contrast-enhancing lesion leading to artificially increased R_2^*.

Of the nine patients who were analyzed in this study, four patients had continued progression on subsequent imaging indicative of PD. Additionally, four patients had a psPD at the site as indicated by improvement of subsequent imaging with one of these four subsequently developing imaging changes that were suggestive of progressive disease after the initial improvement. Finally, one patient had a mixed response with imaging changes being characterized as both psPD and PD (later confirmed histologically).

As shown in Table 5.1, patients who were subsequently diagnosed with PD had an increased R_2^* within the CEL compared to the NEL with a R_2^* ratio of CEL/NEL > 1.3. For patients who were diagnosed with PD, a cluster of increased R_2^* can be seen, as illustrated in Figures 5.1 and 5.2.

Table 5.1 Reported R_2^* and ADC values with clinical outcome of patients

Patient	R_2^* CEL (s⁻¹)	R_2^* NEL (s⁻¹)	Mean R_2^* CEL/NEL ratio	ADC CEL Mean/Median (x 10⁻⁶mm²/s)	ADC NEL Mean/Median (x 10⁻⁶mm²/s)	Outcome
1	10.3-11.0	10.3-11.0	1.0	1358/1398	1315/1362	psPD at site, metastasis elsewhere
2	14.1-14.6	11.1-11.7	1.3	1373/1340	1461/1457	PD
3[a]	9.7-11.4	9.4-11.3	1.0	1456/1449	1475/1524	psPD
4	10.2-11.0	10.5-11.5	1.0	1172/1153[b]	1274/1295[b]	psPD at site, clinical deterioration with reduction of steroids
5	17.9-18.8	12.9-14.1	1.4	1132/1077	1009/1025	PD
6	16.1-17.2	11.8-13	1.3	1101/1092	1353/1301	PD
7	19.1-21.4	13.9-15.1	1.4	1182/1058[b]	1332/1281[b]	PD
8	18.2-21.0 [c]	10.3-11.3 [c]	1.8	1328/1240b	1247/1206[b]	Residual tumor at margins and necrosis
9	12-13.2 [c]	11.4.-12.7[c]	1.0	1335/1329	1314/1329	psPD followed by progression

[a]: ME-GRE sequence was fit over only 4 echoes due to severe motion artifact at echoes 5 and 6.

[b]: ADC histogram had a binomial distribution indicative of PD and psPD.

[c]: Later ME-GRE echoes had binomial distribution of data, this could be due to a mixture of PD and psPD tissue within the lesion.
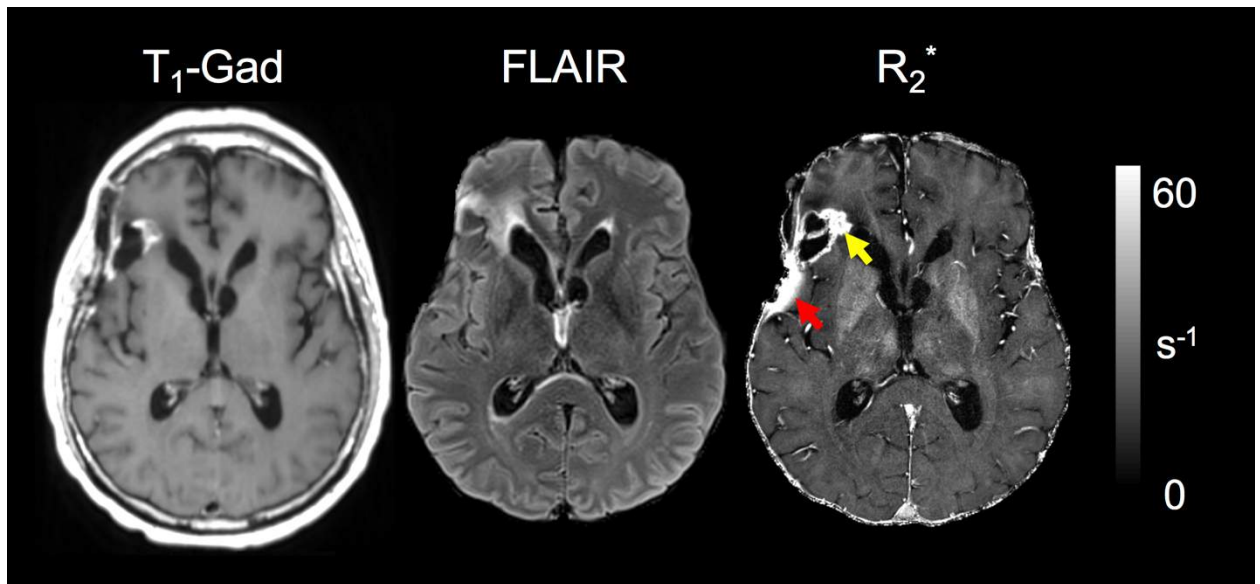
Figure 5.1 Patient 7 shows gadolinium enhancement on T_1 (A) and FLAIR enhancement (B) in the posterior right frontal lobe near the right frontal horn. Corresponding R_2^* maps (C) shows increased R_2^* near the right frontal horn indicative of tumorous tissue. Red arrow shows artefact from titanium clip, where yellow arrow shows PD.
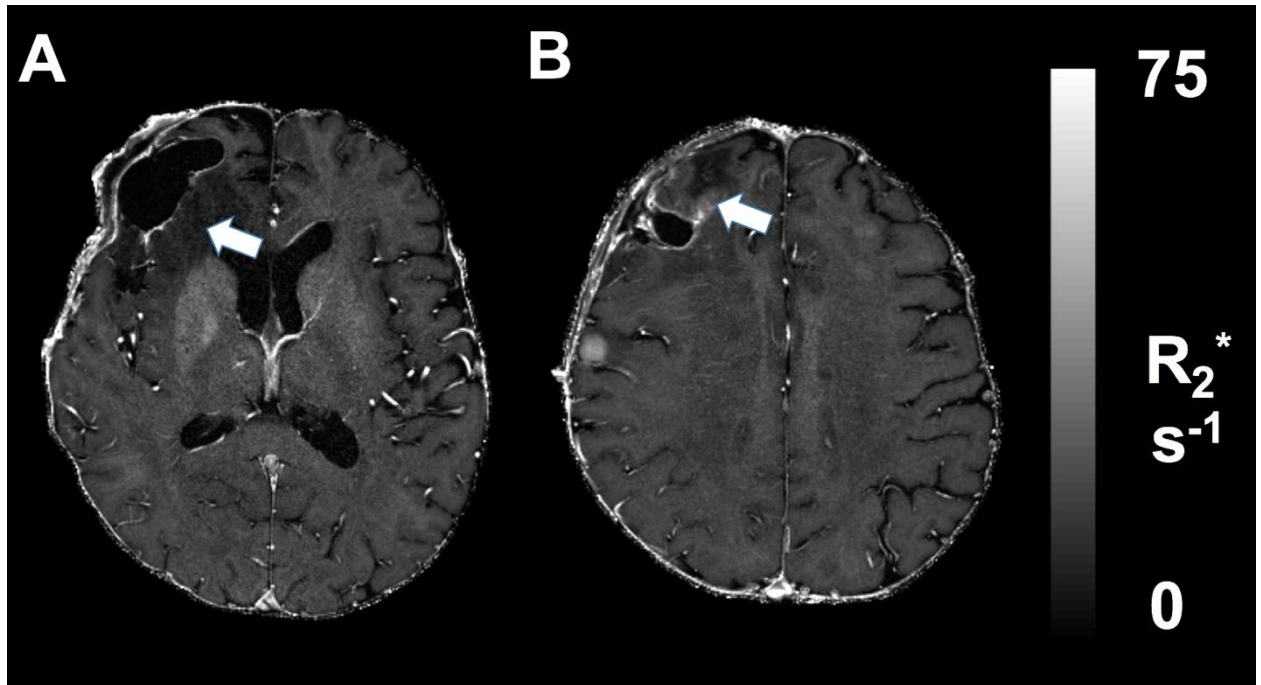
Figure 5.2 Patient 8 shows both suspected necrotic lesions (psPD) (A) and tumorous tissue (PD) (B) in separate slices. Both areas are indicated by the white arrow in the respective panel.

Patients who were subsequently diagnosed with psPD had a similar R_2^* within the CEL and NEL with a ratio of CEL/NEL =1. As well, a slightly lower R_2^* in the NEL of psPD patients compared to the NEL of PD patients was observed.

A rim with an increased R_2^* surrounding the necrotic lesion in all patients who were subsequently diagnosed with psPD is also observed. The increase in R_2^* is associated with a decrease in FLAIR intensity and decrease signal on the SWI average as shown in Figure 5.3.
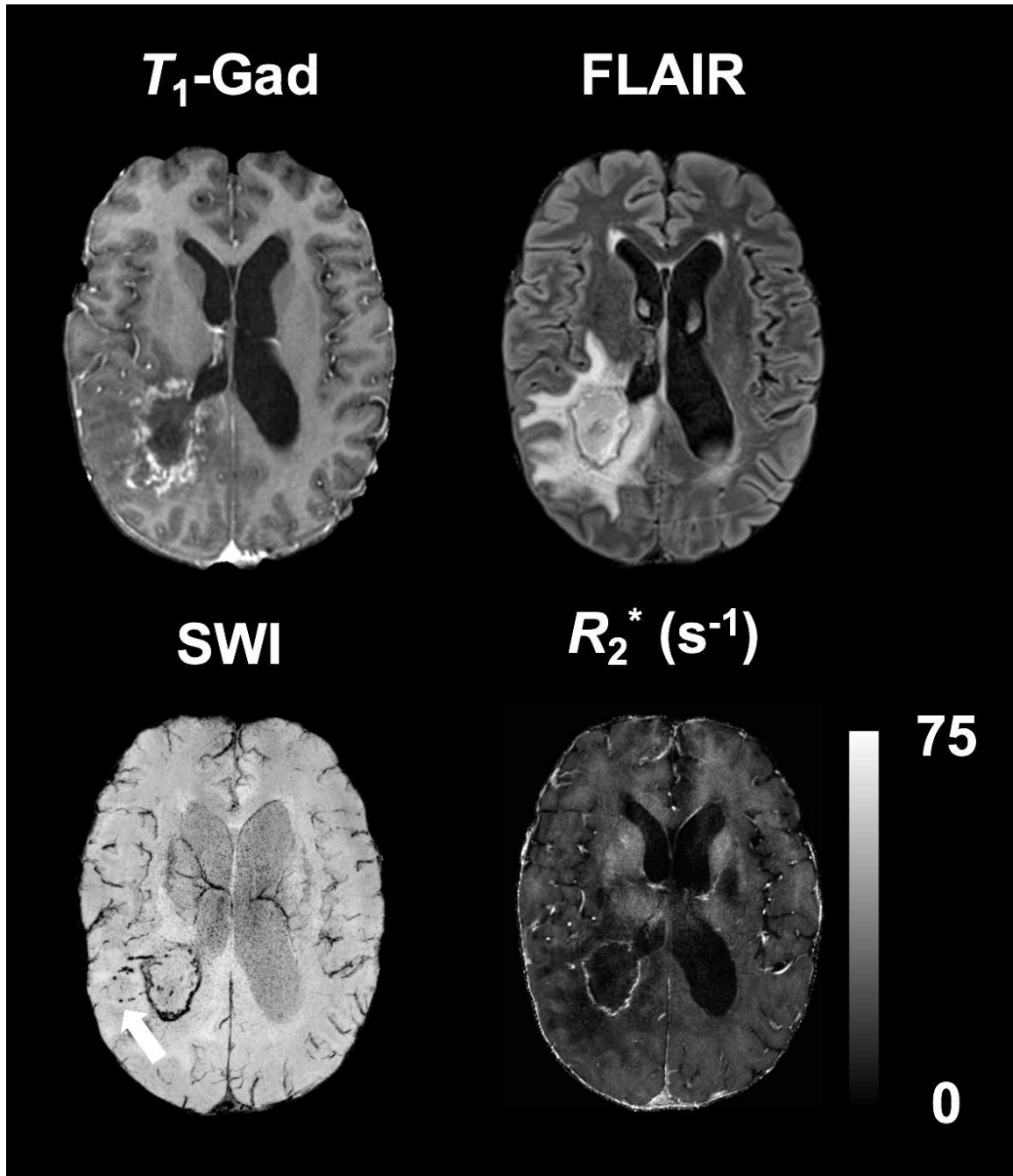
Figure 5.3 Patient 4 developed progression at a the frontal horn (not shown). An example of the rim with increased R_2^* is shown. This is most likely a hypoxic zone as the area appears to be rich in deoxygenated blood shown on the SWI. The SWI also show microbleeds indicated by the white arrow

5.3.2   ADC Values

A comparison of mean ADC values with a cutoff of 1200 x 10^{-6} mm^2/s as suggested in

the literature [27] was performed. A mean ADC below 1200 x 10^{-6} mm^2/s was shown to

indicative of PD and above 1200 x 10^{-6} mm^2/s was shown to be indicative of psPD in the

referenced study. In most cases this mean cutoff agreed with the diagnosis; however, in

two of the cases, the mean ADC values did not agree with clinical outcome. Further

examination of the mean and median, as well as the clinical outcome, shows a mixed

outcome (both PD and psPD) for patient 8. Patient's 2 mean and median ADC are both

above the cut-off that would be indicative of PD.

5.4   Discussion

A method in which quantitative R_2^* maps are used to differentiate PD from psPD is

presented. The findings suggest that increases of R_2^* in the CEL as shown by absolute

measurements and ratios of R_2^* in the CEL compared to the NEL may stratify patients

with PD, psPD, or mixed PD and PsPD. In particular, patients whose R_2^* ratio of CEL to

NEL was closer to 1 had a diagnosis of psPD upon further clinical follow-up. Those

patients with a mean R_2^* that was between 3-6 s^{-1} higher in the CEL compared to the

NEL, and a R_2^* ratio between the CEL and NEL >1.3, subsequently exhibited

radiographic worsening and clinical signs of PD. This is shown in Figure 5.1, where

Patient 7's R_2^* is remarkably increased and subsequent imaging revealed progressive

disease.

The increase in R_2^* is most likely due to an increase in deoxygenated blood due to the

leakiness of the blood vessels within the tumorous tissue. It should also be noted that

intrapatient differences of R_2^* between the CEL and NEL have the distinct advantage of the possibility of multi-center implementation as the patient's NEL could serve as their own control metric. This would reduce variables such as scanner type dependence or difference in magnetic field shimming that could confound the use of an absolute R_2^* as a metric. Potential disadvantages are the sensitivity to motion artifact and tissue inhomogeneities, though these can be addressed with faster R_2^* mapping sequences.

The R_2^* maps provided valuable insight into the potential disease pathology. For example, Patient 8 showed deterioration five months after her initial psPD diagnosis and had to be re-operated. Upon surgery, she was diagnosed with radiation-induced tissue necrosis with infiltrating tumor at the margins of the necrotic region. The initial R_2^* within the CEL was remarkably higher than the NEL, indicating probably tumor; however, the 95% confidence of the R_2^* had a variation of 3 Hz, showing the possibility of a mixture of voxels within the area of interest. As shown in Figure 5.2, most of the treated site is surrounded by a rim of high R_2^*; however, there are clusters of high R_2^* voxels around the treatment site hypothesized to be residual tumor. Thus the R_2^* imaging findings are consistent with the later histologic picture of a mixed treatment and tumor progression effect.

A similar clinical outcome occurred for Patient 9. While initially there was no signs of PD, he deteriorated 3 to 4 months following his research scan visit with a follow-up clinical scan indicative of stable disease. The R_2^* ratio between the CEL and NEL is approximately 1; however, examination of the R_2^* map shows mild increases near the left frontal horn which is within the initial treatment site as shown in Figure 5.4. While it was not possible to obtain R_2^* measurements following his subsequent clinical visit, this case

illustrates that serial monitoring of R_2^* may be useful as some patients may exhibit mixed
pictures of psPD/PD and evolution of PD after psPD.
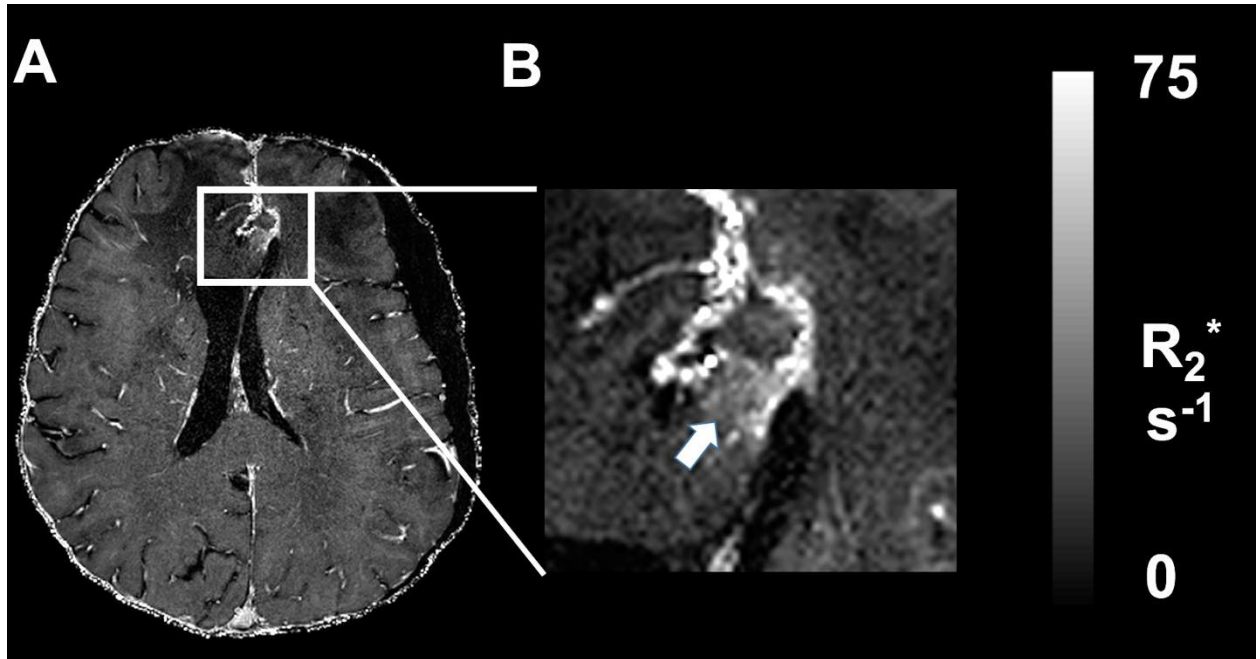
Figure 5.4 Patient 9, initially diagnosed with psPD but presented with PD at a later time point. The R_2^* map (A) corroborates psPD diagnosis; however, zoomed near the left frontal horn, area of slight R_2^* increase is evident, potentially indicative of PD.

There is a rim of increased R_2^* no greater than 1-1.5 mm (2-3 voxels) thick at the
interface between the necrotic core and enhancing rim of tumor in all patients. Upon
closer examination of the SWI and FLAIR, a hypointensity in this rim can be observed in
both methodologies as shown in Figure 5.3. References relating to the increased R_2^* in the
rim in previous literature was not found, and this unique finding requires evaluation in
larger cohorts of patients. Given the fact that changes in blood flow and volume between
PD and psPD has been noted using MR perfusion techniques, it is possible that the R_2^*

rim may also be influenced by changes in blood flow. Whether the R_2^* rim noted could be used as a surrogate marker for perfusion changes remains to be investigated.

In passing, it was noted that microbleeds (shown in Figure 5.3) appear around the treated site for all patients, corroborating other findings in published literature [28–30]. There was no difference in the distribution of microbleeds within this cohort suggesting this might not be a useful imaging biomarker for distinguishing PD from psPD. While the quantitative measures of R_2^* provide us with valuable insight regarding the primary disease, microbleed detection is best accomplished using mIP SWI maps. Whether better assessment of microbleeds by mIP SWI maps would be a useful biomarker for psPD vs. PD requires further investigation.

Absolute ADC values have been proposed as an effective means of distinguishing PD versus psPD. In this series, in 7/9 patients mean ADC was able to predict PD from psPD using a cutoff of 1200 x 10^{-6} mm^2/s as recommended by a Lee et al. [31]. In Patient 4, the proposed ADC cutoff incorrectly identified the patient as psPD while the R_2^* measurements correctly identified them as PD suggesting R_2^* and ADC may provide complementary information. Given that both ADC and R_2^* can be acquired without contrast, combined ADC and R_2^* maps may be worth exploring as an alternative imaging biomarker for psPD compared to contrast-enhanced perfusion MRI which is preferred in the clinic due to shorter imaging time and higher signal [12].

This study offers promise and warrants further investigation; however, some limitations were observed throughout this study that should be refined in future research. Firstly, patient motion artifacts were a severely limiting factor for this study. Patients were put

into the head cradle with sufficient padding to reduce head movement; however, the sub-millimeter in-plane resolution acquired for the ME-GRE sequence was not robust against motion. Additionally, the long scan time of the sequence (12 minutes) was not well tolerated by many patients. A lower-resolution scan could be sufficient for clinical application. A typical clinical scan's duration ranges from 4-6 minutes, and a resolution of 0.8mm in-plane by 1.5 mm thick axial slices would be easily achievable in this time range. In addition to a faster sequence, there would be an increase in SNR which could accelerate the sequence further. The use of enhanced patient immobilization devices could also be considered to reduce patient motion but may be less practical than optimizing the sequence parameters. Another opportunity for optimization would be integrating the R_2^* imaging into the routine clinical imaging. This would reduce errors related to registering different scans acquired on different days and in different positions. This was seen in this study in one patient where technical difficulties in registering the clinical and study scans precluded analysis.

Finally, this technique is also prone to susceptibility artifacts. Figure 5.1 (c) has an excellent example of the titanium clip artifact posterior to the lesion. Also, artifacts caused by air-tissue interfaces such as the sinuses or ear canals could hamper this technique.

5.5   Conclusions

This research demonstrates a feasibility study in which PD can be differentiated from treatment effect using R_2^*. Patients whose R_2^* was increased within the CEL lesion compared to the NEL were diagnosed as true progressive disease, while patients whose R_2^* had similar values between the CEL and NEL were diagnosed as having treatment

effect. This method also shows promise to be adapted to multi-center trials as patients could potentially serve as their own control metric using the NEL. Opportunities exist to optimize the R_2^* acquisition and integrate into clinical scanning protocols to facilitate adoption and use in larger cohorts and across institutions.

5.6   References

1.   Hallock A, Bauman G. Transient radiographic early enhancement after radiotherapy for meningioma. Can. J. Neurol. Sci. 2012; 39(1): 99–101.

2.   Stupp R, Hegi ME, Mason WP, et al. Effects of radiotherapy with concomitant and adjuvant temozolomide versus radiotherapy alone on survival in glioblastoma in a randomised phase III study: 5-year analysis of the EORTC-NCIC trial. Lancet Oncol. 2009; 10(5): 459–466.

3.   Stupp R, Mason WP, Van Den Bent MJ, et al. Radiotherapy plus concomitant and adjuvant temozolomide for glioblastoma. N. Engl. J. Med. 2005; 352(10): 987–996.

4.   Buckner JC, Shaw EG, Pugh SL, et al. Radiation plus Procarbazine, CCNU, and Vincristine in low-grade glioma. N. Engl. J. Med. 2016; 374(14): 1344–1355.

5.   Taal W, Brandsma D, De Bruin HG, et al. Incidence of early pseudo-progression in a cohort of malignant glioma patients treated with chemoirradiation with temozolomide. Cancer. 2008; 113(2): 405–410.

6.   Tran DKT, Jensen RL. Treatment-related brain tumor imaging changes: So-called "pseudoprogression" vs. tumor progression: Review and future research opportunities. Surg. Neurol. Int. 2013; 4(S3): S129–S135.

7.   Knudsen-Baas KM, Moen G, Fluge O, Storstein A. Pseudoprogression in high-grade glioma. Acta Neurol. Scand. 2013; 127(S196): 31–37.

8.   Eisenhauer E, Therasse P, Bogaerts J, et al. New response evaluation criteria in

solid tumours: Revised RECIST guideline (version 1.1). Eur. J. Cancer. 2009; 45(2): 228–247.

9.   Wen PY, Macdonald DR, Reardon DA, et al. Updated response assessment criteria for high-grade gliomas: response assessment in neuro-oncology working group. J. Clin. Oncol. 2010; 28(11): 1963–1972.

10.   Stuplich M, Hadizadeh DR, Kuchlmeister K, Scorzin J, Filss C, Langen K-J. Late and prolonged pseudoprogression in glioblastoma after treatment with Lomustine and Temozolomide. J. Clin. Oncol. 2013; 30(21): 129–132.

11.   Thompson EM, Frenkel EP, Neuwelt EA. The paradoxical effect of bevacizumab in the therapy of malignant gliomas. Neurology. 2011; 76(1): 87–93.

12.   Huang RY, Neagu MR, Reardon DA, Wen PY. Pitfalls in the neuroimaging of glioblastoma in the era of antiangiogenic and immuno/targeted therapy - detecting illusive disease, defining response. Front. Neurol. 2015; 6(33): 1–16.

13.   Young RJ, Gupta A, Shah AD, et al. MRI perfusion in determining pseudoprogression in patients with glioblastoma. Clin. Imaging. 2013; 37(1): 41–49.

14.   Prager AJ, Martinez N, Beal K, Omuro AM, Zhang Z, Young RJ. Diffusion and perfusion MRI to differentiate treatment-related changes including pseudoprogression from recurrent tumors in high-grade gliomas with histopathologic evidence. Am. J. Neuroradiol. 2015; 36(5): 877–885.

15.   Paulson ES, Schmainda KM. Comparison of dynamic susceptibility-weighted contrast-enhanced MR methods: recommendations for measuring relative cerebral blood volume in brain tumors. Radiology. 2008; 249(2): 601–613.

16.   Shiroishi MS, Boxerman JL, Pope WB. Physiologic MRI for assessment of response to therapy and prognosis in glioblastoma. Neuro. Oncol. 2016; 18(4): 467–478.

17. Deistung A, Schäfer A, Schweser F, Biedermann U, Turner R, Reichenbach JR. Toward in vivo histology: a comparison of quantitative susceptibility mapping (QSM) with magnitude-, phase-, and R2*-imaging at ultra-high magnetic field strength. Neuroimage. 2013; 65(de): 299–314.

18. Langkammer C, Schweser F, Krebs N, et al. Quantitative susceptibility mapping (QSM) as a means to measure brain iron? A post mortem validation study. Neuroimage. 2012; 62(3): 1593–1599.

19. Chen W, Zhu W, Kovanlikaya I, et al. Intracranial calcifications and hemorrhages: characterization with quantitative susceptibility mapping. Radiology. 2014; 270(2): 496–505.

20. Wisnieff C, Ramanan S, Olesik J, Gauthier S, Wang Y, Pitt D. Quantitative susceptibility mapping (QSM) of white matter multiple sclerosis lesions: Interpreting positive susceptibility and the presence of iron. Magn. Reson. Med. 2015; 74(2): 564–570.

21. Nasseri M, Gahramanov S, Netto JP, et al. Evaluation of pseudoprogression in patients with glioblastoma multiforme using dynamic magnetic resonance imaging with ferumoxytol calls RANO criteria into question. Neuro. Oncol. 2014; 16(8): 1146–1154.

22. Ibanez L, W S, Ng L, Cates J. The ITK Software Guide. 2003.

23. Reuter M, Rosas HD, Fischl B. Highly accurate inverse consistent registration: a robust approach. Neuroimage. 2010; 53(4): 1181–1196.

24. Brainovich V, Sabatini U, Hagberg GE. Advantages of using multiple-echo image combination and asymmetric triangular phase masking in magnetic resonance venography at 3 T. Magn. Reson. Imaging. 2009; 27(1): 23–37.

25. Quinn MP, Gati JS, Klassen LM, et al. Comparison of multiecho postprocessing schemes for SWI with use of linear and nonlinear mask functions. Am. J. Neuroradiol. 2014; 35(1): 38–44.

26. Yablonskiy DA, Sukstanskii AL, Luo J, Wang X. Voxel spread function method for correction of magnetic field inhomogeneity effects in quantitative gradient-echo-based MRI. Magn. Reson. Med. 2013; 70(5): 1283–1292.

27. Linn J. Neuroimaging of therapy-associated brain tissue abnormalities. Curr. Opin. Neurol. 2014; 27.

28. Bian W, Hess CP, Chang SM, Nelson SJ, Lupo JM. Susceptibility-weighted MR imaging of radiation therapy-induced cerebral microbleeds in patients with glioma: a comparison between 3T and 7T. Neuroradiology. 2014; 56(2): 91–96.

29. Tanino T, Kanasaki Y, Tahara T, Michimoto K, Kodani K, Kakite S. Radiation induced microbleeds after cranial irradiation: Evaluation by phase-sensitive magnetic resonance imaging with 3.0 Tesla. Yonago Acta Med. 2013; 56(1): 7–12.

30. Shen Q, Lin F, Rong X, et al. Temporal cerebral microbleeds are associated with radiation necrosis and cognitive dysfunction in patients treated for nasopharyngeal carcinoma. Int. J. Radiat. Oncol. Biol. Phys. 2016; 94(5): 1113–1120.

31. Lee WJ, Choi SH, Park C-K, et al. Diffusion-weighted MR imaging for the differentiation of true progression from pseudoprogression following concomitant radiotherapy with temozolomide in patients with newly diagnosed high-grade gliomas. Acad. Radiol. 2012; 19(11): 1353–1361.

Chapter 6

6   Conclusions and Future Work

This thesis sought to determine the feasibility of implementing a multi-echo gradient

echo sequence and its post processing techniques within the pre-clinical and clinical

environment to detect for radiation necrosis and pseudoprogression. The post-processed

images used in this thesis were SWI, R_2^* and QSM. The results of this thesis in both an

animal model and human patients show promise for integration within a clinical

environment. This chapter seeks to summarize the content of this thesis and discuss

relevant future work necessary for its implementation in clinical trials or within the clinic

for the long term implication of radiation to the central nervous system (Chapters 3 and

4) and patients treated with chemoradiotherapy who present with post-treatment

radiographical worsening following treatment (Chapter 5).

6.1   Context of Findings

While MRI has become an essential tool within the clinic in the diagnosis and follow-up

imaging of patients, traditional techniques are still preferred due to their proven success

and familiarity. In recent years, the increased availability of MRIs and breakthroughs in

technological advancements has rapidly made newer techniques available to attempt to

address urgent clinical problems; however, many of these techniques require longer

acquisition times or are more technically challenging, making integration within a clinical

setting difficult. As such, this thesis sought to use a widely available sequence and post-

processed images in attempts to solve clinical needs.

Chapter 3 addressed the ability of R_2^* to predict areas of radiation necrosis retrospectively

in a rat brain. A major challenge in the clinic is the capacity to differentiate necrosis from

tumorous tissue using traditional T_1-enhancing image and T_2-weighted images [1]. While the fundamental molecular mechanisms are different in both pathologies, both exhibit similar imaging changes. The use of ADC and perfusion techniques have been shown to aid in differentiation of pathologies [2,3], yet once tissue necrosis is established, the tissue is no longer salvageable and may need to be debulked should patients exhibit neurological symptoms.

The fundamental mechanisms that lead to RN have been researched extensively over the years as contributions from vasculature ischemia, glial cell death, and neuroinflammation [4,5]. Increases of R_2^* within this chapter remained non-specific as markers of histology beyond H&E and LFB were not performed. The ability to predict changes in both the hippocampus and internal/external capsule warrants further study as there exists a potential of harnessing a missing link between in-vivo imaging and histology and immunohistochemistry.

Chapter 4 addressed the usefulness of SWI, R_2^* and QSM as a technique that could be used for long-term monitoring of patients who have undergone radiotherapy for benign or low-grade neoplasms. This is the first study to show microbleeds within the high dose region of radiotherapy with radiation alone. The long-term clinical impact of these microbleeds remain to be established; however, as discussed in chapter 4 there is the potential for increased risk of vascular abnormalities (e.g. stroke). In addition to this finding, hyperintense lesions on FLAIR appear to be venocentric on SWI, R_2^* and QSM. This common finding in MS is indicative of a neuroinflammatory process [6]. This study reinforces the need for long-term monitoring of these patients since their longer expected

OS may yield a predisposition for neurovascular disease as well as long-term necrosis, neurological symptoms or cognitive deficits.

Finally, the findings in Chapter 5 indicate that R_2^* and SWI could serve as a marker to differentiate between pseudoprogression and true progression. This technique was effective in retrospectively determining pseudoprogression from true progression. Additionally, this technique was demonstrated to have increased R_2^* within a contrast enhancing lesion in patients with progression as well as an increase of R_2^* between the contrast and non-contrast enhancing lesion. A large-scale study is needed to establish the sensitivity and specificity of this technique with correlations to PFS and OS.

6.2   Future Work

6.2.1   Future Experiments

As was previously discussed, Chapter 3 provides a solid foundation for further research to establish R_2^* as a predictor of radiation necrosis. The two most immediate refinements that need to be addressed are correlations with histopathological findings and comparison to a tumor model. Previous studies have shown radiation to the CNS increases the immunoreactivity of glial fibrillary acidic protein, a marker of astrocyte activation, as early as hours following radiation and as late as six months in mice [7,8]. In addition to this marker, increases in tumor necrosis factor alpha and intercellular adhesion molecule one were also shown.

A comprehensive histological in a C57BL/6 mouse study showed that markers such as MHC II expression, CD3, and CD11c are evident as early as 30 days following radiation with up to 35 Gy [9]. While one can speculate that these markers are the underlying source of inflammation and therefore increases R_2^*, actual correlations would add value to this

technique.

Additionally, comparison to the tumor model would determine whether R_2^* is a method

that can differentiate radiation necrosis tumor progression. The increased vasculature in

tumors may prove to be a confounding factor in the interpretation of R_2^*.

In Chapter 4, the main unaddressed questions are the relevance of the microbleeds within

the high dose region as well as the finding that the white matter lesions appear to be

venocentric. Venocentric lesions are common in MS and may be ground zero for the

immune response. While microbleeds appear within the high dose region in this specific

cohort of patients, a study with age-matched controls could shed further light onto the

significance of these microbleeds. Also, as was noted in the study, some of these

microbleeds appear to resolve at the one-year follow-up. The significance of this finding

demonstrates that the vascular system may still be re-adapting itself years after therapy.

The feasibility and large cohort necessary for such a long-term study limit the possibility

of pursuing this over a Ph.D. degree.

The method presented in Chapter 5 is promising; however, a larger cohort spanning many

centers is needed to address the issue of sensitivity and specificity of this technique.

Further to this specific issue, correlations with the methylation of the MGMT promoter

could add value to this technique. Methylation of the MGMT promoter has previously

been shown to correlate with pseudoprogression [10]. Finding an imaging correlate of

MGMT expression would be useful as second-line salvage therapy such as Bevacizumab

is unadvised in such a patient cohort [11]. Further refinements to the acquisition techniques

must be performed to make the acquisition tolerable for these patients. Patients may need

to be placed in a more confined restraint system to limit motion or techniques to increase

the speed of the acquisition must be taken. Increasing the voxel size may lead to a faster acquisition; however, the appropriate voxel size should be established to optimize imaging time with the loss of resolution (e.g. imaging small veins, microbleeds, etc.). Other methods for a fast acquisition could include using multiband techniques to accelerate further, using a higher GRAPPA factor. Different techniques for acquisition such as Wave-CAIPI [12] or more common methods such as EPI could be used to acquire images faster

6.2.2   In Closing

While there exists motivation for future work in each of the chapters, an overarching problem with the implantation of the multi-echo gradient echo and its post-processing techniques is the lack of standardization across multiple sites. This issue has already been demonstrated in other techniques such as DWI and perfusion by having vendor dependence (both scanner and software) as well as implementation dependence (use of 2 or 3 diffusion gradients) [13,14].

A consensus on the post-processing methods of multi-echo gradient echo sequences also needs to be established. Specifically, the filtering of phase (e.g. what are considered local and background contributors to phase) for processing of SWI, as well as the methods in which QSM is calculated to avoid artifacts from the ill-defined problem, is needed. The way in which R_2^* is calculated needs to be addressed as different methods for post-processing exist, all adding complexity to the computation. Commercial vendors such as Siemens provide a quick method to calculate R_2^*, yet as shown in Figure 6.1, there are differences compared to a robust and computationally expensive technique such as non-linear least squares optimization with background field correction for intra-voxel

dephasing [15]. Areas of high susceptibility and low signal appear prone to errors in calculation while differences of R_2^* in the veins are also apparent.
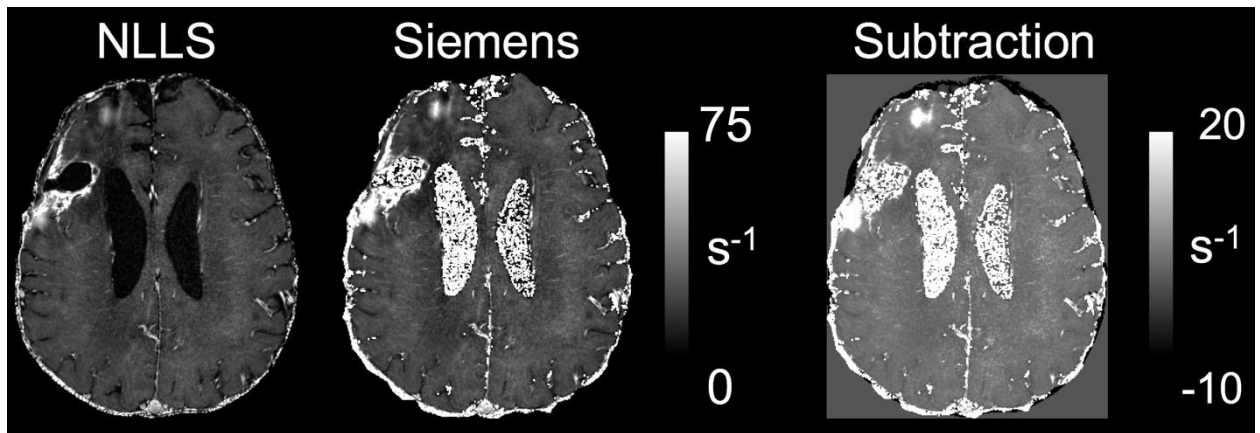

Figure 6.1 Example of R_2^* calculated using the method in this thesis (NLLS), calculation from SIEMENS, and a subtraction of the two.

In conclusion, this thesis presents new methods in which the response of the central nervous system to radiation therapy is investigated. This non-contrast technique makes this sequence easily implementable in routine clinical imaging and could serve as a tool to assist neuroradiologists and neuro-oncologists to assess properly patients treated with radiotherapy.

6.3   References

1.   Mullins ME, Barest GD, Schaefer PW, Hochberg FH, Gonzalez RG, Lev MH. Radiation necrosis versus glioma recurrence: Conventional MR imaging clues to diagnosis. Am. J. Neuroradiol. 2005; 26(8): 1967–1972.

2.   Hein P a, Eskey CJ, Dunn JF, Hug EB. Diffusion-weighted imaging in the follow-up of treated high-grade gliomas: tumor recurrence versus radiation injury. Am. J. Neuroradiol. 2004; 25(2): 201–9.

3.   Wang S, Tryggestad E, Zhou T, et al. Assessment of MRI parameters as imaging biomarkers for radiation necrosis in the rat brain. Int. J. Radiat. Oncol. Biol. Phys.

2012; 83(3): e431–6.

4. Fink JR, Born D, Chamberlain MC. Radiation necrosis: relevance with respect to treatment of primary and secondary brain tumors. Curr. Neurol. Neurosci. Rep. 2012; 12(3): 276–85.

5. Tofilon PJ, Fike JR. The radioresponse of the central nervous system: a dynamic process. Radiat. Res. 2000; 153(4): 357–70.

6. Quinn MP, Kremenchutzky M, Menon RS. Venocentric lesions: An MRI marker of MS? Front. Neurol. 2013; 4 JUL(July): 1–5.

7. Chiang CS, McBride WH, Withers HR. Radiation-induced astrocytic and microglial responses in mouse brain. Radiother. Oncol. 1993; 29(1): 60–8.

8. Kyrkanides S, Olschowka JA, Williams JP, Hansen JT, O'Banion MK. TNF alpha and IL-1beta mediate intercellular adhesion molecule-1 induction via microglia-astrocyte interaction in CNS radiation injury. J. Neuroimmunol. 1999; 95(1-2): 95–106.

9. Moravan MJ, Olschowka J a., Williams JP, O'Banion MK. Cranial irradiation leads to acute and persistent neuroinflammation with delayed Increases in T-cell infiltration and CD11c expression in C57BL/6 mouse brain. Radiat. Res. 2011; 176(4): 459–473.

10. Brandes AA, Franceschi E, Tosoni A, et al. MGMT promoter methylation status can predict the incidence and outcome of pseudoprogression after concomitant radiochemotherapy in newly diagnosed glioblastoma patients. J. Clin. Oncol. 2008; 26(13): 2192–2197.

11. Thompson EM, Frenkel EP, Neuwelt EA. The paradoxical effect of bevacizumab in the therapy of malignant gliomas. Neurology. 2011; 76(1): 87–93.

12. Bilgic B, Gagoski BA, Cauley SF, et al. Wave-CAIPI for highly accelerated 3D imaging. Magn. Reson. Med. 2015; 73(6): 2152–62.

13. Boxerman JL, Ellingson BM. Response Assessment and Magnetic Resonance Imaging Issues for Clinical Trials Involving High-Grade Gliomas. Top. Magn. Reson. Imaging. 2015; 24(3): 127–136.

14. Shiroishi MS, Boxerman JL, Pope WB. Physiologic MRI for assessment of response to therapy and prognosis in glioblastoma. Neuro. Oncol. 2016; 18(4): 467–478.

15. Yablonskiy DA, Sukstanskii AL, Luo J, Wang X. Voxel spread function method for correction of magnetic field inhomogeneity effects in quantitative gradient-echo-based MRI. Magn. Reson. Med. 2013; 70(5): 1283–1292.

Appendix A

Matlab code used to identify CEL and NEL in chapter 5:

```
Clear all; close all;

GADroi_nii=load_untouch_nii('GAD_on_MEA_brain_Seg.nii.gz');

FLAIRroi_nii=load_untouch_nii('FLAIR_on_MEA_brain_Seg.nii.gz');

GADroi= GADmask_nii.img;

FLAIRroi= FLAIRmask_nii.img;
GADroi (FLAIRroi ==0)=0;
FLAIRroi(GadROI==1)=0;

GADroi_nii.img=GADroi

FLAIRroi_nii.img=FLAIRroi

Save_untouch_nii(GADroi_nii,'actual_GAD_ROI_.nii')

Save_untouch_nii(FLAIRroi_nii,'actual_FLAIR_ROI_.nii')
```

Curriculum Vitae

Name: Jean-Guy Belliveau

Post-secondary Education and Degrees: University of British Columbia
Vancouver, British Columbia, Canada
2005-2009 B.A.Sc.

The University of Western Ontario
London, Ontario, Canada
2009-2011 M.E.Sc.

The University of Western Ontario
London, Ontario, Canada
2011-2016 Ph.D.

Honours and Awards: Schmeelk Foundation Fellowship
2015-2016

Ontario Graduate Scholarship in Science and Technology
2013-2014

London Regional Cancer Program Catalyst Grant
2012

Related Work Experience   Teaching Assistant
The University of Western Ontario
2010, 2014, 2015

Linear Accelerator Quality Assurance
London Regional Cancer Program
2013, 2015

Publications:

J-G Belliveau, KM Gilbert, M Abou-Khousa, RS Menon; Analysis of circumferential shielding as a method to decouple radiofrequency coils for MRI; Concepts in MR Part B; 43B(1), 2013; p.11-21

KM Gilbert, **J-G Belliveau**, AT Curtis, JS Gati, LM Klassen, RS Menon; A Conformal Transceive Array for 7 T Neuroimaging; Magn. Res. Med.; 67(5), 2012; p.1487-1496